UNIVERSITY OF MICHIGAN
SEP 16 1953
ENGINEERING LIBRARY

JOURNAL OF THE AERONAUTICAL SCIENCES

VOLUME 20 SEPTEMBER, 1953 NUMBER 9

CONTENTS

Aerodynamic Interference Between Moving Blade Rows ..... NELSON H. KEMP AND W. R. SEARS 585

Stall-Flutter in Cascades ..... F. SISTO 598

An Exact Solution for the Buckling Load of Flat Sandwich Panels with Loaded Edges Clamped ..... S. V. NARDO 605

Thermal Stresses in Conical Shells ..... J. H. HUTH 613

Diffusers for Supersonic Wind Tunnels ..... J. LUKASIEWICZ 617

Transonic Flow Past Simple Bodies ..... J. D. COLE, G. E. SOLOMON, AND W. W. WILLMARTH 627

Free-Flight Determinations of the Drag Coefficients of Spheres ..... ALBERT MAY AND W. R. WITT, JR. 635

Bending Tests of Thin-Walled Sandwich Cylinders ..... GEORGE GERARD 639

Readers' Forum: "Minimum Drag Cambered Rectangular Wing for Supersonic Speeds," by N. Rott; "On Asymptotic Solutions for the Heat Transfer at Varying Wall Temperatures in a Laminar Boundary Layer with Hartree's Velocity Profiles," by Arthur N. Tifford and Sheng To Chu; "On the Behavior of a Sharp Leading Edge," by Y. C. Fung; "The Effect of Dissociation in the Stagnation Region of a Blunt-Nosed Body," by Ivan E. Beckwith; "Heat Transfer in a Transitional and Turbulent Boundary Layer at Supersonic Speeds," by William B. Fallis; "On the Operational Form of the Linearized Equation of Supersonic Flow," by L. E. Fraenkel; "On the Velocity Distribution in the Laminar Sublayer and Transition Region in Turbulent Shear Flows," by Francis R. Hama; "The Medium in Fluid Mechanics," by L. S. Dzung; "Comments on Location of Detached Shock Waves Ahead of Plane Bodies," by Robert Wesley Truitt; "On the Transonic Drag of a Cone Cylinder," by John W. Miles; "Similar Solutions of Compressible Boundary-Layer Equations," by Ting-Yi Li and Henry T. Nagamatsu; "Turbulence Measurements in Flight," by Max Kramer 642–656

Published by the
INSTITUTE OF THE AERONAUTICAL SCIENCES, INC.

JOURNAL OF THE AERONAUTICAL SCIENCES

Editor: HUGH L. DRYDEN, *Director, NACA*

Associate Editor: ROBERT R. DEXTER *Managing Editor:* BERNEICE H. JARCK

Editorial Committee

Aerodynamics

Francis Clauser
Howard Emmons
Antonio Ferri
Alexander Flax
R. Paul Harrington
R. T. Jones
Carl Kaplan
H. W. Liepmann
C. C. Lin
H. F. Ludloff
Harold Luskin
John R. Markham
Clark B. Millikan
Shatswell Ober
W. Bailey Oswald
Allen E. Puckett
Elliott G. Reid
H. J. E. Reid
Russell Robinson
G. B. Schubauer
W. R. Sears
John Stack
Theodore von Kármán

Air Transport

Charles Froesch
J. A. Herlihy
R. D. Kelly
Otto E. Kirchner
Jerome Lederer
John C. Leslie
R. Dixon Speas

Flight Testing

W. K. Ebel
R. R. Gilruth
Melvin N. Gough
B. G. Stout

Structures and Materials

W. B. Bleakney
E. W. Conlon
L. H. Donnell
E. C. Hartmann
N. J. Hoff
Samuel Levy
E. E. Lundquist
Alfred S. Niles
W. Ramberg
F. R. Shanley
H. W. Sibert
C. R. Strang
S. Timoshenko
H. S. Tsien
Chi-Teh Wang

Rotating Wing Aircraft

F. B. Gustafson
K. H. Hohenemser
Bartram Kelley
R. B. Maloy
Ralph McClarren
R. H. Miller
R. H. Prewitt
Igor I. Sikorsky

Vibration and Flutter

Lee Arnold
M. A. Biot
R. L. Bisplinghoff
William Bollay
Chieh-Chien Chang
I. E. Garrick
Martin Goland
J. P. Den Hartog

Aircraft Design

W. E. Beall
W. K. Ebel
Hall L. Hibbard
Richard Hutton
C. L. Johnson
A. A. Kartveli
C. J. McCarthy
Fred E. Weick
Robert J. Woods

Electronics in Aviation

K. C. Black
E. F. Herzog
David S. Little
D. K. Martin
George Rappaport
Paul Rosenberg
L. M. Sherer

Physiologic Problems

H. G. Armstrong
Louis H. Bauer
Robert J. Benford
Eugene Du Bois
W. Randolph Lovelace, II
Ross A. MacFarland

Fuels and Oils

D. P. Barnard
J. H. Doolittle
Graham Edgar
R. T. Goodwin
S. D. Heron
A. M. Rothrock

Flight Propulsion

George W. Brady
Frank W. Caldwell
L. S. Hobbs
E. E. Johnson
Joseph Keenan
R. P. Kroon
Hans Reissner
Abe Silverstein
C. Fayette Taylor
E. S. Taylor
P. Taylor
E. S. Thompson
H. S. Tsien

Instruments

Allan G. Binnie
J. R. Bradburn
Charles H. Colvin
C. S. Draper
S. G. Eskin
O. E. Esval
H. W. Holzapfel
W. L. Howland
George H. Purcell
C. F. Savage
O. Hugo Schuck
C. L. Seward, Jr.
L. D. Statham
R. C. Sylvander
D. K. Warner

Meteorology

C. F. Brooks
D. M. Little
E. J. Minser
F. W. Reichelderfer
H. C. Willett

SUBSCRIPTION RATES

JOURNAL OF THE AERONAUTICAL SCIENCES, Published Monthly.—United States and Possessions: 1 Year, $12.00; Single Copies, $1.50. Foreign Countries Including Canada (American Currency Rates): 1 Year, $13.00; Single Copies, $1.50.

AERONAUTICAL ENGINEERING REVIEW, Published Monthly.—United States and Possessions: 1 Year, $3.00; Single Copies, $0.50. Foreign Countries Including Canada (American Currency Rates): 1 Year, $3.50; Single Copies, $0.50.

Notices of change of address should be sent to the Institute at least 30 days prior to actual change of address.

Manuscripts for publication, proofs, and all correspondence should be addressed to the Editorial Office of the JOURNAL.

Correspondence regarding subscriptions may be addressed to Publication Office, 20th and Northampton Sts., Easton, Pa., or to the Editorial Office of the JOURNAL OF THE AERONAUTICAL SCIENCES, 2 East 64th Street, New York 21, New York.

Copyright, 1953, by the Institute of the Aeronautical Sciences, Inc.

Entered as Second Class Matter at the Post Office, Easton, Pa., May 1, 1937. Acceptance for mailing at a special rate of Postage provided for in the Act of August 24, 1912. Authorized April 29, 1937.

The
form fi
tionary
results
are ap
blades.
represe
sional

In th
a singl
a first
steady
nonste
for the
wakes
that, v
theory
earlier
Expres
and mo

Num
cal of
values
The ef
are fou
blades

The
stator
of this
compre
that th
power

Prese
Meetin

* Th
Force,
Scienti

† Na
1953.
Aircraf

‡ Di

JOURNAL OF THE AERONAUTICAL SCIENCES

VOLUME 20 SEPTEMBER, 1953 NUMBER 9

Aerodynamic Interference Between Moving Blade Rows*

NELSON H. KEMP† AND W. R. SEARS‡

Cornell University

ABSTRACT

The blades of a typical turbomachine move through a nonuniform field of flow, disturbed by the induced effects of other stationary and moving blade rows. In this paper the concepts and results of the theory of single thin airfoils in nonuniform motion are applied to calculate the resulting nonsteady effects on such blades. Incompressible inviscid flow is considered. The usual representation of blade wheels as infinite cascades of two-dimensional airfoils is adopted.

In this investigation, attention is confined to the basic case of a single stator row followed by a single moving motor row. As a first approximation, it is assumed that, to calculate the nonsteady effects at any given blade, it is permissible to neglect the nonsteady parts of the circulation of all other blades. However, for the rotor blades, the effects of their passage through the vortex wakes shed by stator blades are also investigated. It is found that, with this approximation, the only results of thin-airfoil theory required can be obtained by a simple generalization of an earlier study of an airfoil flying through a sinusoidal gust pattern. Expressions are worked out for the unsteady components of lift and moment on stator and rotor blades.

Numerical calculations are carried out for some examples typical of compressor cascades. The results show fluctuating lift values with magnitudes as great as 18 per cent of the steady lift. The effects of stator wakes on the unsteady lift of rotor blades are found to be comparable to the induced effects of the stator blades themselves.

The rate of energy transfer to the wake pattern of the rotor-stator stage has also been calculated within the approximations of this theory, but the details are not presented here. For the compressor stages of the present numerical examples, it is found that this rate of energy transfer is a very small fraction of the power required to turn the rotor.

Presented at the Aerodynamics Session, Twenty-First Annual Meeting, IAS, New York, January 26–29, 1953.

* This work has partially been supported by the U.S. Air Force, Air Research and Development Command, Office of Scientific Research.

† National Science Foundation Pre-Doctoral Fellow, 1952–1953. Now Aeronautical Engineer, Research Department, United Aircraft Corporation.

‡ Director, Graduate School of Aeronautical Engineering.

LIST OF SYMBOLS

b	=	axial distance between centers of stator and rotor rows (Fig. 1)
b'	=	axial distance between trailing edge of stator row and leading edge of rotor row (Fig. 1)
c	=	blade semichord (Fig. 1)
d	=	pitch of blades in direction of rotation (Fig. 1)
h	=	parameter giving relative orientation of rotor and stator blades (Figs. 3b and 4b)
t	=	time
u, v	=	horizontal and vertical perturbation velocity components, respectively
x	=	coordinate along blade from center, positive toward trailing edge
y	=	coordinate perpendicular to x, positive up
z	=	$x + iy$
A	=	coefficient of steady bound-vortex distribution, Eqs. (27) and (38)
$C(\omega)$	=	Theodorsen function, $K_1(i\omega)/[K_0(i\omega) + K_1(i\omega)]$
C_E	=	energy coefficient, $E/\rho V^2 c$
${}_0C_L$	=	steady lift coefficient, ${}_0L/\rho V^2 c$
E	=	average energy per unit length per unit width in wake

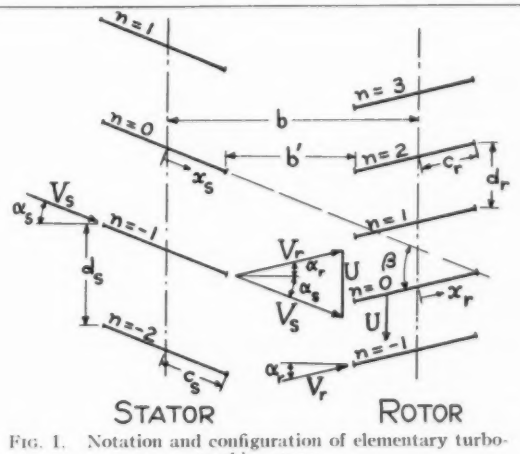

FIG. 1. Notation and configuration of elementary turbomachine stage.

F = coefficient of quasi-steady circulation, Eqs. (3), (48), and (53)
G = coefficient of velocity induced at blade, Eqs. (37) and (41)
H = steady bound-vortex distribution function, Eqs. (31) and (42)
J_n = Bessel function of the first kind
J = $J_0 - iJ_1$
K_n = modified Bessel function of the second kind
K_L, K_M = lift and moment functions defined in Eqs. (16) and (17)
L = lift, positive up
M = moment about the center of the blade, positive clockwise
R = real part
$S(\omega)$ = $\{i\omega[K_0(i\omega) + K_1(i\omega)]\}^{-1}$
U = rotational speed of rotor, positive down
V = speed of flow relative to blade
α = angle of stagger of blades (Fig. 1)
β = angle between stator and rotor blades, $\alpha_s + \alpha_r$
γ = strength of bound vortex distribution, positive clockwise
ϵ = strength of wake vortex distribution, positive clockwise
ζ = complex coordinate
ξ, η = Cartesian coordinates
λ = $\mu c/V$
μ = complex frequency of chordwise velocity distribution, Eq. (13)
ν = circular frequency of motion in time, $\nu_s = 2\pi U/d_r$, $\nu_r = 2\pi U/d_s$
ρ = air density
σ = solidity of row, $2c/d$
ω = reduced frequency, $\nu c/V$
Γ = circulation, positive clockwise
$\sum_n$ = summation from $n = 1$ to $n = +\infty$
$\sum_n'$ = summation from $n = -\infty$ to $n = +\infty$, omitting $n = 0$ term

Postsubscripts

s = stator
r = rotor
k, m, n = summation indices
n = nth blade

Presubscripts

o = steady quantities
q = quasi-steady quantities
1 = apparent-mass contributions
2 = wake contributions
t = time-dependent quantities

Superscripts

s = stator
r = rotor
$r1$ = effects at rotor due to motion of steady stator circulation
$r2$ = effects at rotor due to stator wakes

Introduction

Engineers have long recognized that the airfoils arranged in rotating and stationary cascades of axial-flow machinery do not operate in steady flow. A typical airfoil of such a cascade acts in the disturbance field of all the other airfoils of its own blade row and of near-by blade rows. Since these rows rotate relative to one another, each airfoil acts in a time-varying disturbance field; thus, its circulation varies with time, it experiences nonsteady forces, and it produces a varying disturbance field itself. The periodic changes of its circulation involve the production of a wake of vortices shed into the fluid at its trailing edge, as will be discussed below, and this phenomenon represents an undesirable energy exchange. The probable magnitude of this energy exchange, in a typical turbojet engine, has been discussed briefly by Wu,[1] based largely on the work of Keller.[2]

The intention here is to attack the problem of mutual interference of blades in cascades, due to relative motion of successive blade rows, on the basis of the theory of thin airfoils in unsteady motion. The objectives of this calculation will be to evaluate the magnitudes of the unsteady forces on the blades and the rate of energy transfer to wake vortices and to determine how these are affected by the major geometrical and aerodynamic parameters.

To make any real progress in this complex problem, a number of simplifying approximations seems to be required from the start. Thus, the fluid will be assumed incompressible, and the usual representation of a blade wheel by an infinite cascade of two-dimensional airfoils will be adopted. The airfoil theory to be used here is based, furthermore, upon the approximation of an inviscid fluid. This will not eliminate the possibility of accounting for some of the effects of viscous wakes—in fact, this may be one of the important applications of the methods of this study. Nevertheless, in the present report all viscous effects are neglected to avoid needless complications in the development of the methods and in the belief that the extension to account for passage of the blades through the viscous wakes of blades upstream can be accomplished later without serious difficulty.

Since there is no usable nonsteady-airfoil theory without the approximation of thin slightly cambered (i.e., lightly loaded) airfoils, the restriction to small turning angles through the blade rows seems to be an inevitable one. Thus the study is limited to cascades of blades whose chord lines lie approximately in the direction of the relative stream vector. It is therefore more directly applicable to typical compressor stages than to turbines.

Finally, for the sake of simplicity in this initial attack on the problem, attention will be confined to the elementary case of a single stator cascade followed by a single rotor cascade, as sketched in Fig. 1. This figure represents two infinite cascades of nearly plane, thin airfoils of unequal chords, gaps, and incidence and spaced an arbitrary distance apart. The angle α_s represents the swirl of the entering basic stream. The rotor row moves (downward) relative to the stator with velocity U, and α_r denotes the apparent swirl of the basic stream relative to the rotor, as indicated in Fig. 1. It is to be understood that, in the usual fashion of airfoil theory, all aerodynamic effects of the blade rows

are to be represented as induced velocities superimposed on this basic flow. The lightly loaded airfoil approximation means that such induced velocities are always small compared with V_x or V_r.

Unsteady Airfoil Theory

Before attacking this problem, it may be helpful to review briefly the major assumptions of the theory of thin airfoils in unsteady motion and some of its conclusions that are applicable here. For a more complete account, the reader is referred to references 3 and 4.

In this theory the airfoil is visualized as being replaced by a plane vortex sheet (Fig. 2) whose strength $\gamma(x, t)$ is such, at every instant, as to cancel the relative velocity component normal to the airfoil surface, thus satisfying the boundary condition there. The Kutta-Joukowski condition of finite velocity at the trailing edge is imposed at every instant. According to the theorem that the total circulation about the whole system is invariant, variations of the airfoil circulation ${}_1\Gamma(t)$ must be accompanied by the shedding of free vortices—the so-called "starting vortices"—at the trailing edge. Since no forces act on these shed vortices, they are carried away by the flow—i.e., in first-order theory, they are carried rearward with the stream velocity V.

Thus, the determination of flow about an airfoil in nonsteady motion or subjected to nonsteady flow conditions is similar to the same problem in steady-airfoil theory, except that the transient velocity field of the trailing wake of free vortices must be accounted for in calculating $\gamma(x, t)$. That is, the wake induces velocity components normal to the airfoil, which are superimposed upon other relative normal components because of the airfoil's camber, incidence, and motion and due to nonuniformities of the stream. All of these components are involved in the determination of $\gamma(x, t)$, as mentioned above.

The only additional complication caused by the transient nature of the flow arises in the calculation of pressures and forces after $\gamma(x, t)$ is known. It will be recalled that the formula for pressure in terms of velocity components is different in steady and nonsteady flows. The familiar Joukowski theorem, which equates the lift to $\rho V\Gamma$, is no longer valid. Instead, the lift is given by more complicated expressions, which are worked out[3, 4] by separating the lift into three recognizable terms,

$$ {}_1L(t) = {}_qL(t) + {}_1L(t) + {}_2L(t) \tag{1} $$

where ${}_qL(t)$ is the lift that would be calculated for the instantaneous motion and flow conditions, neglecting entirely the presence of wake vortices (this is called the *quasi-steady* lift); ${}_1L(t)$ is the lift corresponding to variations of the "apparent mass" of the airfoil; and ${}_2L(t)$ contains all wake effects.

The moment about the airfoil center is given similarly by three analogous terms,

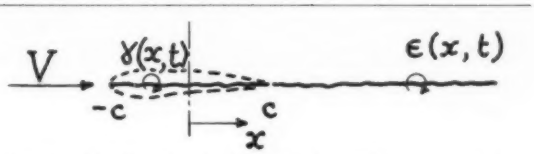

Fig. 2. Airfoil and wake in unsteady motion represented as vortex sheets.

$$ {}_1M(t) = {}_qM(t) + {}_1M(t) + {}_2M(t) \tag{2} $$

Formulas for calculation of ${}_1L$, ${}_2L$, ${}_1M$, and ${}_2M$ are given in references 3 and 4, and some of these will be reviewed below. Formulas for determination of the quasi-steady lift and moment, ${}_qL$ and ${}_qM$, are available in aerodynamics textbooks and standard reference works.[5, 8] Only ${}_2L$ and ${}_2M$ require knowledge of the wake configuration and therefore depend on the history of the motion.

Fortunately, considerable simplification of this whole matter is possible if the motion is sinusoidal in time. Then as can easily be found,[3] all three parts of the lift and moment are sinusoidal, the wake vortex strength is sinusoidal in both x and t, and ${}_2L$ and ${}_2M$ can be calculated directly in terms of ${}_qL$.

Because the expressions for lift and motion for a certain case of sinusoidal motion will be used extensively in the present analysis, they will be reviewed now. The familiar complex notation will be used to represent sinusoidally varying terms; it must be remembered that, wherever physical quantities are given complex expressions, it is the real part that is to be taken unless otherwise specified.

If the motion of the airfoil of Fig. 2 is such that its quasi-steady circulation is given by

$$ {}_q\Gamma(t) = Fe^{i\nu t} \tag{3} $$

then reference 3 shows that

$$ {}_qL(t) + {}_2L(t) = {}_qL(t)C(\omega) \tag{4} $$

where ω denotes the "reduced frequency," $\nu c/V$, c being the semichord, and $C(\omega)$ is the Theodorsen function,[6] which plays such an important part in wing-flutter analysis. The Theodorsen function is a complex function whose real and imaginary parts are tabulated in various references. One analytic formula for it is

$$ C(\omega) = K_1(i\omega)/[K_0(i\omega) + K_1(i\omega)] \tag{5} $$

where K_0 and K_1 are modified Bessel functions of the second kind.[9]

Since the expression for ${}_1L(t)$ is not needed in the present paper, it will not be given. Instead, the results of the special case of sinusoidal motion of interest for the purposes of this paper will now be summarized. Reference 4 shows that, if an airfoil operates in a sinusoidal gust pattern such that the relative upwash at the airfoil is given by

$$v(x, t) = v_0 e^{i\nu(t - x/V)} \tag{6}$$

then the total nonsteady lift and moment about the center are given by

$$\left.\begin{aligned} {}_tL(t) &= 2\pi\rho c V v_0 S(\omega) e^{i\nu t} \\ {}_tM(t) &= {}_tL(t)(1/2)c \end{aligned}\right\} \tag{7}$$

where c is the semichord (not the chord, as in reference 4) and

$$S(\omega) = \{i\omega[K_o(i\omega) + K_1(i\omega)]\}^{-1} \tag{8}$$

[The identification of the function $S(\omega)$ with that given in reference 4 was made in reference 11.]

Inspection of the original form of ${}_tL(t)$ in Eq. (14) of reference 4, shows that, since the coefficient of $C(\omega)$ in the expression for ${}_tL(t)$ must be ${}_qL(t)$ [see Eq. (4)], the corresponding quasi-steady circulation is given by

$${}_q\Gamma(t) = 2\pi c v_o J(\omega) e^{i\nu t} \tag{9}$$

where $J(z)$ is a combination of Bessel functions defined as

$$J(z) \equiv J_o(z) - iJ_1(z) \tag{10}$$

From ${}_q\Gamma(t)$ the strength of the vortex distribution in the wake, $\epsilon(x, t)$, can be obtained. Reference 3 shows that, for general sinusoidal motion in which ${}_q\Gamma(t)$ is of the form of Eq. (3), the wake strength is

$$\epsilon(x, t) = \frac{-Fe^{i\nu(t - x/V)}}{c[K_o(i\omega) + K_1(i\omega)]} = -\frac{F}{c} i\omega S(\omega) e^{i\nu(t - x/V)} \tag{11}$$

Applying this to Eq. (9), the wake strength for the sinusoidal gust of Eq. (6) becomes

$$\epsilon(x, t) = -2\pi v_o J(\omega) i\omega S(\omega) e^{i\nu(t - x/V)} \tag{12}$$

These results were derived in reference 4 only for the special case of an airfoil flying through a stationary sinusoidal gust pattern. It will be shown in the present report that, by means of a simple generalization, they provide just the formulas needed to calculate the nonsteady aerodynamic quantities in the present rotor-stator problem. The generalization required has already been pointed out in reference 11; it consists of replacing the relative upwash expression (6) by

$$v(x, t) = v_o e^{i\nu t} e^{-i\mu x/V} \tag{13}$$

where ν is real but μ may be an arbitrary complex number. As will be seen farther below, the induced velocity fields in which the rotor and stator blades operate can be expressed in this special form.

The extension of reference 4 to this more general case is not difficult; it is only necessary to change the argument of the Bessel functions J_n in Eqs. (13), (14), and (15) of that reference to the complex parameter $\lambda \equiv \mu c/V$. Upon application of the recurrence relation for Bessel functions, the expressions for lift and moment are then immediately found to be

$${}_tL(t) = 2\pi\rho c V v_o K_L(\omega, \lambda) e^{i\nu t} \tag{14}$$

$${}_tM(t) = \pi\rho c^2 V v_o K_M(\omega, \lambda) e^{i\nu t} \tag{15}$$

where

$$K_L(\omega, \lambda) \equiv J(\lambda)C(\omega) + i(\omega/\lambda)J_1(\lambda) \tag{16}$$

$$K_M(\omega, \lambda) \equiv J(\lambda)[C(\omega) - 1] + (\omega/\lambda)J_o(\lambda) + (2/\lambda)(1 - \omega/\lambda)J_1(\lambda) \tag{17}$$

(In reference 11, K_L was denoted by K.)

Again inspection of Eqs. (14) and (16) shows that the corresponding quasi-steady circulation for this case must be

$${}_q\Gamma(t) = 2\pi c v_o J(\lambda) e^{i\nu t} \tag{18}$$

so that the wake vortex strength follows from Eq. (11) as

$$\epsilon(x, t) = -2\pi v_o J(\lambda) i\omega S(\omega) e^{i\nu(t - x/V)} \tag{19}$$

The results expressed in Eqs. (7), (9), (12), (14), (15), (18), and (19) are those that will be used in the present attack on the two-cascade problem set up in the preceding section.

Application to Stator-Rotor Problem

In basic idea, the extension of thin airfoil theory to the stator-rotor interference problem of the present paper is fairly obvious: One must consider each airfoil to be acting in a velocity field induced by (a) its own wake, (b) the (variable) bound vortices of fellow members of its own blade row, (c) their wakes, (d) the (variable) bound vortices of members of the other blade row, and (e) their wakes.

It is not surprising, however, that this approach leads to rather discouraging mathematical complexity—in fact, to a pair of intractable, simultaneous integral equations for the stator and rotor bound-vortex distributions. It seems more profitable to adopt a different scheme, based upon an idea of *successive approximations*, which will now be outlined as follows:

(1) Let it be assumed, subject to later verification, that the entire unsteady effect on the circulation of any blade is small compared with the steady circulation carried by the blade. Symbolically, this means that, for any airfoil

$$\Gamma(t) = {}_o\Gamma + {}_t\Gamma(t); \quad |{}_t\Gamma(t)| \ll |{}_o\Gamma|$$

where ${}_o\Gamma$ is the steady circulation of the blade, considering its camber, incidence, rotational speed (for rotor blades), and the steady induction effects of its own cascade and the other cascade. In other words, ${}_o\Gamma$ is the circulation ordinarily estimated by the designer, neglecting all nonsteady effects. Thus, ${}_t\Gamma(t)$ contains all the effects due to the relative motion of the cascades.

(2) As a first approximation, to calculate the nonsteady effects on a typical stator blade, such as ${}_t\Gamma^s(t)$, let it be assumed that the only significant contribution

arises from ${}_0\Gamma'$. This means that the effects of the unsteady terms ${}_1\Gamma'(t)$ of rotor circulation, as well as the unsteady parts of the circulation of all other stator blades and also all vortex wakes except that shed by the blade itself, are neglected. (Presumably this approximation breaks down for stator cascades of extremely large solidity, in which the adjacent blades are so close that their nonsteady circulation components induce large effects.)

(3) In the same approximation, to calculate the unsteady effects on a typical rotor blade, let it be assumed that the significant contribution arises from ${}_0\Gamma^s$. For the rotor blades, however, one additional effect will also be investigated—viz., the effect of their passage through the vortex wakes shed by the stator blades. To be sure, this is, in the present system of approximation, a sort of second-order contribution, since it is due to the unsteady part of the stator circulation. But the rotor blades pass directly through the stator wakes and therefore may encounter appreciable induced velocities due to them. For this reason it would not be surprising if this "secondary" effect were found to be comparable in magnitude to the "primary" effects of the steady circulation components.

In principle, the approximate theory outlined here might be the first step of a series of successive approximations—i.e., the second approximation to ${}_1\Gamma^s(t)$ might include the effects both of ${}_0\Gamma^r$ and of the first-approximation unsteady quantities. However, the mathematical complexities of the first approximation, as will be seen shortly, suggest that a second approximation might be extremely difficult. At any rate, the first step will permit approximate evaluation of some useful engineering data, the absolute accuracy of which may subsequently be checked by experiment or by closer approximations.

Calculation of Periodic Quantities

Induced Velocity Due to ${}_0\Gamma$

In this subsection the velocity at a rotor or stator blade induced by the steady circulation distribution of the blades of the other row, which is time-dependent because of the motion of these blades relative to the blade in question, will be found.

The upwash velocity on the x-axis and normal to that axis, produced by equal vortices of strength Γ' located at any N complex points ζ_n, is given by*

$$v = -(\Gamma'/2\pi) \sum_{n=1}^{N} 1/(x - \zeta_n) \tag{20}$$

If this equation is applied to the induction effect of the rotor on a stator blade and the rotor circulation is temporarily thought to be made up of single point vortices, as shown in Fig. 3a, then the induced velocity at the stator may be written as

* As mentioned above, the real part is implied.

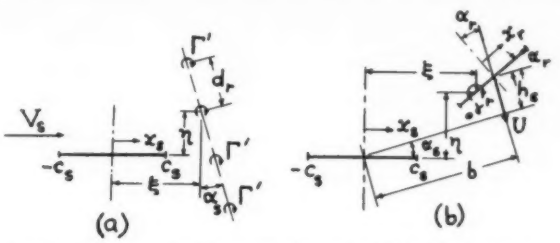

FIG. 3. Diagram used in computing velocity induced at stator blade.

$$v^s = -\frac{\Gamma'}{2\pi} \sum_{n=-\infty}^{+\infty} \frac{1}{x_s - (\xi + i\eta + ind_r e^{i\alpha_s})} \tag{21}$$

where x_s is measured parallel to the stator blade from its center and ξ and η are defined in Fig. 3a.

The summation in Eq. (21) may be performed using the well-known relation[7]

$$\sum_{n=-\infty}^{+\infty} 1/(z - in\pi) = \coth z$$

which gives

$$v^s = \frac{\Gamma' e^{-i\alpha_s}}{2d_r} \coth\left[\frac{\pi e^{-i\alpha_s}}{d_r}(\xi + i\eta - x_s)\right] \tag{22}$$

This form of the velocity induced by an infinite row of equal, equally spaced vortices is well known but is not so useful in the present case. It can, however, be transformed into a convenient form as follows: If $R(z) > 0$,

$$\coth z = 1 + 2\sum_{m} e^{-2mz} \tag{23}\dagger$$

Moreover, when the line of vortices (Fig. 3a) does not intersect the stator blade, which is true in the present case, it is easily verified that

$$R[e^{-i\alpha_s}(\xi + i\eta - x_s)] > 0$$

and therefore Eq. (23) is applicable to Eq. (22). The resulting expression for v^s is

$$v^s = \frac{\Gamma' e^{-i\alpha_s}}{2d_r}\left\{1 + 2\sum_{m} \exp \times \left[-\frac{2\pi m}{d_r} e^{-i\alpha_s}(\xi + i\eta - x_s)\right]\right\} \tag{24}$$

If, now, Γ' is replaced by a distribution of vortices, ${}_0\gamma'(x_r)\,dx_r$ along a line representing a typical rotor blade, as shown in Fig. 3b, Eq. (24) need only be integrated over x_r from $-c_r$ to c_r. The resulting velocity

† Since summation signs will appear many times in this analysis, it will be convenient at the outset to adopt the following conventions: $\sum_n$ will denote $\sum_{n=1}^{\infty}$, while $\sum_n'$ will denote $\sum_{n=-\infty}^{-1} + \sum_{n=1}^{\infty}$. If any other type of summation is used, it will be explicitly indicated.

v^s is the induced velocity at the stator blade due to the whole row of rotor blades in a given position. In order to perform this integration, the complex coordinate $\xi + i\eta$ must be written in terms of the geometric parameters and of x_r, which is measured along the rotor blade.

With the aid of Fig. 3b, it is seen that

$$\xi + i\eta = (b + ih_s)e^{i\alpha_s} + x_r e^{i(\alpha_s + \alpha_r)} \tag{25}$$

where b is the spacing of the two blade rows and h_s is defined in Fig. 3b, positive when measured upward. Use of Eq. (25) and replacement of Γ' by ${}_o\gamma^r(x_r)\,dx_r$ yields, upon integration,

$$v^s = \frac{{}_o\Gamma^r e^{-i\alpha_s}}{2d_r}\left\{1 + 2\sum_m \exp\left[-\frac{2\pi m}{d_r}(b + ih_s - x_s e^{-i\alpha_s})\right]\int_{-c_r}^{c_r}\frac{{}_o\gamma^r(x_r)}{{}_o\Gamma^r}\exp\left[-\frac{2\pi m}{d_r}e^{i\alpha_r}x_r\right]dx_r\right\} \tag{26}$$

where ${}_o\Gamma^r \equiv \int_{-c_r}^{c_r} {}_o\gamma^r(x_r)\,dx_r$.

To eliminate the integral from Eq. (26), it is convenient to assume $0\gamma^r$ in the Glauert form[8]

$${}_o\gamma^r = 2V_r[A_o{}^r(1 - \cos\theta)/\sin\theta + 2\sum_n A_n{}^r \sin n\theta] \tag{27}$$

where $x_r = c_r \cos\theta$. In this form, ${}_o\Gamma^r$ and ${}_oM^r$, the moment about the center, are given by

$${}_o\Gamma^r = 2\pi c_r V_r(A_o{}^r + A_1{}^r) \tag{28}$$

$${}_oM^r = 2\pi c_r{}^2\rho V_r{}^2(A_o{}^r - A_2{}^r) \tag{29}$$

Furthermore, the integral appearing in Eq. (26), by virtue of some trigonometric identities, becomes

$$\int_{-c_r}^{c_r}\frac{{}_o\gamma^r(x_r)}{{}_o\Gamma^r}\exp\left[-\frac{2\pi m}{d_r}e^{i\alpha_r}x_r\right]dx_r \equiv H_m{}^r = \frac{1}{\pi}\int_0^\pi\left[1 + \sum_n\frac{A_{n+1}{}^r - A_{n-1}{}^r}{A_0{}^r + A_1{}^r}\cos n\theta\right]\exp\left[-\pi m\sigma_r e^{i\alpha_r}\cos\theta\right]d\theta$$

where σ_r is written for the rotor solidity $2c_r/d_r$.

Since

$$-\pi\sigma_r e^{i\alpha_r} \equiv -i\pi\sigma_r e^{-i[(\pi/2) - \alpha_r]}$$

the typical integral in the expression for $H_m{}^r$ is

$$\frac{1}{\pi}\int_0^\pi \exp\left\{-i\pi\sigma_r m e^{-i[(\pi/2) - \alpha_r]}\right\}\cos n\theta\,d\theta$$

The well-known relation $J_n(-z) = (-1)^n J_n(z)$ combined with[10]

$$\frac{i^{-n}}{\pi}\int_0^\pi e^{iz\cos\theta}\cos n\theta\,d\theta = J_n(z)$$

leads to

$$\frac{1}{\pi}\int_0^\pi e^{-iz\cos\theta}\cos n\theta\,d\theta = (-i)^n J_n(z) \tag{30}$$

With the result of Eq. (30), $H_m{}^r$ becomes

$$H_m{}^r \equiv J_o\{\pi m\sigma_r e^{-i[(\pi/2) - \alpha_r]}\} + \sum_n (-i)^n\frac{A_{n+1}{}^r - A_{n-1}{}^r}{A_o{}^r + A_1{}^r}J_n\{\pi m\sigma_r e^{-i[(\pi/2) - \alpha_r]}\} \tag{31}$$

In terms of this notation, Eq. (26) becomes

$$v^s = \frac{{}_o\Gamma^r e^{-i\alpha_s}}{2d_r}\left\{1 + 2\sum_m H_m{}^r \exp\times\left[-\frac{2\pi m}{d_r}(b + ih_s - x_s e^{-i\alpha_s})\right]\right\} \tag{32}$$

In order to complete the expression for $v^s(x_s, t)$, it is only necessary to insert the time factor by assuming that the rotor row, hitherto taken as stationary, is in motion. It is convenient to take the positions of the zero-th rotor and stator blades ($n = 0$), for which the calculations are done, to be as shown in Fig. 1 at $t = 0$. The trailing edge of the zero-th rotor blade just touches a line drawn through the zero-th stator blade. In this position

$$h_s = -b\tan\alpha_s - c_r\sin\beta/\cos\alpha_s$$

where $\beta \equiv \alpha_s + \alpha_r$. Since the rotor moves downward at a speed U, h_s increases negatively with time as Ut. Thus,

$$b + ih_s = b - i(b\tan\alpha_s + c_r\sin\beta/\cos\alpha_s) - iUt \tag{33}$$

Reference to the velocity triangle of Fig. 1 gives the following relations:

$$\left.\begin{aligned} V_r\sin\beta &= U\cos\alpha_s;\quad V_s\sin\alpha_s = U - V_r\sin\alpha_r \\ V_s\cos\alpha_s &= V_r\cos\alpha_r \end{aligned}\right\} \tag{34}$$

so that

$$b + ih_s = b[1 + i(\tan\alpha_r - U/V_s\cos\alpha_s)] - iUc_r/V_r - iUt \tag{35}$$

Inserting Eq. (35) in Eq. (32), the final expression for v^s is obtained.

$$v^s(x_s, t) = \frac{{}_o\Gamma^r e^{-i\alpha_s}}{2d_r} + \frac{{}_o\Gamma^r}{2\pi c_s} \sum_m G_m{}^s \exp \times \left(\frac{2\pi m}{d_r} e^{-i\alpha_s} x_s\right) e^{i\nu_s m t} \quad (36)$$

where

$$G_m{}^s \equiv \frac{\pi \sigma_s d_s}{d_r} e^{-i\alpha_s} H_m{}^r \exp \left\{ -\pi m \sigma_r \times \left[\frac{b}{c_r}\left(1 + i \tan \alpha_r - \frac{iU}{V_s \cos \alpha_s}\right) - \frac{iU}{V_r}\right]\right\} \quad (37)$$

with $2c_s/d_s \equiv \sigma_s$, the stator solidity, and $\nu_s \equiv 2\pi U/d_r$, the stator frequency, which is the circular frequency at which the rotor blades move past a stator blade.

The advantage of the series form of v^s over the hyperbolic-cotangent expression is now clear. The variables x_r, x_s, and t were separated so that the integration over x_r was easily done; furthermore, in each term of the series, x_s and t appear in the same form as x and t do in Eq. (13). Since the problem deals with thin airfoils and is therefore linear, the results of Eqs. (14), (15), (18), and (19) for the aerodynamic quantities may be applied directly to each term of v^s and then summed to give the total effect of all terms. This procedure will be followed in the next section.

It should be noted that the time-independent term in v^s is precisely that which arises from the steady induction effect of the rotor row on a stator blade and is usually taken into account in the steady-flow quantities by the turbomachinery designer. If the rotor and stator rows are far apart ($b \to \infty$), only this term remains. In order that this steady-flow effect is not inadvertently included twice, the time-independent term in v^s will be omitted hereafter.

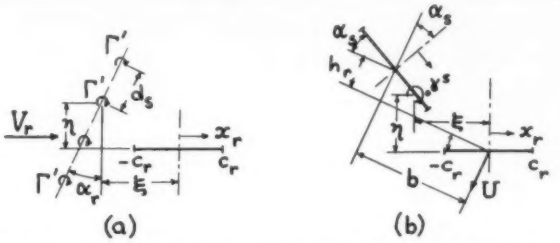

FIG. 4. Diagram used in computing velocity induced at rotor blade.

The calculation of the velocity v^{r1} induced at a rotor blade by the motion of the steady-stator circulation ${}_o\Gamma^s$ parallels that of v^s exactly and can be carried out with the aid of Fig. 4. Besides the interchange of subscripts on the geometric parameters, $-\alpha_s$ must be replaced by α_r and α_r by $-\alpha_s$ to obtain the expressions for v^{r1} from those for v^s. With these replacements and the introduction of $x_s = c_s \cos \theta$

$${}_o\gamma^s = 2V_s[A_o{}^s(1 - \cos\theta)/\sin\theta + 2\sum_n A_n{}^s \sin n\theta] \quad (38)$$

$$\left.\begin{aligned} {}_o\Gamma^s &= 2\pi c_s V_s (A_o{}^s + A_1{}^s) \\ {}_oM^s &= 2\pi c_s{}^2 \rho V_s{}^2 (A_o{}^s - A_2{}^s) \end{aligned}\right\} \quad (39)$$

the final expression for $v^{r1}(x_r, t)$ is found,

$$v^{r1}(x_r, t) = \frac{-{}_o\Gamma^s e^{i\alpha_r}}{2d_s} + \frac{{}_o\Gamma^s}{2\pi c_r} \sum_m G_m{}^r \exp\left(-\frac{2\pi m}{d_s} e^{i\alpha_r} x_r\right) e^{i\nu_r m t} \quad (40)$$

Here

$$G_m{}^r \equiv \frac{-\pi \sigma_r d_r}{d_s} e^{i\alpha_r} H_m{}^s \exp\left\{\frac{-\pi \sigma_r d_r}{d_s}\left[\frac{b}{c_r}\left(1 + i \tan \alpha_r - \frac{iU}{V_s \cos \alpha_s}\right) - \frac{iU}{V_r}\right]\right\} \quad (41)$$

$$H_m{}^s \equiv J_o\{\pi \sigma_s m e^{i[(\pi/2) - \alpha_s]}\} + \sum_n (-i)^n \frac{A_{n+1}{}^s - A_{n-1}{}^s}{A_o{}^s + A_1{}^s} J_n\{\pi \sigma_s m e^{i[(\pi/2) - \alpha_s]}\} \quad (42)$$

and the rotor frequency ν_r is given by $\nu_r \equiv 2\pi U/d_s$.

The velocity at the rotor just calculated is given the double superscript because, as explained in the preceding section, two types of nonsteady effects on the rotors will be investigated. The first kind, due to the motion of the steady stator circulation past the rotor, will be denoted by the superscript $r1$; the velocity of Eq. (40) is one of these. The second kind—i.e., the effects of the stator wakes at the rotor—will be given the superscript $r2$. These latter are discussed farther below.

Again, the time-independent term in Eq. (40) will be omitted from further consideration here, its effects already having been accounted for in the steady-flow quantities.

Now that v^s and v^{r1} are available, the application to them of the formulas developed in connection with the relative velocity of Eq. (13) can be made to calculate the nonsteady lift and moment and the properties of the vortex wakes. This will be done for the stator in the next subsection and for the rotor in a later subsection.

Nonsteady Lift and Moment of Stator

As has been mentioned above, the similarity of the form of each term of v^s, Eq. (36), to that of v in Eq. (13) leads immediately to the use of Eqs. (14) and (15) to obtain the nonsteady lift and moment on a stator

blade. Furthermore, the linearity of the problem permits one to apply these equations term by term to Eq. (36).

The argument of the exponential involving x_s in Eq. (36) can be written

$$(2\pi m x_s/d_r)e^{-i\alpha_s} \equiv -i(2\pi m V_s/d_r)(x_s/V_s)e^{i[(\pi/2) - \alpha_s]} \tag{43}$$

Let

$$\left.\begin{aligned}\mu_s &\equiv (2\pi V_s/d_r)e^{i[(\pi/2) - \alpha_s]}\\ \lambda_s &\equiv (2\pi c_s/d_r)e^{i[(\pi/2) - \alpha_s]}\end{aligned}\right\} \tag{44}$$

Then application of Eqs. (14) and (15) to Eq. (36) gives

$$\frac{{}_tL^s(t)}{{}_oL^s} = \frac{{}_o\Gamma^r}{{}_o\Gamma^s}\sum_m G_m{}^s K_L(\omega_s m, \lambda_s m)e^{i\nu_s mt} \tag{45}$$

$$\frac{{}_tM^s(t)}{2{}_oL^s c_s} = \frac{{}_o\Gamma^r}{{}_o\Gamma^s}\sum_m \frac{1}{4} G_m{}^s K_M(\omega_s m, \lambda_s m)e^{i\nu_s mt} \tag{46}$$

Here the steady-stator lift ${}_o\Gamma^s\rho V_s$ is denoted by ${}_oL^s$, and ω_s is the stator reduced frequency $\nu_s c_s/V_s$.

Furthermore, use of Eq. (18) gives the quasi-steady circulation as

$${}_q\Gamma^s(t) = {}_o\Gamma^r\sum_m F_m{}^s e^{i\nu_s mt} \tag{47}$$

where

$$F_m{}^s \equiv G_m{}^s J(\lambda_s m) \tag{48}$$

This expression for ${}_q\Gamma^s$ will be needed later.

Eqs. (45) and (46) are to be used to evaluate, within the approximations of the present theory, the nonsteady oscillatory parts of the lift and moment on a stator blade. In addition to the various geometrical parameters characterizing the stage, this calculation requires knowledge of the coefficients $A_n{}^r$ of the rotor's steady circulation distribution. In actual use, of course, one will approximate to this distribution by a small number of terms—i.e., one will terminate the series over n in Eq. (31). Moreover, one must decide how many harmonics are of interest in the lift and moment formulas and will retain only that number of terms in the summations over m in Eqs. (45) and (46). This process will be made clearer by means of some examples in a later section of this paper.

Nonsteady Lift and Moment of Rotor

The lift and moment of the rotor blade due to the motion of the steady-stator circulation ${}_o\Gamma^s$, which are denoted by the superscript $r1$, can be found from v^{r1} of Eq. (40) exactly as the analogous quantities for the stator were found above.

The argument appearing in Eq. (40), $-(2\pi m x_r/d_s) \times e^{i\alpha_r}$ can be written $-i(2\pi m V_r/d_s)(x_r/V_r)e^{-i[(\pi/2) - \alpha_r]}$. Let

$$\left.\begin{aligned}\mu_r &\equiv (2\pi V_r/d_s)e^{-i[(\pi/2) - \alpha_r]}\\ \lambda_r &\equiv (2\pi c_r/d_r)e^{-i[(\pi/2) - \alpha_r]}\end{aligned}\right\} \tag{49}$$

Then, from Eqs. (14) and (15),

$$\frac{{}_tL^{r1}(t)}{{}_oL^r} = \frac{{}_o\Gamma^s}{{}_o\Gamma^r}\sum_m G_m{}^r K_L(\omega_r m, \lambda_r m)e^{i\nu_r mt} \tag{50}$$

$$\frac{{}_tM^{r1}(t)}{2{}_oL^r c_r} = \frac{{}_o\Gamma^s}{{}_o\Gamma^r}\sum_m \frac{1}{4} G_m{}^r K_M(\omega_r m, \lambda_r m)e^{i\nu_r mt} \tag{51}$$

Here the steady-rotor lift ${}_o\Gamma^r\rho V_r$ is denoted by ${}_oL^r$, and ω_r is the rotor reduced frequency $\nu_r c_r/V_r$.

From Eq. (18), the quasi-steady circulation is

$${}_q\Gamma^{r1}(t) = {}_o\Gamma^s\sum_m F_m{}^r e^{i\nu_r mt} \tag{52}$$

where

$$F_m{}^r \equiv G_m{}^r J(\lambda_r m) \tag{53}$$

The practical calculation of ${}_tL^{r1}$ and ${}_tM^{r1}$ is analogous to that of ${}_tL^s$ and ${}_tM^s$, described above—i.e., it requires knowledge of the steady stator circulation-distribution coefficients $A_n{}^s$, in addition to geometrical quantities. Again, a decision must be made concerning the number of harmonics required.

As mentioned above, the additional effects of the vortex wakes shed by stator blades are also taken into account in calculating conditions at the rotor blades. These give rise to the contributions identified here by the superscript $r2$. The details of this calculation are not reproduced here because of the necessity of conserving space, the calculations being somewhat lengthy. The detailed calculation may be found in reference 13.

To determine these $r2$ quantities, it is necessary first to determine the strength of the stator vortex wakes, which is easily done by means of Eqs. (19), (36), and (48), and then to work out the phase relationships between the successive stator wakes. This second item requires a study of the phase relationships existing within the stator row itself, the results of which are of general interest and will be of use later on. It is found that, if $f_n{}^s(t)$ is any function of time associated with the nth stator blade, such as its lift or circulation, it must be that

$$f_{n+k}{}^s(t) = f_n{}^s[t + (kd_s/U)] \tag{54}$$

Eq. (54) establishes not only the periodicity of effects in the stator row but also, because it applies to the stator circulation, the periodicity and phase relationships between various stator wakes.

[It may be mentioned here in passing that the analogous general relationship applying to any function $f_n{}^r(t)$ associated with the nth rotor blade is

$$f_{n+k}{}^r(t) = f_n{}^r[t - (kd_r/U)] \tag{55}$$

This result is needed in determining the energy transfer to the wake.]

The next step is to calculate the velocity components induced by the infinite row of sinusoidally varying vortex sheets which trails back from the stator blades. This is greatly simplified if the vortex sheets can be assumed to extend from $-\infty$ to $+\infty$ instead of originating at the stator trailing edges as they actually do. This

approximation is made; it is probably a good one, since the portions of stator wakes close to the rotor contribute the largest part of the velocity, while the contributions of portions farther away, where the error in the approximation lies, are probably negligible. With this simplification the calculation of the velocity component v^{r2} normal to the rotor blades at the position of a blade is simple except for the geometrical complications. The distortion of the stator wakes due to the passage through them of the rotor blades will be ignored, as is consistent with the approximations of thin-airfoil theory.

The velocity component v^{r2} is calculated for the zero-th rotor blade during the time interval $0 \leq t \leq d_s/U$ and, finally, is expressed in complex Fourier-series form. The result is thus obtained in the form

$$v^{r2}(x_r, t) = \sum_m \sum_k{}' v_{mk} \exp\left[i\nu_r k(t - x_r/V_r)\right] \quad (56)$$

where v_{mk} is a certain complex geometrical coefficient and x_r is the coordinate measured along this blade (Fig. 1). Expressions for the aerodynamic quantities associated with v^{r2} are now found immediately from Eq. (7), since each term of v^{r2} is of exactly the same form as Eq. (6) and the linearity of the present problem permits superposition. [The Fourier expansion mentioned above was carried out in order to throw this velocity into the form where Eq. (7) would apply.] The lift and moment are, finally,

$$\frac{{}_tL^{r2}(t)}{{}_oL^r} = -\sum_m \sum_k{}' \frac{\pi\sigma_r d_r}{d_s \cos\alpha_s} \exp\left[-im\pi\sigma_r\left(\frac{bU}{V_s c_r \cos\alpha_s} + \frac{U}{V_r}\right) + i\omega_r k\right] \times \frac{F_m{}^s S(\omega_s m) S(\omega_r k)(V_s d_r/V_r d_s)(k/m)}{1 + \cot^2\beta[1 - (V_s d_r/V_r d_s)(k/m)\sec\beta]^2} e^{i\nu_r kt} \quad (57)$$

$${}_tM^{r2}(t)/2_oL^r c_r = {}_tL^{r2}(t)/4_oL^r \quad (58)$$

From Eq. (9), the corresponding quasi-steady circulation is

$${}_q\Gamma^{r2} = \sum_m \sum_k{}' 2\pi c_r v_{mk} J(\omega_r k) e^{i\nu_r kt}$$

and v_{mk} can be found by comparing Eqs. (56) and (57) with Eqs. (6) and (7).

These formulas complete the calculation of unsteady lift and moment on stator and rotor blades. For practical computation of ${}_tL^{r2}$ and ${}_tM^{r2}$, the same decision as mentioned previously, regarding the number of harmonics, must be made. Here both stator and rotor circulation coefficients $A_n{}^s$ and $A_n{}^r$ are required. Moreover, there is a summation over m in Eq. (57), and judgment will be required regarding the number of terms of this series to be carried in computing each harmonic.

Calculation of Wake Energy

The wake of trailing vortices behind any airfoil in unsteady flow involves motion of the fluid far behind the airfoil and corresponding kinetic energy that the passage of the air foil has produced in the flow. As part of the present investigation, the energy left in this flow behind the elementary turbomachine stage (stator and rotor) has been calculated. This calculation is given in reference 13 and will be the subject of a subsequent short paper. For completeness, some remarks about the numerical values obtained for wake energies are included in the closing section below.

Numerical Calculations

Convergence of Series

Since the theoretical results presented in this paper are given in the form of infinite series, the first question to be answered when numerical calculations are undertaken is: How many terms of the series must be retained?—i.e., how rapid is the convergence? However, the successive terms in ${}_tL^s$, ${}_tM^s$, ${}_tL^{r1}$, and ${}_tM^{r1}$ and in the summations over k in ${}_tL^{r2}$ and ${}_tM^{r2}$ have a special significance: they are the successive *harmonics* of the forces and moments calculated. The virtue of the form in which these results have been obtained is that these periodic quantities are explicitly obtained as sums of these successive harmonics. Thus, each term will be of interest in itself, particularly in studies of blade vibration. The question of rapidity of convergence of these series is therefore simply the question of how rapidly the higher harmonics diminish in size.

On the other hand, the various harmonics of ${}_tL^{r2}$ and ${}_tM^{r2}$ involve infinite sums over m, so that the practical problem of approximating to infinite series by finite sums does arise here (and also in all the summations in the wake-energy expressions).

Investigation of the expressions for ${}_tL^s$, ${}_tM^s$, ${}_tL^{r1}$, and ${}_tM^{r1}$ shows that, when allowance is made for the exponential nature of $J_n(z)$, the principal factor tending to decrease the size of successive harmonics is $e^{-2\pi mb'/d}$, where b' is the axial distance from stator trailing edge to rotor leading edge (Fig. 1). For present-day axial compressors, $b'/d \cong 0.2$ so that $\exp(-2\pi b'/d) \cong 0.285$. This indicates that the successive harmonics ultimately decrease by a factor of at least one-quarter. This same factor is involved in the summations over m in ${}_tL^{r2}$ and ${}_tM^{r2}$. Therefore a few terms should give sufficient accuracy for engineering purposes.

A similar analysis of the harmonics of ${}_tL^{r2}$ and ${}_tM^{r2}$ shows that they behave like $k^{-3/2}$, which is a rather slow convergence.

To be sure, almost all the functions involved in these sums are oscillatory in nature, so that these approximate factors of convergence obtained by the use of asymptotic expressions may not hold exactly in any particular case. It is believed, however, that they give lower limits to the speed of convergence, and the actual convergence is even faster than they indicate. Most of the numerical examples worked out so far indicate that such is the case.

Evaluation of H-Functions

Before the calculations are started one more sum must be approximated, and that is the one in the H-functions, which comes from the Glauert expansions for the steady bound vortex distributions, ${}_o\gamma(x)$, Eqs. (21) and (33). The first coefficient, A_o, gives a distribution corresponding to angle of attack on an isolated flat-plate airfoil, while the second, A_1, gives a symmetrical elliptic distribution corresponding to circular-arc camber. Since they are the only coefficients that affect the total steady circulation ${}_o\Gamma$ and since they represent the effects of both camber and incidence, it is felt that the most important features of the flow will be retained if the series for ${}_o\gamma(x)$ is terminated after the second term—i.e., $A_n = 0$, $n \geq 2$.

With this simplification and the use of the recurrence relation for the Bessel functions, it is easy to show that

$$H_m\{\pi m\sigma e^{\pm i[(\pi/2) - \alpha]}\} = \frac{A_o}{A_o + A_1}(J_o + iJ_1) \mp \frac{2ie^{\pm i\alpha}}{\pi\sigma m}\frac{A_1}{A_o + A_1}J_1 \quad (59)$$

This result can easily be applied to $H_m{}^s$ or $H_m{}^r$ by proper choice of the sign and the parameters, as indicated by Eqs. (42) and (31), respectively. In Eq. (59), the effects of incidence and of camber are separated. If there is zero incidence in the steady part of the flow, then $A_o = 0$ and the steady lift distribution is *elliptical* over the chord; in this case the first term vanishes, leaving H_m expressed as one term, independent of A_1. If, on the other hand, there is only incidence, then $A_1 = 0$ and the steady chordwise lift distribution is the *flat-plate* one; again, H_m is given by a single term, $(J_o + iJ_1)$, independent of A_o.

The linearity of the lift and moment in H_m permits any combination of flat-plate and elliptical distributions to be imposed by merely adding pure flat-plate and pure elliptical results in the proper proportions. Also, since H_m appears as a factor in lift and moment, it is easy to convert elliptical results to flat-plate results, and vice versa, merely by multiplying by the proper (complex) factor. This fact proves useful in the numerical work. (This addition procedure will not, of course, give the correct wake energy, since the energy is nonlinear.)

The Bessel functions $J_o(re^{i\theta})$ and $J_1(re^{i\theta})$ are tabulated[12] for $0 \leq r \leq 10$ and $0 \leq \theta \leq 90°$ at intervals of 5°. Since $0 \leq \alpha_s, \alpha_r \leq 90°$, the argument $(\pi/2) - \alpha_s$ is in the table, and noting that $J_n(re^{-i\theta}) = \bar{J}_n(re^{i\theta})$ the argument $-[(\pi/2) - \alpha_r]$ can also be found there. (The bar denotes the complex conjugate.)

Cases Calculated in This Paper

There are five lengths that enter into the geometric configuration—namely, c_s, c_r, d_s, d_r, and b' (or b). Therefore, in dimensionless form, four ratios made from these lengths must be specified for each configuration. The ratios σ_r, σ_s, d_r/d_s, and b'/c_r have been chosen as the most convenient. It was felt that the effects of variations of the pitch ratio d_r/d_s and the ratio of axial separation to rotor half-chord, b'/c_r, would be the most interesting to investigate, and these two parameters were varied in the numerical calculations, while σ_r and σ_s were held fixed at 1.0.

Since only velocity ratios are involved in the theory, the velocity triangle is determined when α_r and α_s are specified. The only remaining parameter that enters the problem is the ratio of steady circulation, ${}_o\Gamma^r/{}_o\Gamma^s$. In the present paper it is assumed that the steady part of the flow is such as to cause no net turning of the flow through the stage—i.e., the flow leaving the rotor is parallel to that entering the stator. Since the turning angle of a row of equal, equally spaced vortices, ${}_o\Gamma$, is proportional to ${}_o\Gamma/d$, d being the pitch, it is easy to see that the condition of no net turning through the stage requires that

$${}_o\Gamma^r/{}_o\Gamma^s = -d_r/d_s \quad (60)$$

This relates the circulation ratio to one of the previously chosen geometric parameters, the pitch ratio.

The result is that, for no net turning through the stage, it is necessary to specify four geometric ratios, σ_r, σ_s, d_r/d_s, and b'/c_r, and two angles, α_r and α_s, in order to carry out numerical calculations. This is, of course, in addition to the condition of flat-plate or elliptical distribution discussed above.

It is interesting to note that it is not necessary to differentiate between a turbine and a compressor in the calculations, Eq. (60) being valid for either. However, the restriction of the whole theory to thin airfoils and solidities close to unity makes it more realistic for typical compressors than for typical turbines.

For the numerical examples investigated in the present paper, values of the various parameters that are believed to be typical of present-day practice were chosen. Both rotor and stator solidities were fixed at unity, $\sigma_r = \sigma_s = 1$. A 50 per cent reaction stage was

chosen so that $\alpha_r = \alpha_s$, and the angle $\alpha_r = \alpha_s = 45°$ was used. As mentioned above, the effect of variation of the parameters d_r/d_s and b'/c_r was investigated by varying each, holding the other fixed according to the following scheme:

$$b'/c_r = 0.2; \quad d_r/d_s = 0.8, 1.0^*, 1.25$$
$$d_r/d_s = 1.0;^* \quad b'/c_r = 0.2, 0.4, 0.6$$

The first (fundamental) and second harmonics of the rotor and stator lift were calculated for these cases. The moments have not yet been calculated.

The effects of changing from elliptical to flat-plate circulation distribution on the rotor blades were also investigated by performing these calculations for both $A_o{}^r = 0$ (elliptical) and $A_1{}^r = 0$ (flat plate). The condition $A_o{}^s = 0$ (elliptical distribution on the stator blades) was maintained throughout.

* Although the case of equal pitch ($d_r/d_s = 1$) is commonly avoided in practice, this is dictated by considerations of mechanical vibration rather than by purely aerodynamic matters. No singular behavior occurs in the aerodynamics of the rigid cascades treated here at this value of d_r/d_s, and this value is a convenient one to use.

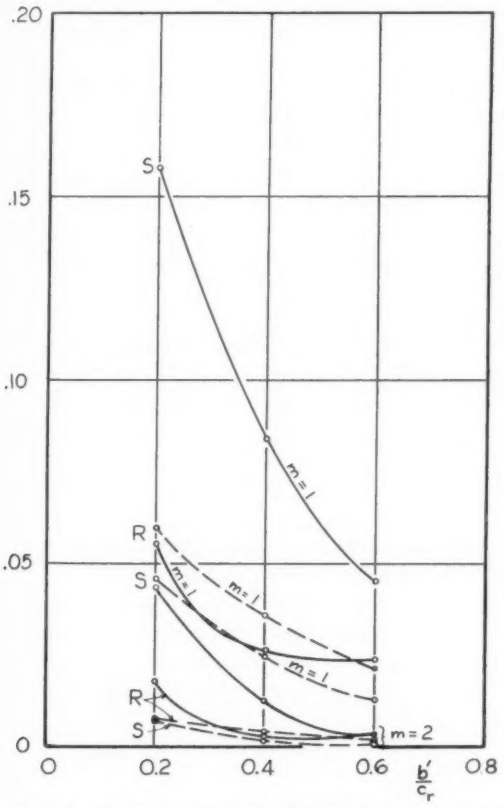

FIG. 5. Absolute values of unsteady lift of rotor and stator blades for $d_r/d_s = 1$, as functions of axial spacing ratio b'/c_r. *Key:* S denotes $|{}_tL^s/{}_oL^s|$ and R denotes $|{}_tL^r/{}_oL^r|$. Dash curves: elliptical steady-state chordwise load distribution on both rotor and stator blades. Solid curves: elliptical steady-state chordwise load distribution on stator blades; flat-plate distribution on rotor blades. $m = 1$: first (fundamental) harmonic. $m = 2$: second harmonic. $2c_r/d_r = 2c_s/d_s = 1$. $\alpha_r = \alpha_s = 45°$.

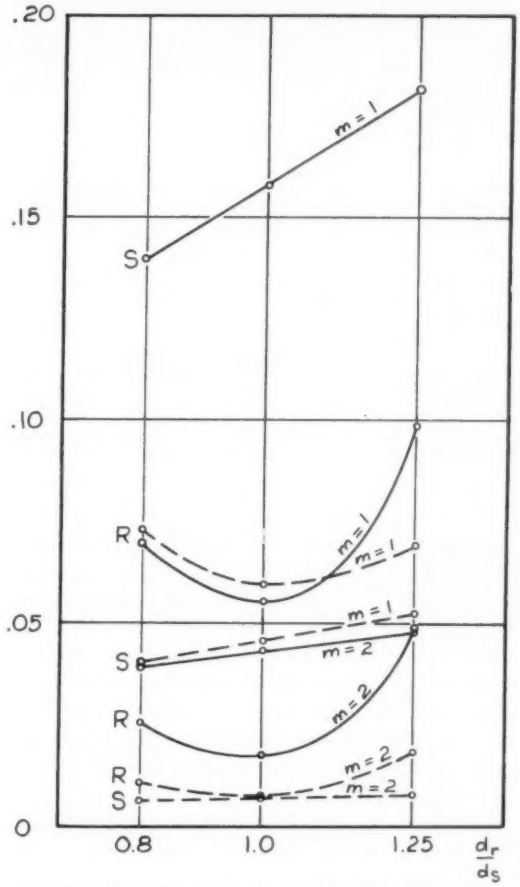

FIG. 6. Absolute values of unsteady lift of rotor and stator blades for $b'/c_r = 0.2$, as functions of pitch ratio d_r/d_s. *Key:* Same as Fig. 5.

It might be mentioned that, since nearly all the numbers involved in the calculations are complex and most of the manipulations involve multiplication, it was found most convenient to express the complex numbers in polar form in carrying out the numerical work.

Numerical values of the Theodorsen function $C(\omega)$ are available from many sources—for instance, from Luke and Dengler.[14] The function $S(\omega)$ may be calculated from its definition, Eq. (8), and the relations[11]

$$K_o(i\omega) = -(1/2)\pi i[J_o(\omega) - iY_o(\omega)]$$
$$K_1(i\omega) = -(1/2)\pi[J_1(\omega) - iY_1(\omega)]$$

RESULTS AND CONCLUSION

The results of the calculations for ${}_tL^s$ and for ${}_tL^r$, which is the sum of ${}_tL^{r1}$ and ${}_tL^{r2}$, are shown in Figs. 5 and 6. The magnitudes of the first two harmonics, $m = 1$ and $m = 2$, of the lift ratio $|{}_tL/{}_oL|$ are plotted against b'/c_r and d_r/d_s for elliptical steady circulation distribution on the stator and for both flat-plate and elliptical distributions on the rotor.

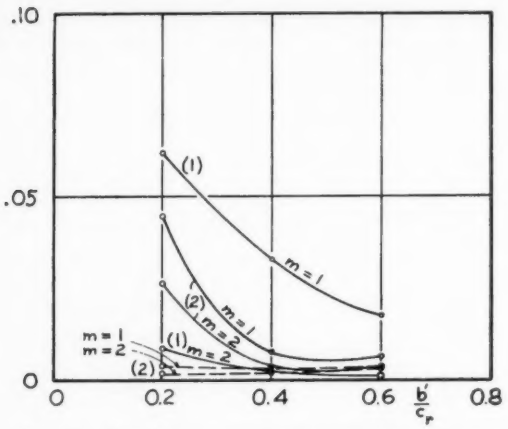

FIG. 7. Absolute values of rotor unsteady lift components for $d_r/d_s = 1$, as functions of axial spacing ratio b'/c_r. *Key:* Same as Fig. 5 except (1) denotes $|{}_tL^{r1}/{}_oL^r|$ and (2) denotes $|{}_tL^{r2}/{}_oL^r|$.

It is seen that the nonsteady part of the lift increases sharply with decreasing b'/c_r, as might be expected from the exponential nature of the factor in which this parameter appears. The change of lift with variation of d_r/d_s is also appreciable. A flat-plate distribution on the rotor blades produces much larger effects on the stator than does elliptical distribution. This is to be expected, since the centroid of the rotor steady bound-vortex distribution is a quarter chord closer to the stator in the flat-plate case than in the elliptical case. The change of rotor steady circulation distribution also affects ${}_tL^r$ somewhat, because ${}_tL^{r2}$ is altered, although ${}_tL^{r1}$ remains unchanged.

A general conclusion to be drawn from the results shown in Figs. 5 and 6 is that the nonsteady part of the lift may be as large as 18 per cent of the steady lift and therefore may be of practical importance, especially with reference to blade vibration.

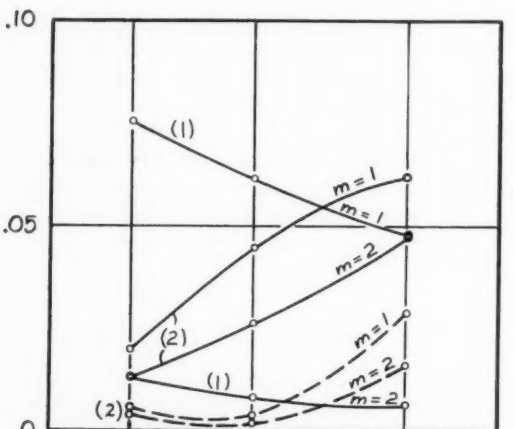

FIG. 8. Absolute values of rotor unsteady lift components for $b'/c_r = 0.2$, as functions of pitch ratio d_r/d_s. *Key:* Same as Fig. 7.

TABLE 1

		Elliptical Steady-State Distribution on Stator and Rotor Blades	Flat-Plate Steady-State Distribution on Rotor; Elliptical on Stator
Stator wake:	$\frac{C_E{}^s}{({}_oC_L{}^s)^2}$	0.00017	0.0069
Rotor wake:	$\frac{C_E{}^r}{({}_oC_L{}^r)^2}$	0.0000042	0.000046

In order to give some idea of the relative sizes of ${}_tL^{r1}$ and ${}_tL^{r2}$, the magnitudes of the first two harmonics of $|{}_tL^{r1}/{}_oL^r|$ and $|{}_tL^{r2}/{}_oL^r|$ are plotted in Figs. 7 and 8 for the same cases that were presented in Figs. 5 and 6. The first two harmonics of ${}_tL^{r1}$ are the $m = 1, 2$ terms of Eq. (50). The first two harmonics of ${}_tL^{r2}$ come from the $k = \pm 1, \pm 2$ terms of the sum over k in Eq. (57), and in the present calculations two terms in the sum over m in that equation were used. It must be remembered that $|{}_tL^r|$ is not the algebraic sum of $|{}_tL^{r1}|$ and $|{}_tL^{r2}|$, because these are the real parts of complex quantities.

It is seen that ${}_tL^{r1}$ and ${}_tL^{r2}$ are comparable in size, especially for flat-plate distribution on the rotor blades, which increases ${}_tL^{r2}$ considerably while, of course, leaving ${}_tL^{r1}$ unchanged. The slower decrease in size of the successive harmonics of ${}_tL^{r2}$, as compared with ${}_tL^{r1}$, as noted above, is also apparent.

Wake Energy

As has already been mentioned, the equations for the rate of transfer of energy to the vortex wakes have been worked out. These have been applied to two of the numerical cases treated above—viz., $d_r/d_s = 1$, $b'/c_r = 0.2$, elliptical distribution on stator blades, and both (a) elliptical and (b) flat-plate distribution on rotor blades. The results are summarized in Table 1, where $C_E{}^s$ and $C_E{}^r$ are the respective coefficients defined by

$$C_E = E/\rho V^2 c$$

E being the (average) rate of energy transfer per unit length of wake per unit width.

These results can easily be converted into the ratios of the energy produced per unit time in the wake to the steady power necessary to turn the rotor, which is ${}_oL^r U \cos \alpha_r$. If the ratios are denoted by P^s and P^r, then

$$P^s = \frac{C_E{}^s}{({}_oC_L{}^s)^2}\left|\frac{{}_o\Gamma^s}{{}_o\Gamma^r}\right|\frac{V_s}{V_r}\frac{{}_oC_L{}^sV_s}{U\cos\alpha_r}, \quad P^r = \frac{C_E{}^r}{({}_oC_L{}^r)^2}\frac{{}_oC_L{}^rV_r}{U\cos\alpha_r}$$

For the cases calculated here,

$$V_s = V_r = U\cos\alpha_r$$
$${}_o\Gamma^s/{}_o\Gamma^r = -d_s/d_r = -1$$

so that

$$P^s = [C_E{}^s/({}_oC_L{}^s)^2]{}_oC_L{}^s, \quad P^r = [C_E{}^r/({}_oC_L{}^r)^2]{}_oC_L{}^r$$

and the numbers given above are precisely the wake-energy power to rotor-power ratios, except for a factor ${}_oC_L$. The power in the vortex wakes is thus seen to be small compared with the power necessary to drive the rotor.

A striking feature of the wake-energy results is the fact that the energy in the stator wake is about 100 times as large as that in the rotor wake. This implies that the nonsteady circulation on the stator blades is about ten times as large as that on the rotor blades, since the wake energy is proportional to $|{}_t\Gamma|^2$. Although this seems surprising at first, it has been verified that, because of the difference in chordwise velocity distribution on the stator (upstream) and rotor (downstream) blades, as indicated by Eqs. (36) and (40), it is indeed true that the nonsteady circulation on the stator is considerably larger than that on the rotor, although the nonsteady lift is approximately the same on both. This can be expected to be a general result—i.e., that the circulation induced on a given row by the relative motion of an adjacent downstream row will be considerably larger than that induced by the adjacent upstream row.

Verification of Basic Assumption

The assumption that $|{}_t\Gamma| \ll |{}_o\Gamma|$, on which the present approximate treatment is based, can also be checked by numerical calculation in order to verify that the theory given in this paper is a consistent one. The expression for ${}_t\Gamma$ for each blade can be found, as mentioned above, from Eqs. (47) and (52), and the general formula for any sinusoidal motion[11]

$${}_t\Gamma(t) = {}_o\Gamma(t)e^{-i\omega}S(\omega)$$

These give

$${}_t\Gamma^s/{}_o\Gamma^s = ({}_o\Gamma^r/{}_o\Gamma^s)\sum_m F_m{}^s e^{-i\omega_s m}S(\omega_s m)$$

$${}_t\Gamma^{r1}/{}_o\Gamma^r = ({}_o\Gamma^s/{}_o\Gamma^r)\sum_m F_m{}^r e^{-i\omega_r m}S(\omega_r m)$$

and a similar expression for ${}_t\Gamma^{r2}$ can be found. An upper limit for $|{}_t\Gamma/{}_o\Gamma|$ is obtained by taking the absolute value of each term in the sum on the right. For the case $d_r/d_s = 1$, $b'/c_r = 0.2$, these upper limits, based on two terms of the series, are shown in Table 2. It appears that for the other cases these numbers would be much the same, so that the basic assumption is well verified by the results of the theory.

Conclusions

An approximate calculation has been carried out, based on the assumptions of incompressible inviscid two-dimensional flow, of the unsteady aerodynamic interference between two cascades of thin airfoils in relative motion. The basic approximation, which is confirmed by the numerical results obtained for typical present-day compressor cascades, is that the unsteady part of the circulation about any blade is small compared with the steady part. Formulas for the unsteady components of lift and pitching moment of rotor and stator blades have been obtained in the form of successive harmonics.

Table 2

	Elliptical Steady-State Distribution on Stator and Rotor Blades	Flat-Plate Steady-State Distribution on Rotor; Elliptical on Stator
$\lvert {}_t\Gamma^s/{}_o\Gamma^s \rvert$	0.02	0.13
$\lvert {}_t\Gamma^r/{}_o\Gamma^r \rvert$	0.0027	0.030

The limited numerical results presented here indicate that:

(1) The fundamental harmonic component of variable lift varies in magnitude from 1 to 18 per cent of the steady value, depending especially on the axial distance between rows and on the chordwise distribution of steady circulation of the blades of the other row.

(2) The second harmonic component of variable lift is considerably smaller than the fundamental.

(3) The contribution to rotor lift of the vortex wakes shed by stator blades, through which the rotor blades pass, is comparable in size to the effect induced by the stator blades themselves.

(4) The fluctuating part of the circulation, expressed as a ratio to the steady part, is several times as large for stator (upstream) blades as for rotor (downstream) blades, even though the corresponding ratio of lifts is about equal.

(5) The rate of transfer of energy into the vortex-wake pattern which results from the variable circulation is small compared with the power required to turn the rotor. It is about 100 times as large for the stator (upstream) blades as for the rotor (downstream) blades.

References

[1] Wu, Chung-Hua, *Survey of Available Information on Internal Flow Losses Through Axial Turbomachines*, NACA RM E50J13, January 26, 1951.

[2] Keller, C., *Kinetic Energy Losses Behind Blade Grids, as a Result of Periodic Variation in the Circulation*, Rep. Inst. Aero., Tech. Hochschule (Zürich), pp. 167–187, 1934. (Also available as RTP Trans. No. 1883, British M.A.P.)

[3] von Kármán, Th., and Sears, W. R., *Airfoil Theory for Non-Uniform Motion*, Journal of the Aeronautical Sciences, Vol. 5, No. 10, pp. 379–390, August, 1938.

[4] Sears, William R., *Some Aspects of Non-Stationary Airfoil Theory and its Practical Application*, Journal of the Aeronautical Sciences, Vol. 8, No. 3, pp. 104–108, January, 1941.

[5] von Kármán, Th., and Burgers, J. M., *General Aerodynamic Theory—Perfect Fluids*, Vol. II of *Aerodynamic Theory*, W. F. Durand (Ed.); Julius Springer, Berlin, 1935. (Also available from Durand Reprinting Committee, Pasadena, Calif., 1943.)

[6] Theodorsen, Theodore; *General Theory of Aerodynamic Instability and the Mechanism of Flutter*, NACA TR 496, 1935.

(*Concluded on page 612*)

Stall-Flutter in Cascades*

F. SISTO†

Wright Aeronautical Division, Curtiss-Wright Corporation

ABSTRACT

Assuming the complex of oscillatory aerodynamic reactions to be small compared with blade inertia and elastic forces, some results from nonlinear mechanics are utilized to develop a convenient method of studying stall-flutter oscillations. This represents a new approach to the problem.

Data are presented from an exploratory experimental investigation of a "two-dimensional" cascade in which one blade and later three blades are flexibly mounted. The variation of flutter amplitude with stream velocity and mean incidence is obtained for angles of attack near the static stall. Experimental determinations are given for three different gap/chord ratios. The motion is predominantly torsional.

The results confirm certain deductions from the nonlinear theory concerning transient behavior and equilibrium flutter amplitudes or "limit-cycles." Other qualitative results are reported which confirm the necessity of adopting this general approach in order to explain the important features of stall-flutter phenomena.

INTRODUCTION

THE FATIGUE AND EVENTUAL FAILURE of the aerodynamic blading in axial-flow compressors is often attributable to stall-flutter oscillations. At the large mean angles of attack where this type of vibration is encountered, the flow about the blade is separated during the whole, or at least a part, of the cycle of oscillation. Because of the difficulty involved in the aerodynamics of unsteady stalled flow most of the previous work has been wholly experimental[1] or has consisted of empirical and semiempirical[2–4] modifications of classical flutter theory.

In the sequel, the nonlinearities in the oscillatory aerodynamic reactions are considered directly by standard methods of nonlinear mechanics.

Finally, the results of an exploratory experimental investigation are presented in corroboration of the gross features of compressor blade stall-flutter phenomena. Eventually, this general method, in conjunction with suitable experimental work, should lead to reliable quantitative information.

PRELIMINARY CONSIDERATIONS

Certain simplifications that appear to be allowable in the turboblade problem consist in assuming that (1) the ratio of air density to blade density is small and consequently, (2) the unsteady aerodynamic forces may be taken to be small compared with the elastic and inertia forces of the blade, (3) the frequency of flutter will be close to the natural frequency of the blade in the predominant normal mode, and (4) the equilibrium motion of a sustained flutter condition will be "nearly sinusoidal" in the principal mode.

For simplicity we consider only a single degree of freedom system acted upon by two-dimensional aerodynamic forces.

Under the previous assumptions, the differential equation of motion (either pure torsional or pure translational degree of freedom) is

$$\ddot{x} + \omega\delta\pi^{-1}\dot{x} + \omega^2 x = F(x, \dot{x}) \qquad (1)$$

where ω is the natural frequency of the system, δ is the logarithmic decrement *in vacuo*, and F is the ratio of the small aerodynamic forces to the system inertia (mass or moment of inertia).

Presupposing a "nearly harmonic" solution of the form

$$x = x_0 \cos \omega t \qquad (2)$$

where x_0 is a slowly varying quantity, it is possible to arrive at an approximate expression for the rate of change of amplitude

$$\dot{x}_0 = -(2\pi x_0\omega)^{-1} \int_0^{2\pi} [F(x_0 \cos \tau, -x_0\omega \sin \tau) + \omega^2\delta x_0\pi^{-1} \sin \tau] \sin \tau \, d\tau \qquad (3)$$

by an energy consideration[5] or by one of the standard methods of nonlinear mechanics.[6, 7]

The equilibrium flutter amplitudes consequently are given by the condition

$$\int_0^{2\pi} [F(x_0 \cos \tau, -x_0\omega \sin \tau) + \omega^2\delta x_0\pi^{-1} \sin \tau] \sin \tau \, d\tau = 0 \qquad (4)$$

where only the real positive values of x_0 satisfying this equation are significant. Whether these values of x_0 represent stable‡ or unstable motions is determined by the criterion

$$\left.\begin{aligned} \frac{\partial \dot{x}_0(x_0)}{\partial x_0} &< 0 \qquad \text{stable} \\ \frac{\partial \dot{x}_0(x_0)}{\partial x_0} &> 0 \qquad \text{unstable} \end{aligned}\right\} \qquad (5)$$

Presented at the Flight Propulsion Session, Twenty-First Annual Meeting, IAS, New York, January 26–29, 1953.

* Portions of this paper are from an Sc.D. Thesis investigation conducted at the Gas Turbine Laboratory, Massachusetts Institute of Technology. Permission to include these portions is gratefully acknowledged.

† Assistant Project Engineer.

‡ Stability according to Liapounoff.[6]

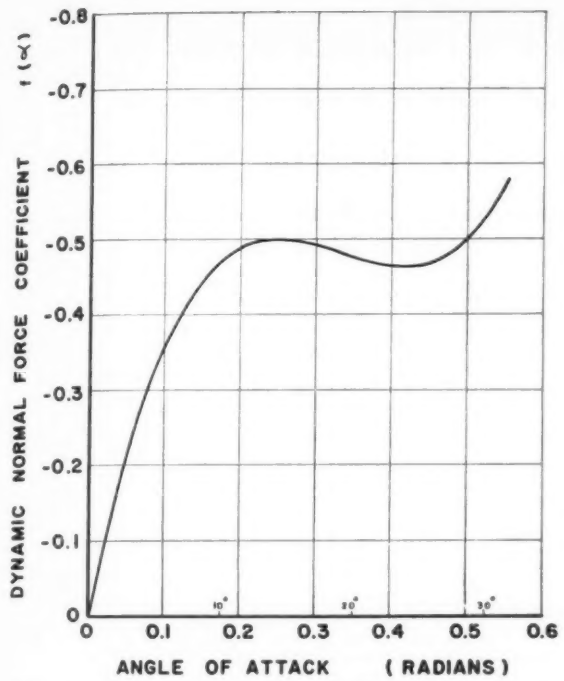

FIG. 1. Mean dynamic normal force coefficient for the illustrative example in pure bending stall-flutter.

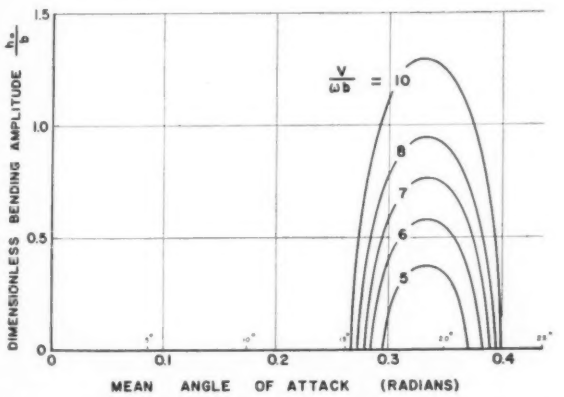

FIG. 2. Flutter amplitude in pure bending as a function of angle of attack and reduced velocity.

Hence, the stable equilibrium flutter amplitudes may be obtained to a first approximation within the accuracy of the aerodynamic reaction $F(x, \dot{x})$.

Experimentally,[2, 8] F is known to be a more or less complicated function that exhibits an aerodynamic lag or "hysteresis" effect. For the time being it is convenient to ignore this hysteresis and to suppose that a single-valued mean dynamic characteristic exists. This characteristic is either aerodynamic moment or normal force as a function of instantaneous angle of attack. The angle of attack, however, is a function of blade velocity transverse to the air stream, so that a certain amount of "hysteresis" reappears in the aerodynamic reactions.

PURE BENDING STALL-FLUTTER

The previous concepts are best illustrated by some simple examples. A pure bending stall-flutter will be considered first. In this case put

$$x = h, \quad x_0 = h_0, \quad \text{etc.} \tag{6}$$

and

$$F(h, \dot{h}) = F(\dot{h}) = 2qbf(\alpha)/m \tag{7}$$

where α is the instantaneous angle of attack and is given by

$$\alpha = \alpha_i + (\dot{h}/V) \tag{8}$$

In these expressions b is the blade semichord, V is the mean stream velocity at upstream infinity, q is the dynamic pressure based on this velocity, α_i is the mean value of α, and m is the blade mass per unit span.

Assume, for the purposes of this example, that f may be expressed as a polynomial

$$f(\alpha) = \sum_{n=1}^{N} a_n \alpha^n \tag{9}$$

where the a_n could be adjusted to fit the mean dynamic characteristic if this characteristic were known. Retaining the first three terms and applying the previous development, the expression for the stable equilibrium flutter amplitudes (limit-cycles) in pure bending is

$$(h_0/b)^2 = 8[f'''(\alpha_i)]^{-1} \times \left[-f'(\alpha_i) + \left(\frac{m}{\pi\rho b^2}\right)\left(\frac{\omega b}{V}\right)(\delta)\right]\left[\frac{V}{\omega b}\right]^2 \tag{10}$$

where ρ is the air density. Only positive values of the right-hand side of Eq. (10) are significant.

Taking $a_1 = -5$, $a_2 = 16$, $a_3 = -16$, for instance, defines the mean dynamic normal force coefficient illustrated in Fig. 1. The stable equilibrium flutter amplitudes are shown in Fig. 2 in nondimensional form for various values of the reduced velocity $V/(\omega b)$, and with

$$(m/\pi\rho b^2)(\delta) = 4/3$$

Further, if $V/(\omega b)$ is cross-plotted against α_i for constant values of h_0/b, the conventional "critical" flutter velocity diagram illustrated in Fig. 3 is obtained. The term "critical" is somewhat misleading, since the flutter condition may or may not develop explosively as a governing parameter is slowly varied. In the present instance of so-called soft flutter, the amplitude grows smoothly from zero as the flutter boundary is traversed by means of slowly varying the air-stream velocity or angle of attack. In hard flutter, on the other hand, the amplitude may suddenly jump to a finite value.

Pure Torsional Stall-Flutter

Pure torsional stall-flutter, by a similar analysis, proves to be somewhat more complicated, since the instantaneous angle of attack due to rotational velocity is a strong linear function of position along the blade chord. By way of illustrating certain other features, however, put (with $x = \theta$, $x_0 = \theta_0$, etc.)

$$\alpha = \alpha_i + \theta + (nb\dot{\theta}/V) \tag{11}$$

where n is so chosen as to give the instantaneous angle of attack at the three-quarter chord point. (This convention is taken over directly from classical flutter theory[9] as a crude approximation in stall-flutter.)

Then, taking

$$F(\theta, \dot{\theta}) = 4qb^2g(\alpha)/I \tag{12}$$

and assuming a fifth degree polynomial for g

$$g(\alpha) = \sum_{n=1}^{5} b_n\alpha^n \tag{13}$$

there results, after a similar reduction, the expression for the limit-cycles in pure torsional flutter

$$\theta_0^2 = 12\,\frac{(V/\omega b)^2}{n^2 + (V/\omega b)^2}\left\{-\frac{g'''(\alpha_i)}{g^{V}(\alpha_i)} \pm \sqrt{\left[\frac{g'''(\alpha_i)}{g^{V}(\alpha_i)}\right]^2 - \frac{2}{3ng^{V}(\alpha_i)}\left[2ng'(\alpha_i) - \left(\frac{I}{\pi\rho b^4}\right)\left(\frac{\omega b}{V}\right)(\delta)\right]}\right\} \tag{14}$$

where I is blade moment of inertia about the elastic axis per unit span.

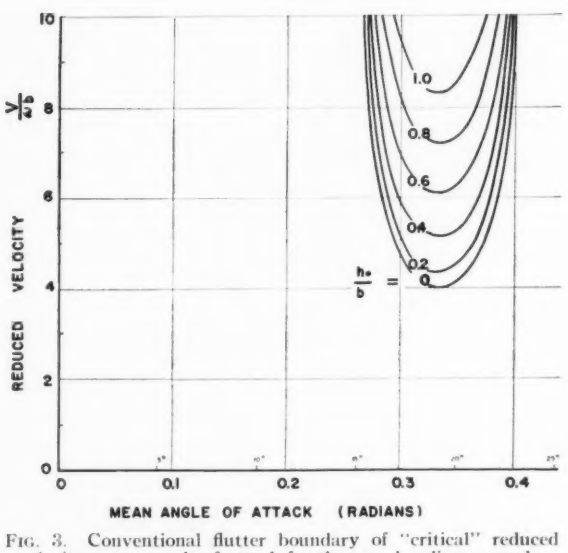

FIG. 3. Conventional flutter boundary of "critical" reduced velocity versus angle of attack for the pure bending example.

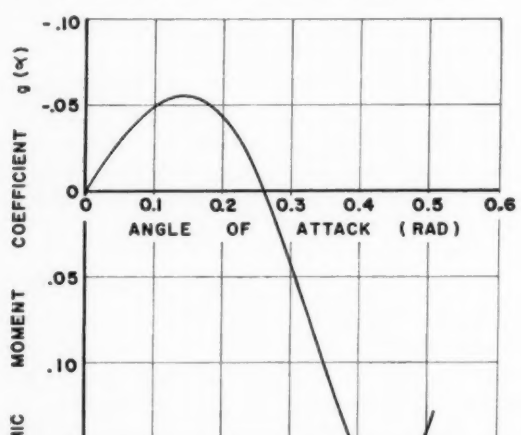

FIG. 4. Mean dynamic moment coefficient for the illustrative example in pure torsional stall-flutter.

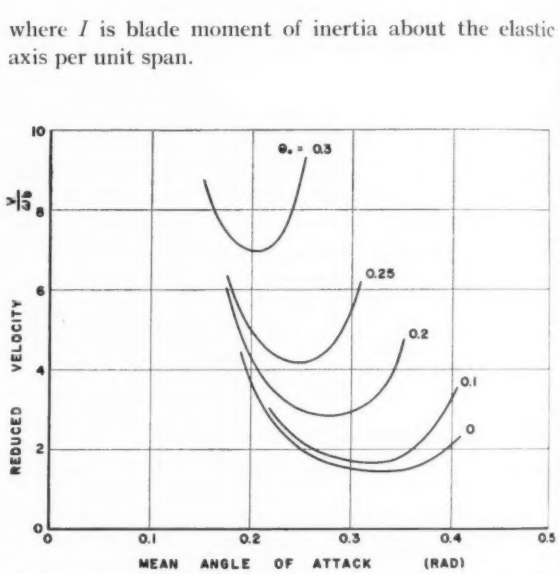

FIG. 5. Flutter boundary with contours of constant amplitude for pure torsional flutter.

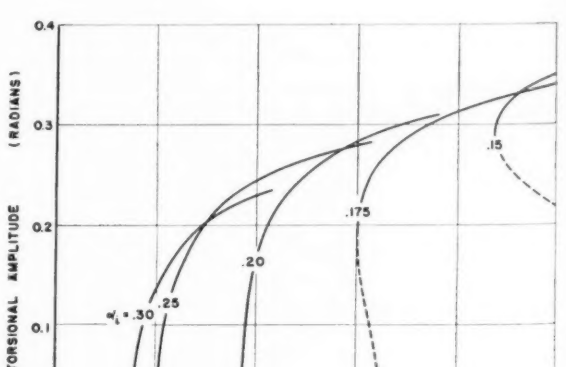

FIG. 6. Torsional amplitude as a function of reduced velocity for various angles of attack in pure torsional example.

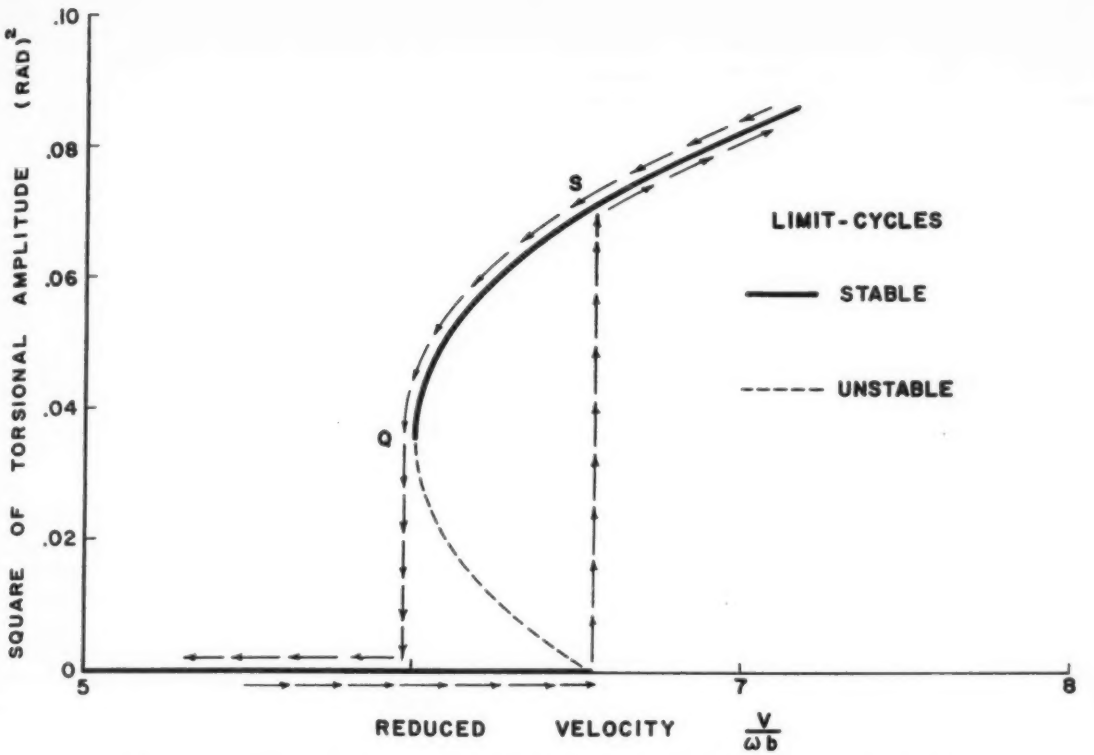

FIG. 7. "Hysteresis" loop in amplitude versus velocity obtainable in hard flutter ($\alpha_r = 0.175$).

The results of calculations for an illustrative case in which

$$n = 0.85$$
$$b_2 = b_4 = 0$$
$$b_1 = -3/5, \quad b_3 = 11, \quad b_5 = -30$$
$$(I/\pi\rho b^4)(\delta) = 3$$

are shown in Figs. 4, 5, and 6. Data similar to Fig. 5 were obtained in the earliest stall-flutter experiments by Studer.[1] Fig. 6 is included to indicate the possibility of hard flutter. The dotted lines are unstable limit-cycles according to the inequalities (5). If, for a given angle of attack and air-stream velocity, the operational point lies in this region of the figure, the blade will remain at rest unless impulsively started with an amplitude greater than the dotted portion of the curve. This situation is illustrated in Fig. 7, which indicates that it is possible to traverse a "hysteresis" loop of a different kind by cyclically changing the velocity.

Effect of Cascading

Embedding a single blade in an infinite cascade of similar blades gives rise to two effects:

(1) The shape of the mean dynamic force characteristic is changed because of the proximity of other blades.

(2) The movement of these adjacent blades further modifies the "instantaneous" characteristic, in addition to giving rise to possible transient effects that travel along the cascade (i.e., progress from blade to blade).

In the first case F becomes a function of blade spacing and stagger in addition to x and $\dot{x}$. In the second case the displacement and velocity of all the additional blades must enter into F.

Experimental Results

Considering only the first type of cascading effect, experiments[5] were conducted in a low-speed cascade tunnel in which all blades but the central one were rigidly attached to the tunnel walls. The central steel blade was flexibly mounted on springs to allow independent motion in torsion and bending, the blade itself

TABLE 1
Experimental Blade Constants

a	$= -0.35$
b	$= 0.112$ ft.
x_θ	$= 0.192$
ω_θ	$= 170$ rad. per sec.
ω_h	$= 48.6$ rad. per sec.
I_θ	$= 1.74\ (10^{-4})$ slug-ft.²/ft. span
M_h	$= 0.065$ slug/ft. span
M_θ	$= 0.050$ slug/ft. span
Profile	NACA 6 1/2 409
Blade span	5.5 inches
log $dec\ \delta_\theta$	< 0.05
log $dec\ \delta_h$	< 0.01

being completely rigid by comparison. The constants of the system, in the Theodorsen notation,[9] are listed in Table 1. Structural and aerodynamic conditions were substantially "two-dimensional." Data were obtained by means of electric resistance strain gage pick-ups attached to the springs. The signals from the gage bridges were amplified and recorded on conventional oscillographic equipment.

The results of this investigation are illustrated in Figs. 8, 9, and 10 for three different gap/chord ratios at zero stagger. While exact correspondence with the illustrative example is not to be expected, general curve shapes and broad trends are substantially as predicted. Two influences that cause deviations from predicted variation are: (1) the coexistence of bending motion in some regions of the curves (datum points with "tails") and (2) the degree of approximation involved in using a fifth-degree characteristic. (Time-average values of moment in pure pitch determined experimentally in reference 2 indicate that the use of a seventh- or ninth-degree polynomial would greatly improve the representation of a mean dynamic moment coefficient.) The effects of bending motion on torsional amplitude may be explained satisfactorily if it is assumed that the aerodynamic reactions due to this bending motion do positive work on the blade in the regions where the torsional amplitude is larger than the theoretical type of variation would predict.

The self-starting (e.g., point S in Fig. 7) and quenching (e.g., point Q in Fig. 7) limits could not be determined accurately. A certain amount of residual coulomb damping in the torsional spring supports made it impossible to obtain a completely soft pure torsional flutter. Furthermore, a close examination of some of the starting transients indicated that in some cases a soft bending flutter was sufficient to start the torsional mode into vibration. The resulting steady amplitude torsional flutter completely obscured the important "triggering" effect of the bending instability.

This characteristic of nonlinear systems is referred to as asynchronous excitation and quenching,[7] the term "asynchronous" denoting that there is no relation between the frequencies of the two oscillations (bending and torsion).

The second type of cascading effect is illustrated by two series of experimental determinations conducted with three spring-mounted blades. The results of one such series is compared in Fig. 11 with the result for a single spring-mounted blade. In addition to showing a consistent reduction in amplitude at this particular mean angle of attack, the records for the three fluttering blades indicated either an amplitude or a frequency

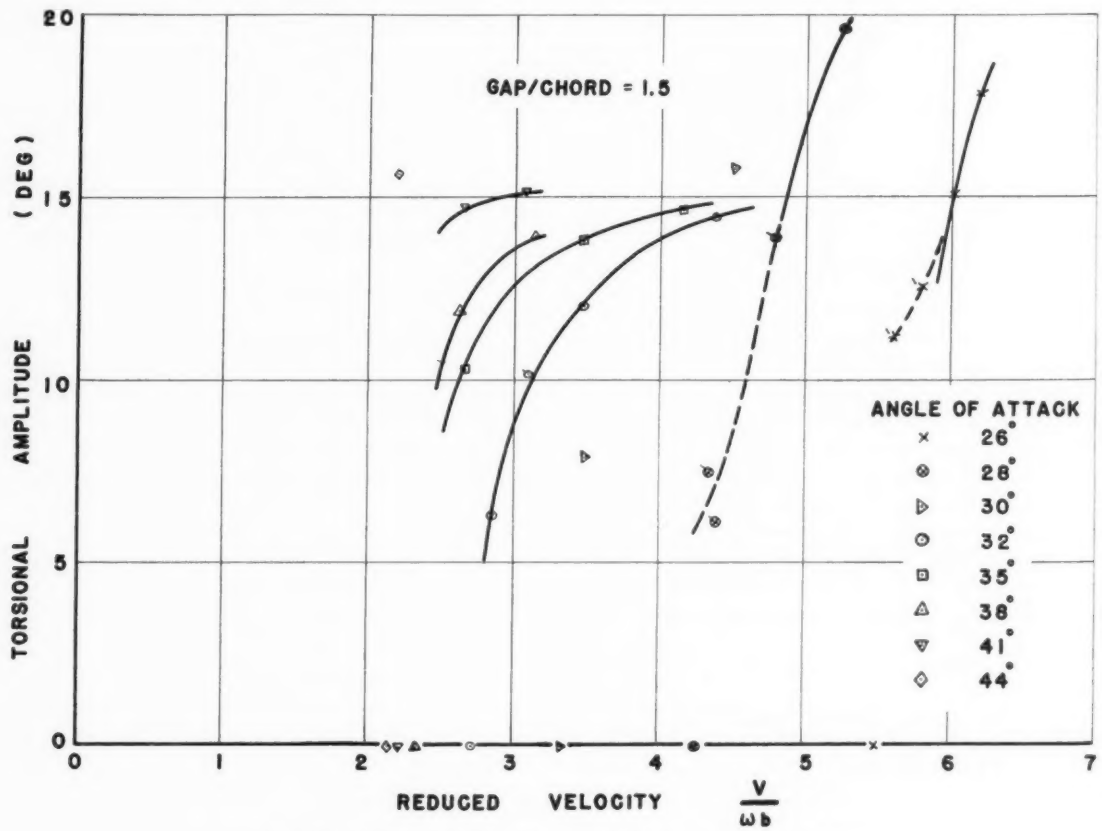

FIG. 8. Experimental torsional amplitudes for gap/chord = 1.5.

TORSIONAL AMPLITUDE (DEG)
TORSIONAL AMPLITUDE (DEG)

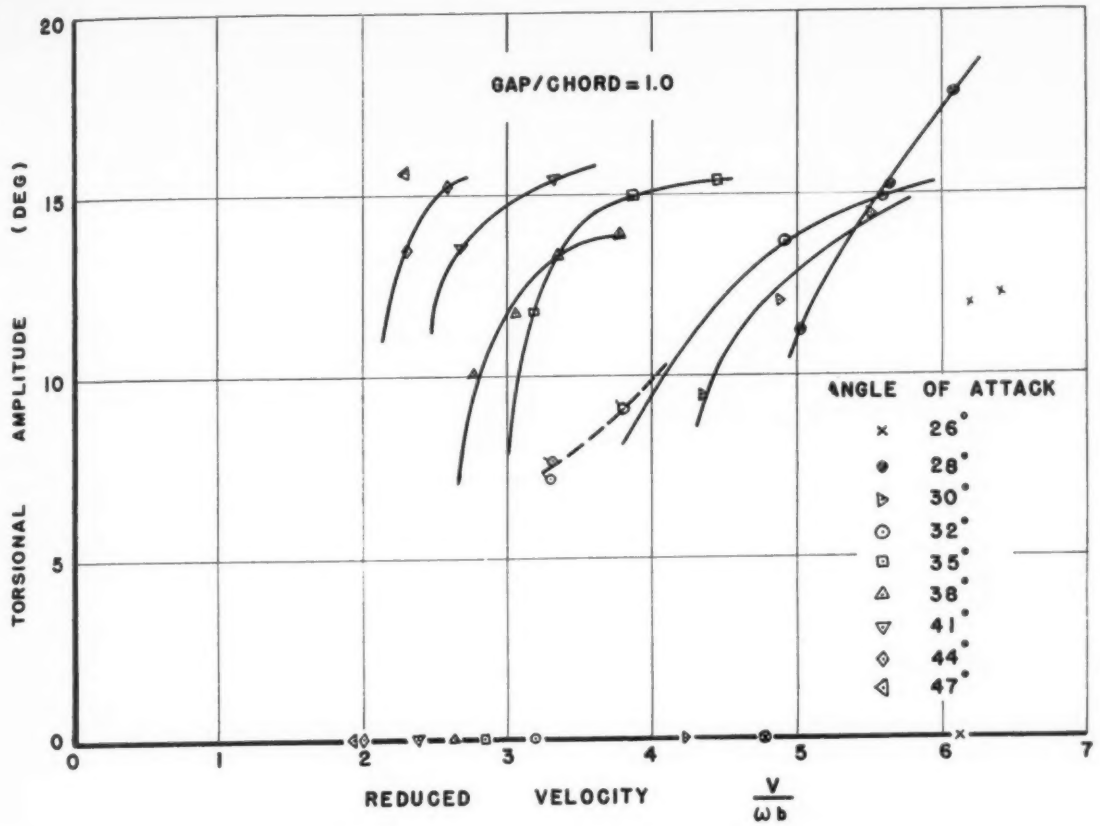

FIG. 9. Experimental torsional amplitudes for gap/chord = 1.0.

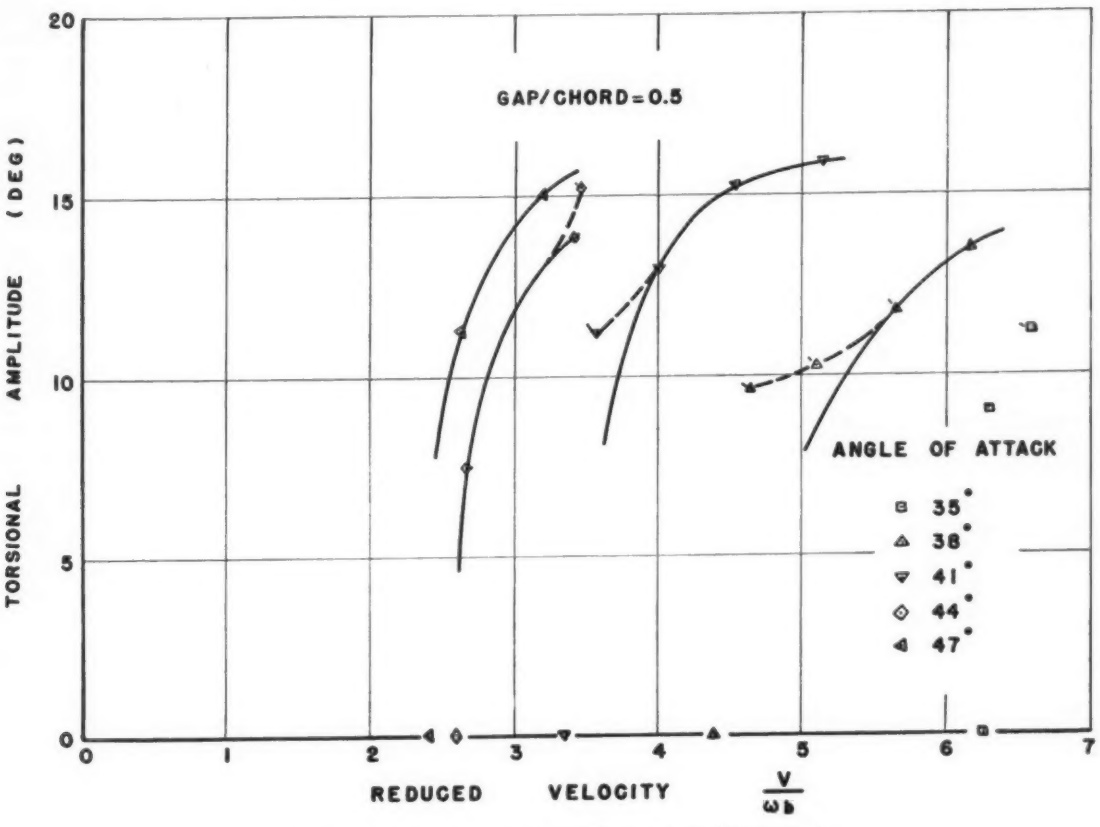

FIG. 10. Experimental torsional amplitudes for gap/chord = 0.5.

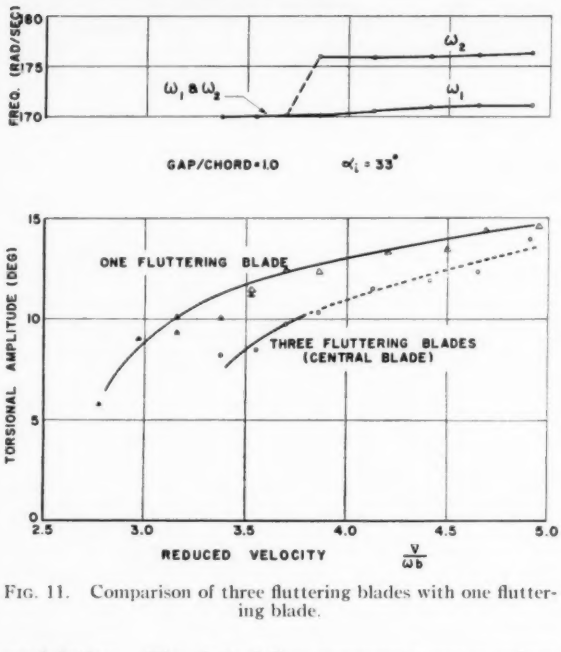

FIG. 11. Comparison of three fluttering blades with one fluttering blade.

modulation. The dotted line represents mean values of the amplitude modulated wave form. The frequencies in the upper portion of the diagram refer to the configuration with three flexibly mounted blades, ω_1 being the frequency of the central or reference blade and ω_2 the frequency of the adjacent blade on the convex side of the reference. The point where the two frequencies separate corresponds to the onset of the amplitude modulation mentioned before. Below this point the frequencies recorded are long-time averages (i.e., over several cycles of frequency modulation). The phenomenon exhibited by the two separate frequencies ω_1 and ω_2 is known as synchronization or entrainment of frequency and is predicted by nonlinear theory.[7]

Fig. 11 also affords a particularly accurate determination of amplitude variation with velocity. The similarity with predicted curve shape is apparent.

Extension of the Method

The experimental investigation indicates a serious handicap in considering a single degree of freedom system theoretically; aerodynamic and mass coupling phenomena are automatically excluded. The analysis for a two degree of freedom system, including first-order coupling effects, may be performed by applying the Method of Equivalent Linearization.[10] When sufficient experimental data become available to warrant their use, the general method may be extended in this direction.

Another approach to aerodynamic coupling in cascades presupposes each blade to have only one degree of freedom. In this case each blade is an "identical" element, and the analogy may be drawn to infinite lattices of identical coupled circuits in network theory. The problem may then be attacked by the successive application of: the Method of Equivalent Linearization, the Method of Complex Amplitudes, and the theory of linear difference equations.

Finally, when the stage is reached where it is desired to determine the mean dynamic aerodynamic characteristics (i.e., f and g or their counterparts) from experimental data, it is not necessary to assume polynomial representations for these functions. On the contrary, it is desirable to expand each in Taylor series about α_i, terminate the series at some convenient point, and pursue the analysis as before. The experimental data may then be used to solve for the first derivative, and the form of f (or g) may be obtained within an additive constant by graphical integration.

References

[1] Studer, H. L., *Experimentelle Untersuchungen über Flugelschwingungen*, Mitteilungen aus dem Institut fur Aerodynamik, Eidgenossische Technische Hochschule, Zurich, No. 4/5, 1936.

[2] Halfman, R. L., et al., *Evaluation of High-Angle-of-Attack Aerodynamic-Derivative Data and Stall-Flutter Prediction Techniques*, NACA TN No. 2533, November, 1951.

[3] Victory, M., *Flutter at High Incidence*, R. & M. No. 2048, British A.R.C., January, 1943.

[4] Mendelson, A., *Aerodynamic Hysteresis as a Factor in Critical Flutter Speed of Compressor Blades at Stalling Conditions*, Journal of the Aeronautical Sciences, Vol. 16, No. 11, pp. 645–652, November, 1949.

[5] Sisto, F., *Flutter of Airfoils in Cascade*, Sc.D. Thesis, M.I.T., Cambridge, September, 1952.

[6] Andronow, A. A., and Chaikin, C. E., *Theory of Oscillations;* Princeton University Press, Princeton, N.J., 1949.

[7] Minorsky, N., *Introduction to Nonlinear Mechanics;* J. W. Edwards, Ann Arbor, 1947.

[8] Farren, W. S., *The Reaction on a Wing Whose Angle of Incidence is Changing Rapidly*, R. & M. No. 1648, British A.R.C., 1935.

[9] Theodorsen, T., *General Theory of Aerodynamic Instability and the Mechanism of Flutter*, NACA Report No. 496, April 1935.

[10] Kryloff, N. M., and Bogoliuboff, N., *Introduction to Nonlinear Mechanics* (a free translation by S. Lefschetz); Princeton University Press, Princeton, N.J., 1943.

An Exact Solution for the Buckling Load of Flat Sandwich Panels with Loaded Edges Clamped*,†

S. V. NARDO‡

Polytechnic Institute of Brooklyn

SUMMARY

This paper presents an exact solution for the buckling load of flat rectangular plates whose loaded edges are clamped and unloaded edges simply supported. The theory is also shown to be applicable for the case in which unloaded edges are clamped and loaded edges simply supported.

The solution is based on small deflection theory, and it is assumed that the stresses are always below the proportional limit. The material for both the faces and the core is considered isotropic. Three equations of equilibrium, derived by means of the principle of virtual displacements, form the starting point of the theory. The equilibrium equations are partial linear differential equations with constant coefficients—two are of the second order, and the third is of the fourth order. Both the equations of equilibrium and 16 boundary conditions are satisfied identically.

Numerical calculations have been made for the case of loaded edges clamped. A series of design charts is presented which gives the buckling load as a function of the plate aspect ratio and the ratio of core to plate thickness. Each curve is valid for a particular value of a parameter representing the ratio of shear rigidity to bending rigidity. Values of this latter parameter, which are four in number, are chosen to span the range encountered in most practical applications.

A check with experiments run at the Forest Products Laboratory indicates that the theory is in reasonable agreement with the experimental results.

SYMBOLS

$2a, 2b$ = edge lengths of sandwich panel, in.
c = core thickness, in.
C = buckling coefficient, $\sigma_{cr}/F\sigma_{cr_0}$
E = Young's modulus, lbs. per sq.in.
F = $1 + 3[(c/t) + 1]^2$
G = shear modulus, lbs. per sq.in.
h = total thickness of sandwich plate, in.
n = number of half waves in sandwich plate in x or y direction
P_{cr} = critical value of edge load, lbs. per in.
R = relative rigidity parameter, $12(1 - \nu^2)Ga^2/Et^2$
t = face thickness, in.
u, v, w = sandwich plate displacements, in.
x, y, z = coordinate system for sandwich plate
ξ, η, ζ = nondimensional coordinate system for sandwich plate
λ = critical load coefficient
ν = Poisson's ratio
σ_{cr} = buckling stress of sandwich plate, lbs. per sq.in.
σ_{cr_0} = buckling stress of two independent faces, lbs. per sq.in., $\pi^2 Et^2/3(1 - \nu^2)(2a)^2$

Presented at the Structures Session, Twenty-First Annual Meeting, IAS, New York, January 26–29, 1953.

* This paper is based upon a thesis submitted to the Polytechnic Institute of Brooklyn in partial fulfillment of the requirements for the degree of Doctor of Philosophy (in Applied Mechanics).

† The work here described was started in connection with a contract awarded to the Polytechnic Institute of Brooklyn by the National Advisory Committee for Aeronautics. It was completed by the author with the aid of funds provided by the Polytechnic Institute of Brooklyn. The author is grateful to these organizations for the financial aid received. He also acknowledges his indebtedness to his thesis advisers, Profs. N. J. Hoff and V. L. Salerno, and to Burton Erickson, Ivan Rattinger, and Dominick Torrillo for their assistance in carrying out part of the numerical calculations.

‡ Assistant Professor of Aeronautical Engineering.

INTRODUCTION

THE TERM "SANDWICH CONSTRUCTION" generally refers to a flat or curved load-carrying surface, composed of two thin high-strength faces on either side of a comparatively thick low-weight low-strength core. In aircraft practice, aluminum alloy has been widely used for face material, but also suitable in certain applications are Papreg or Fiberglas. Balsawood, oriented in such a manner that the fibers are perpendicular to the faces, has been popular as a core material. Cores have also been made of expanded synthetic materials and built-up square or honeycomb grids of the same material as the faces. Considerable research has been conducted to develop a more satisfactory core material—i.e., a core material with relatively high strength compared to its weight.

The modulus of elasticity of the core in the plane of the faces may be as low as one-thousandth of that of the faces. As a consequence, the normal stresses developed in the core can be neglected in comparison with those developed in the face material, even though the ratio of core to face thickness may lie between 10 and 100. The core, however, is counted upon to transmit shearing forces. Because of the core's low shear modulus, considerable shearing deformations take place which cannot be disregarded as they are in the case of thin plate theory.

Toward the end of, and immediately following, World War II, considerable work was done in the field of sandwich construction. Many airplanes have been designed utilizing sandwich-type construction for the major structural components. For this reason the

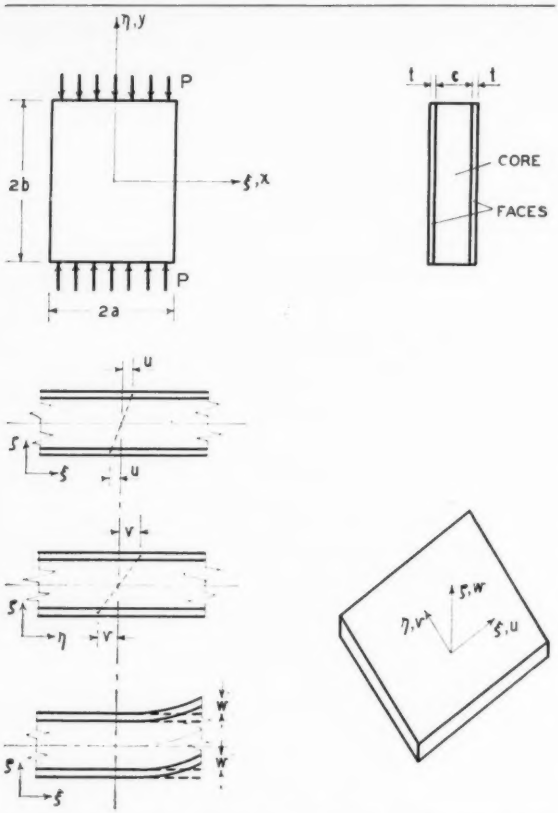

FIG. 1. Notation for coordinate system displacements and loading.

strength of sandwich construction was also investigated, and various theories were proposed for the analysis of sandwich plates.

The first among these was one developed by Leggett and Hopkins[1] in 1942, which was followed by the theory of Van der Neut[2] in 1943. These two investigators derived differential equations, while March and Smith[3] used the strain-energy approach in 1945. A simplified procedure was suggested by Bijlaard[4] in 1946, and in 1948 Reissner,[5] as well as Libove and Batdorf[6] presented new sets of differential equations. These were followed by Hoff's[7] theory, which is the basis of the present investigation.

Most of the work cited dealt with sandwich plates having simple supports along all four edges, because this condition leads to particularly simple solutions. The condition of simple supports along the unloaded edges and rigid clamping along the loaded edges has been given much less attention.

This boundary condition, as well as the one in which the unloaded edges are clamped and the loaded edges simply supported, was first solved for ordinary (not sandwich-type) thin plates by Schleicher in 1931.[8, 9] Schleicher assumed that the deflected shape of the plate could be expressed as the product of an unknown function in the loaded direction and a trigonometric function in the unloaded direction. Substitution of this function into the partial differential equation of equilibrium reduced it to an ordinary differential equation in the unknown function. Enforcement of the boundary conditions led to a set of two linear homogeneous equations whose denominator determinant was required to vanish if the solution was to be nontrivial. Since the elements of the determinant contained the edge load, this gave a condition yielding the critical load.

An exact solution to the buckling of flat plywood plates was published in 1944 by R. C. T. Smith.[10] Again it was assumed that in the expression for the deflected shape the variables separate. The solution for this plywood plate-buckling problem was given for a number of boundary conditions exactly. In the case of all four edges clamped, however, a Rayleigh-Ritz procedure was utilized.

In 1945, March and Smith[3] gave the strain-energy solution to the buckling of flat sandwich plates, loaded edgewise in one direction, under various edge conditions. The plates were considered orthotropic. The procedure involved was a straightforward energy method, the work done by the edge load being equated to the strain energy of bending of the panel. Curves were presented for all cases and for various degrees of orthotropy.

STATEMENT OF PROBLEM AND BASIC ASSUMPTIONS

The problem investigated in the present paper is the exact solution to the buckling load of a flat sandwich panel, loaded edgewise in one direction, with loaded edges clamped and unloaded edges simply supported. The method used in the solution is also satisfactory when the boundary conditions are reversed— i.e., the loaded edges are simply supported and the unloaded edges clamped.

Hoff's differential equations were used in the analysis because they represent the behavior of sandwich plates more accurately than the theories in which the sandwich plate is replaced by a homogeneous thin plate weak in shear. At the same time, they are not so difficult to solve as the theories in which the sandwich plate is treated rigorously as the assembly of three interconnected plates. These equations have already been solved for the cases where all the four edges are simply supported[7] and when the loaded edges are simply supported and the unloaded edges rigidly clamped.[11]

This theory assumes that the deflections are small and the stresses are less than the proportional limit. The edge load is applied only to the faces and not to the core.

In the derivation of the equations of equilibrium, the following strain-energy quantities were considered: (1) strain energy due to extension and shear of the faces in their own plane; (2) strain energy of bending of the faces; and (3) shear strain energy of the core.

Note that any strain energy due to transverse shearing of the faces and to extensions in the core parallel or perpendicular to the faces was considered negligible.

The displacements are described by means of three variables u, v, and w as functions of the independent variables, ξ and η, the coordinates in the plane of the plate. These latter coordinates are nondimensional and are chosen in such a manner that the edges of the sandwich plate coincide with ξ and $\eta = \pm 1$. A sketch of the loading, coordinate system, and displacements is shown in Fig. 1. Note that u represents a displacement in the positive ξ direction in the upper face and an equal but opposite displacement in the lower face. The v displacements are similarly defined, except that they obtain in the η direction. The plane of the plate becomes curved only during w displacements.

Theoretical Solution

The equations of equilibrium as derived in reference 7, after setting the transverse load and the edge load acting in the $x(\xi)$ direction equal to zero, may be written as follows:

$$-B_0[2(\partial^2u/\partial x^2) + (1 - \nu)(\partial^2u/\partial y^2) + (1 + \nu)(\partial^2v/\partial x\partial y)] + 2Gcu + Gc(c + t)(\partial w/\partial x) = 0 \quad (1)$$

$$-B_0[2(\partial^2v/\partial y^2) + (1 - \nu)(\partial^2v/\partial x^2) + (1 + \nu)(\partial^2u/\partial x\partial y)] + 2Gcv + Gc(c + t)(\partial w/\partial y) = 0 \quad (2)$$

$$B_f[(\partial^4w/\partial x^4) + 2(\partial^4w/\partial x^2\partial y^2) + (\partial^4w/\partial y^4)] - [2Gc/(c + t)][(\partial u/\partial x) + (\partial v/\partial y)] - Gc[(\partial^2w/\partial x^2) + (\partial^2w/\partial y^2)] + P_{cr}(\partial^2w/\partial y^2) = 0 \quad (3)$$

where $B_0 = Et(c + t)^2/2(1 - \nu^2)$ and $B_f = Et^3/6(1 - \nu^2)$. Making a transformation of coordinates $\xi = x/a$ and $\eta = y/b$, Eqs. (1), (2), and (3) become

$$-B_0\{(2/a^2)(\partial^2u/\partial\xi^2) + [(1 - \nu)/b^2](\partial^2u/\partial\eta^2) + [(1 + \nu)/ab](\partial^2v/\partial\xi\partial\eta)\} + 2Gcu + Gc(c + t)(\partial w/\partial\xi) = 0 \quad (4)$$

$$-B_0\{(2/b^2)(\partial^2v/\partial\eta^2) + [(1 - \nu)/a^2](\partial^2v/\partial\xi^2) + [(1 + \nu)/ab](\partial^2u/\partial\xi\partial\eta)\} + 2Gcv + Gc(c + t)(\partial w/\partial\eta) = 0 \quad (5)$$

$$B_f[(1/a^4)(\partial^4w/\partial\xi^4) + (2/a^2b^2)(\partial^4w/\partial\xi^2\partial\eta^2) + (1/b^4)(\partial^4w/\partial\eta^4)] - Gc[2/(c + t)][(1/a)(\partial u/\partial\xi) + (1/b)(\partial v/\partial\eta)] - Gc[(1/a^2)(\partial^2w/\partial\xi^2) + (1/b^2)(\partial^2w/\partial\eta^2)] + (P_{cr}/b^2)(\partial^2w/\partial\eta^2) = 0 \quad (6)$$

A solution for the displacements is assumed in the form:

$$u = a_ne^{\alpha_n\eta}\sin(n\pi/2)\xi \quad (7)$$

$$v = b_ne^{\alpha_n\eta}\cos(n\pi/2)\xi \quad (8)$$

$$w = c_ne^{\alpha_n\eta}\cos(n\pi/2)\xi \quad (9)$$

If the foregoing solution is substituted into Eqs. (4), (5) and (6), the equations of equilibrium are transformed into three simultaneous algebraic equations,

$$-A_1[-2(n\pi/2)^2a_n + (k\alpha_n)^2(1 - \nu)a_n - (k\alpha_n)(1 + \nu)(n\pi/2)b_n] + a_n - A_2(n\pi/2)c_n = 0 \quad (10)$$

$$-A_1[2(k\alpha_n)^2b_n - (n\pi/2)^2(1 - \nu)b_n + (k\alpha_n)(1 + \nu)(n\pi/2)a_n] + b_n + A_2(k\alpha_n)c_n = 0 \quad (11)$$

$$A_3[(n\pi/2)^2 - (k\alpha_n)^2]^2c_n - (1/A_2)[(n\pi/2)a_n + (k\alpha_n)b_n] + [(n\pi/2)^2 - (k\alpha_n)^2]c_n + \lambda(k\alpha_n)^2c_n = 0 \quad (12)$$

where

$$A_1 = 3[(c/t) + 1]^2/R(c/t), \qquad \lambda = P_{cr}/Gc$$
$$A_2 = (t/2a)/[(c/t) + 1], \qquad R = 12(1 - \nu^2)Ga^2/Et^2$$
$$A_3 = 2/R(c/t), \qquad k = a/b$$

The above equations represent three linear homogeneous equations whose denominator determinant, formed by the coefficients of the a_n, b_n, and c_n terms, must vanish. Enforcement of this condition leads to the following quartic algebraic equation:

$$[f_n + 1/A_1(1 - \nu)]\{-2A_1A_3f_n^3 - [2A_1(1 - \lambda) + A_3]f_n^2 - \lambda[2A_1(n\pi/2)^2 - 1]f_n - \lambda(n\pi/2)^2\} = 0 \quad (13)$$

where

$$f_n = (n\pi/2)^2 - (k\alpha_n)^2 \quad (13a)$$

One of the roots of the above equation is immediately obtained,

$$f_{1n} = -1/A_1(1 - \nu)$$

Note that this root is dependent only on the physical and geometrical properties of the sandwich plate. The remaining three roots, f_{2n}, f_{3n}, and f_{4n}, are obtained by solving the cubic expression in the brackets in Eq. (13). Once the four roots of Eq. (13) are determined, the eight corresponding values of α follow from the substitution previously made [Eq. (13a)].

The eight roots in α are in the form $\pm\alpha_{1n}$, $\pm\alpha_{2n}$, $\pm\alpha_{3n}$, and $\pm\alpha_{4n}$. If we substitute these values into the displacement functions and stipulate that the displacements in the loaded direction be symmetrical, the expressions for u, v, and w can be written as follows:

$$u = [C_{1n}a_{1n} \cosh \alpha_{1n}\eta + C_{2n}a_{2n} \cosh \alpha_{2n}\eta + C_{3n}a_{3n} \cosh \alpha_{3n}\eta + C_{4n}a_{4n} \cosh \alpha_{4n}\eta] \sin (n\pi/2)\xi \quad (14)$$

$$v = [C_{1n}b_{1n} \sinh \alpha_{1n}\eta + C_{2n}b_{2n} \sinh \alpha_{2n}\eta + C_{3n}b_{3n} \sinh \alpha_{3n}\eta + C_{4n}b_{4n} \sinh \alpha_{4n}\eta] \cos (n\pi/2)\xi \quad (15)$$

$$w = [C_{1n} \cosh \alpha_{1n}\eta + C_{2n} \cosh \alpha_{2n}\eta + C_{3n} \cosh \alpha_{3n}\eta + C_{4n} \cosh \alpha_{4n}\eta] \cos (n\pi/2)\xi \quad (16)$$

In writing down the foregoing displacement functions, Eqs. (7), (8), and (9) were redefined by arbitrarily assigning a value of unity to c_n.

Thus, the a_n's and b_n's in Eqs. (14) and (15) correspond to $c_n = 1$ in Eqs. (7), (8), and (9). By substituting the above displacement functions into the equations of equilibrium, it can be shown that

$$a_n = A_2(n\pi/2)/2A_1f_n + 1 \quad (17)$$

$$b_n = -A_2(k\alpha_n)/2A_1f_n + 1 \quad (18)$$

Boundary Conditions

For the present problem, the sandwich plate is loaded edgewise in one direction and has clamped loaded edges and unloaded edges that are simply supported. The following boundary conditions are required to be satisfied:

$$w = 0 \quad (\text{at } \xi = \pm 1) \quad (19)$$

$$w = 0 \quad (\text{at } \eta = \pm 1) \quad (20)$$

$$\partial w/\partial \eta = 0 \quad (\text{at } \eta = \pm 1) \quad (21)$$

$$\partial^2 w/\partial \xi^2 = 0 \quad (\text{at } \xi = \pm 1) \quad (22)$$

$$u = 0 \quad (\text{at } \eta = \pm 1) \quad (23)$$

$$v = 0 \quad (\text{at } \eta = \pm 1) \quad (24)$$

$$v = 0 \quad (\text{at } \xi = \pm 1) \quad (25)$$

$$\partial u/\partial \xi + \nu(\partial v/\partial \eta) = 0 \quad (\text{at } \xi = \pm 1) \quad (26)$$

Boundary conditions (19), (22), (25), and (26) at the unloaded edges ($\xi = \pm 1$) are satisfied identically by the trigonometric functions. Enforcement of the remaining four boundary conditions yield the following equations:

$$C_{1n} \cosh \alpha_{1n} + C_{2n} \cosh \alpha_{2n} + C_{3n} \cosh \alpha_{3n} + C_{4n} \cosh \alpha_{4n} = 0 \quad (27)$$

$$C_{1n}\alpha_{1n} \sinh \alpha_{1n} + C_{2n}\alpha_{2n} \sinh \alpha_{2n} + C_{3n}\alpha_{3n} \sinh \alpha_{3n} + C_{4n}\alpha_{4n} \sinh \alpha_{4n} = 0 \quad (28)$$

$$C_{1n}a_{1n} \cosh \alpha_{1n} + C_{2n}a_{2n} \cosh \alpha_{2n} + C_{3n}a_{3n} \cosh \alpha_{3n} + C_{4n}a_{4n} \cosh \alpha_{4n} = 0 \quad (29)$$

$$C_{1n}b_{1n} \sinh \alpha_{1n} + C_{2n}b_{2n} \sinh \alpha_{2n} + C_{3n}b_{3n} \sinh \alpha_{3n} + C_{4n}b_{4n} \sinh \alpha_{4n} = 0 \quad (30)$$

The boundary conditions therefore yield the foregoing four linear simultaneous homogeneous equations in four unknown arbitrary constants. The only possibility for a nontrivial solution occurs if the denominator determinant, formed by the coefficient of the C's, is equal to zero.

$$\begin{vmatrix} \cosh \alpha_{1n} & \cosh \alpha_{2n} & \cosh \alpha_{3n} & \cosh \alpha_{4n} \\ \alpha_{1n} \sinh \alpha_{1n} & \alpha_{2n} \sinh \alpha_{2n} & \alpha_{3n} \sinh \alpha_{3n} & \alpha_{4n} \sinh \alpha_{4n} \\ a_{1n} \cosh \alpha_{1n} & a_{2n} \cosh \alpha_{2n} & a_{3n} \cosh \alpha_{3n} & a_{4n} \cosh \alpha_{4n} \\ b_{1n} \sinh \alpha_{1n} & b_{2n} \sinh \alpha_{2n} & b_{3n} \sinh \alpha_{3n} & b_{4n} \sinh \alpha_{4n} \end{vmatrix} = 0 \quad (31)$$

By a manipulation of the elements of the above determinant, it may be reduced from one of the fourth order to one of the third order.

$$Q_n \begin{vmatrix} \alpha_{2n} \tanh \alpha_{2n} - \alpha_{1n} \tanh \alpha_{1n} & a_{2n} - a_{1n} & b_{2n} \tanh \alpha_{2n} - b_{1n} \tanh \alpha_{1n} \\ \alpha_{3n} \tanh \alpha_{3n} - \alpha_{1n} \tanh \alpha_{1n} & a_{3n} - a_{1n} & b_{3n} \tanh \alpha_{3n} - b_{1n} \tanh \alpha_{1n} \\ \alpha_{4n} \tanh \alpha_{4n} - \alpha_{1n} \tanh \alpha_{1n} & a_{4n} - a_{1n} & b_{4n} \tanh \alpha_{4n} - b_{1n} \tanh \alpha_{1n} \end{vmatrix} = 0 \quad (32)$$

where

$$Q_n = \cosh \alpha_{1n} \cosh \alpha_{2n} \cosh \alpha_{3n} \cosh \alpha_{4n} \tag{32a}$$

It will be recalled that the quantities forming the elements of the above determinant come from the solution of the quartic equation, Eq. (13), and that three of the four roots are dependent upon the critical load. The procedure for obtaining the numerical value of the critical load involves assuming a value for the critical load, and, if the value happens to be correct, determinants (31) or (32) will be satisfied. In general, the assumed critical value is not the correct one—i.e., the determinant yields a value other than zero. If three or four values of the critical load are assumed and the corresponding values of the determinant are plotted against the critical load, then the value of the critical load may easily be obtained by graphical interpolation.

In the foregoing analysis, it is assumed that the plate buckles symmetrically in the loaded (η) direction. There will be certain values of the plate aspect ratio (ratio of height to width), for which the sandwich plate buckles unsymmetrically. In these cases, the expressions for u, v, and w will take the following form.

$$u = [C_{1n}a_{1n} \sinh \alpha_{1n}\eta + C_{2n}a_{2n} \sinh \alpha_{2n}\eta + C_{3n}a_{3n} \sinh \alpha_{3n}\eta + C_{4n}a_{4n} \sinh \alpha_{4n}\eta] \sin (n\pi/2)\xi \tag{33}$$

$$v = [C_{1n}b_{1n} \cosh \alpha_{1n}\eta + C_{2n}b_{2n} \cosh \alpha_{2n}\eta + C_{3n}b_{3n} \cosh \alpha_{3n}\eta + C_{4n}b_{4n} \cosh \alpha_{4n}\eta] \cos (n\pi/2)\xi \tag{34}$$

$$w = [C_{1n} \sinh \alpha_{1n}\eta + C_{2n} \sinh \alpha_{2n}\eta + C_{3n} \sinh \alpha_{3n}\eta + C_{4n} \sinh \alpha_{4n}\eta] \cos (n\pi/2)\xi \tag{35}$$

The boundary conditions remain unchanged, and their enforcement leads to four simultaneous homogeneous equations as it does in the symmetrical case. Following the same line of reasoning as before, the determinant corresponding to Eq. (32) giving the critical load is obtained.

$$S_n \begin{vmatrix} \alpha_{2n}/\tanh \alpha_{2n} - \alpha_{1n}/\tanh \alpha_{1n} & a_{2n} - a_{1n} & b_{2n}/\tanh \alpha_{2n} - b_{1n}/\tanh \alpha_{1n} \\ \alpha_{3n}/\tanh \alpha_{3n} - \alpha_{1n}/\tanh \alpha_{1n} & a_{3n} - a_{1n} & b_{3n}/\tanh \alpha_{3n} - b_{1n}/\tanh \alpha_{1n} \\ \alpha_{4n}/\tanh \alpha_{4n} - \alpha_{1n}/\tanh \alpha_{1n} & a_{4n} - a_{1n} & b_{4n}/\tanh \alpha_{4n} - b_{1n}/\tanh \alpha_{1n} \end{vmatrix} = 0 \tag{36}$$

where $S_n = \sinh \alpha_{1n} \sinh \alpha_{2n} \sinh \alpha_{3n} \sinh \alpha_{4n}$.

For the case in which the loaded edges are simply supported and the unloaded edges clamped, an exact solution may also be obtained. The procedure is similar to that described above and only the more important differences will be discussed. It can be assumed that the rectangular sandwich plate maintains its original orientation with respect to the coordinate system. The edge load, however, is made to act in the x or ξ direction—i.e., on the simply supported edges.

Under these conditions, the three equations of equilibriums, Eqs. (4), (5), and (6), remain unaltered except that the last term in Eq. (6) is replaced by $(P_{cr}/b^2)\,(\partial^2 w/\partial \xi^2)$. The displacement functions assumed in the loaded edges fixed case [Eqs. (7), (8), and (9)] are again assumed as solutions. By following the procedure previously described, the quartic equation corresponding to that given in Eq. (13) is obtained.

$$[f_n + 1/A_1(1 - \nu)] \left\{-2A_1B_1{f_n}^3 - (2A_1 + B_1){f_n}^2 + [2A_1(n\pi/2)^2\lambda]f_n + \lambda(n\pi/2)^2\right\} = 0 \tag{37}$$

From this point, the analysis is identical to that presented for the loaded edges fixed case. Even the boundary conditions need no alteration because the sandwich plate was allowed to maintain its original relationship with the coordinate system. Hence, the determinants required to vanish are given by Eqs. (32) and (36). In reference 11, a solution is given for this problem. Lower bounds are obtained by Leggett's method; upperbounds, by Galerkin's method.

Numerical Results

Values of the buckling load, calculated according to the present exact theory, are presented in Figs. 2 through 5. In Figs. 2 and 3, a buckling coefficient, C, is plotted as a function of the sandwich plate height to width ratio (aspect ratio). Each curve is valid for a particular value of the parameter R (relative rigidity in shear to that in bending) and a particular value of core to face thickness ratio.

The buckling coefficient, C, is defined by

$$C = \sigma_{cr}/F\sigma_{cr_0}$$

Physically, C is the ratio of the actual critical stress of the panel to the critical stress of a sandwich plate whose edges are simply supported, its core being infinitely strong in shear and without bending resistance. For values of the aspect ratio approaching infinity, C approaches 1, provided R is relatively high.

Fig. 2 shows the relationship between C and the aspect ratio for values of R equal to 50,000 and 25,000. The values chosen for c/t, the core to face thickness ratio, are 15 and 25. Differences in C due to the change in c/t were so small that a single curve is shown for each value of the relative rigidity R.

The results of March and Smith (strain energy solution) are also presented for comparison. In converting to C the values of the critical load coefficient, k_{cr}, used by March and Smith in reference 3, the relationship

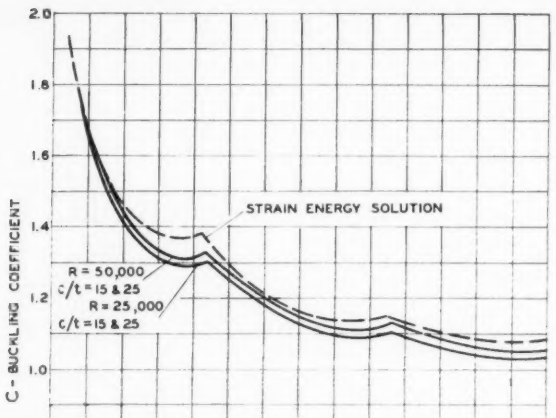

FIG. 2. Buckling coefficient vs. aspect ratio for various values of the relative rigidity.

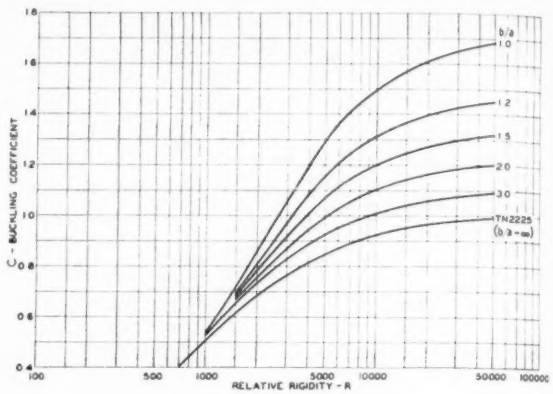

FIG. 4. Buckling coefficient variation with relative rigidity for selected aspect ratios $c/t = 15$.

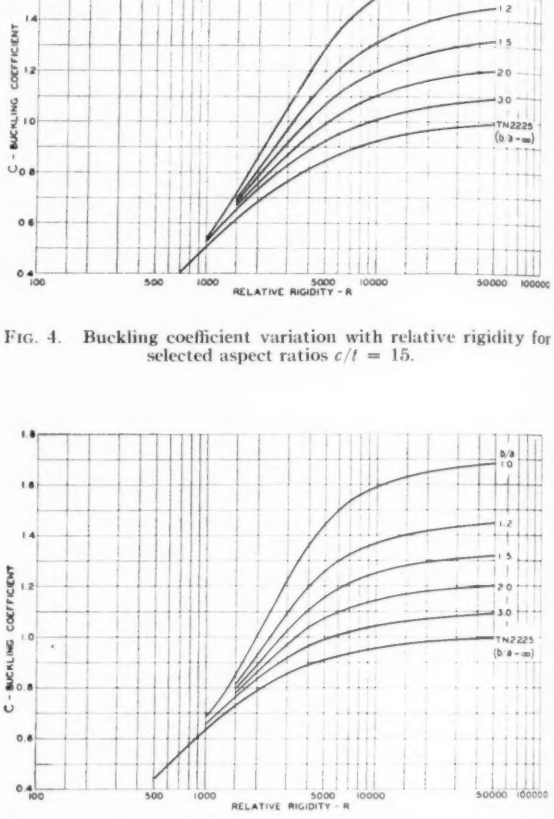

FIG. 5. Buckling coefficient variation with relative rigidity for selected aspect ratios $c/t = 25$.

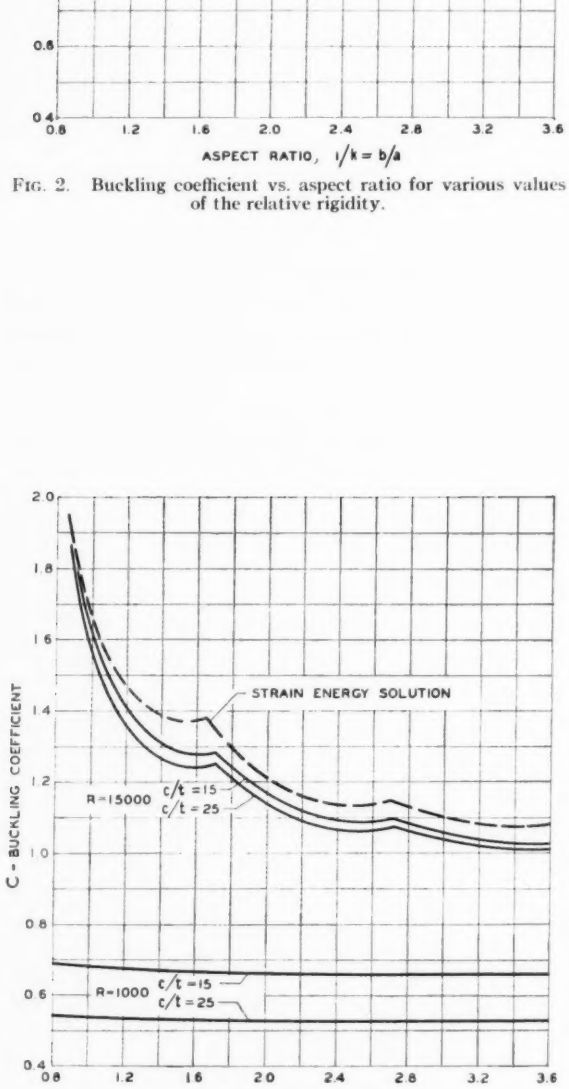

FIG. 3. Buckling coefficient vs. aspect ratio for various values of the relative rigidity.

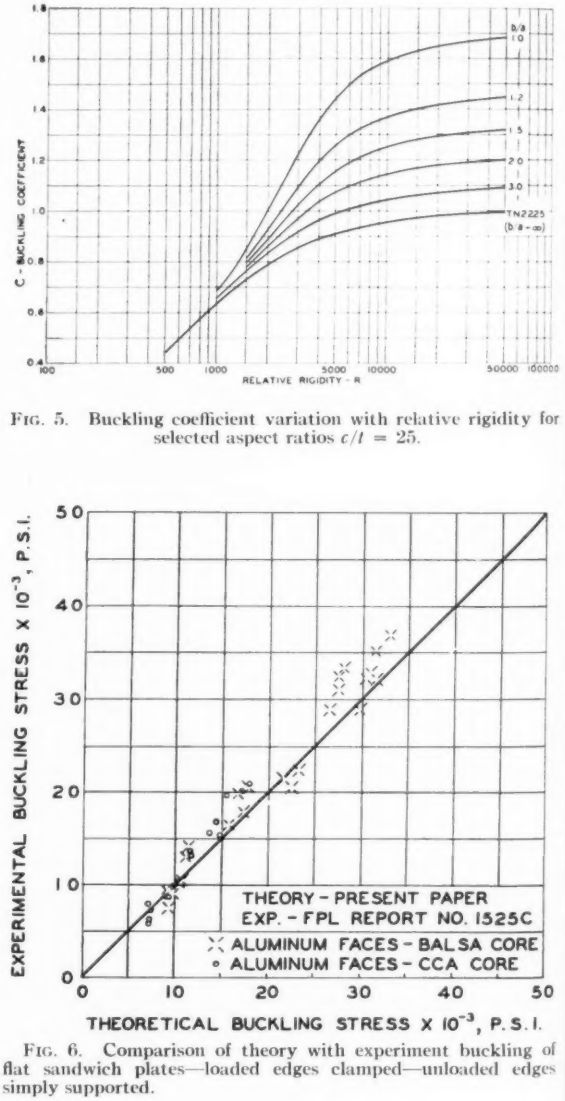
EXPERIMENTAL BUCKLING STRESS X 10⁻³, P.S.I.
THEORETICAL BUCKLING STRESS X 10⁻³, P.S.I.
THEORY - PRESENT PAPER
EXP. - FPL REPORT NO. 1525C
ALUMINUM FACES - BALSA CORE
ALUMINUM FACES - CCA CORE

FIG. 6. Comparison of theory with experiment buckling of flat sandwich plates—loaded edges clamped—unloaded edges simply supported.

$$C = (3/\pi^2)k_{cr}$$

was employed. In deriving the above expression, D, the plate bending rigidity, was assumed equal to $E(h^3 - c^3)/12(1 - \nu^2)$, which means that the contribution of the core to the plate bending rigidity was neglected.

In Fig. 3, curves of the same type are presented for values of R equal to 15,000 and 1,000. For each value of R, curves are presented corresponding to c/t ratios of 15 and 25. As R decreases, the effect of the shearing deformations becomes noticeable. Note the changes that take place in the buckling coefficient at values of R between 15,000 and 1,000. At R equal to 1,000, the results are almost independent of the sandwich plate aspect ratio, and smooth curves are drawn rather than the "scalloped" characteristic curves corresponding to larger values of R.

To extend the usefulness of the curves, the numerical results of Figs. 2 and 3 were cross-plotted to yield curves of the buckling coefficient C versus the sandwich plate relative rigidity R for selected aspect ratios and a fixed core to thickness ratio. These results are presented in Figs. 4 and 5. Also shown in these figures are curves corresponding to infinite aspect ratio (all edges simply supported) obtained by cross-plotting the results presented in reference 7. At values of the aspect ratio of 3.6, it was found that the values of the buckling coefficient were within 6 to 8 per cent of the values given for the simply supported case of reference 7.

Comparison with Experiment

The theory presented in this paper was checked against the results of experiments conducted by the Forest Products Laboratory.[12] The critical stress was computed by the present theory for 42 sandwich plates whose faces were composed of aluminum-alloy sheet and whose cores were of either balsa or cellular cellulose acetate. Only those panels that suffered a glue or compression failure were disregarded. Fig. 6 shows the comparison of the theoretical results with the observed values.

On the whole, it is considered that the theory is in reasonable agreement with the experimental results. Although three panels indicated a difference between theory and experiment of over 20 per cent, three-quarters of the panels agreed within 15 per cent, and one-half of the panels agreed within 10 per cent. Fig. 6 shows a tendency for the theory to be conservative—i.e., theoretical critical stresses lower than those observed experimentally.

A discrepancy of 10 to 15 per cent between theory and experiment is judged to be reasonable on the basis of the many factors that affect the observed critical load. One of these factors is the unavoidable variations in the mechanical properties of the face and core material. In computing the theoretical critical stresses, the modulus value used for the faces was taken from data published by the Aluminum Company of America for 24S-T Alclad aluminum alloy. For sandwich panels buckling at stresses exceeding the elastic limit of the aluminum alloy, the Young's modulus in the equations was replaced by the tangent modulus. The values recommended in reference 12 by the Forest Products Laboratory were taken as the shear moduli of the core materials.

There are factors that would tend to make the experimental critical loads fall below theory. Probably the most important factor is the inability to obtain perfect rigid end fixation in practice. On the other hand, experiment is apt to be higher than theory if the unloaded edges are not perfectly hinged and if the core absorbs part of the edge load (in the theory, only the faces are assumed to absorb the edge load). In addition, there was a $^1/_4$-in. overhang on each side of the simple supports, which also contributed toward increasing the observed critical values over those obtained by the theory.

The scatter of 10 to 15 per cent mentioned should be compared with the scatter in the experimental results. For example, there were three pairs of panels for which all the geometric and physical properties within each pair were identical with the exception of the core thickness. With decreasing core thickness, the critical load would be expected to decrease. In one of the three cases mentioned, the experimental critical load remained constant, and in the other two cases the experimental critical load rose approximately 10 per cent. In the case of one pair of identical panels, there was a 5 per cent difference in the observed critical loads; in a second identical pair, the difference was 30 per cent. It is not the intention of the author to cast aspersions on the experimental results. On the contrary, it is appreciated that reliable plate buckling tests, especially on sandwich plates, are difficult to perform, and it is considered that the experiments of reference 12 were well conducted. The comments in the foregoing paragraphs were solely intended to justify the conclusion that the theory was in reasonable agreement with experiment.

Concluding Remarks

An exact theory has been presented for the buckling loads of flat rectangular sandwich panels with loaded edges clamped, unloaded edges simply supported, and loaded edgewise in one direction. Briefly indicated is the method of solution for the case of a sandwich plate whose loaded edges are simply supported and unloaded edges clamped.

A series of design charts are presented which give the buckling loads of sandwich plates for various relative bending rigidities, aspect ratios, and core to face thicknesses of 15 and 25. It is appreciated that many plates may not fall within the range of parameters covered by the curves. The parameters were chosen

with a view toward encompassing most plates encountered in practice without unduly lengthening the time required to perform the numerical computations. A check of the theory with published test data indicates reasonable agreement between theory and experiment.

References

[1] Leggett, D. M. A., and Hopkins, H. G., *Sandwich Panels and Cylinders under Compressive End Loads*, R. & M. No. 2262, British A.R.C., 1942.

[2] Van der Neut, A., *Die Stabilitaet Geschichteter Platten*, Rapport S.286, Nationaal Luchtvaartlaboratorium, September, 1943.

[3] March, H. W., and Smith, C. B., *Buckling Loads of Flat Sandwich Panels in Compression. Various Types of Edge Conditions*, Forest Products Laboratory Report No. 1525, March, 1945.

[4] *Bijlaard, P. P., On the Elastic Stability of Thin Plates Supported by a Continuous Medium*, Proc. Roy. Netherlands Acad. Sci., No. 10, 1946. *On the Elastic Stability of Sandwich Plates, I*, Proc. Roy. Netherlands Acad. Sci., No. 1, 1947. *On the Elastic Stability of Sandwich Plates, II*, Proc. Roy. Netherlands Acad. Sci., No. 2, 1947.

[5] Reissner, Eric, *Finite Deflections of Sandwich Plates*, Journal of the Aeronautical Sciences, Vol. 15, No. 7, pp. 435–440, July, 1948.

[6] Libove, Charles, and Batdorf, S. B., *A General Small-Deflection Theory for Flat Sandwich Plates*, NACA TN No. 1526, 1948.

[7] Hoff, N. J., *Bending and Buckling of Rectangular Sandwich Plates*, NACA T.N. No. 2225, November, 1950.

[8] Schleicher, F., *Mitt. Forschungsanstalt Gutehoffnungshütte Konzerns*, Vol. 1; 1931.

[9] Timoshenko, S., *Theory of Elastic Stability*, p. 364; McGraw-Hill Book Company, Inc., New York, 1936.

[10] Smith, R. C. T., *The Buckling of Flat Plywood Plates in Compression*, Australian Council for Aeronautics Report ACA-12, December, 1944.

[11] Yen, Kuo Tai, Salerno, V. L., and Hoff, N. J., *Buckling of Rectangular Sandwich Plates Subjected to Edgewise Compression with Loaded Edges Simply Supported and Unloaded Edges Clamped*, NACA TN No. 2556, January, 1952.

[12] Boller, K. H., *Buckling Loads of Flat Sandwich Panels in Compression—Loaded Edges Clamped and the Remaining Edges Simply Supported*, Forest Products Laboratory Report No. 1525C, September, 1947.

Aerodynamic Interference Between Moving Blade Rows

(*Concluded from page 597*)

[7] Whittaker, E. T., and Watson, G. N., *Modern Analysis*, American Ed., p. 136, Example 7; The Macmillan Company, New York, 1948.

[8] Glauert, H., *The Elements of Aerofoil and Airscrew Theory*, 2nd Ed.; Cambridge University Press, England, 1948.

[9] Watson, G. N., *Theory of Bessel Functions*, 2nd Ed.; The Macmillan Company, New York, 1945.

[10] Jahnke, E., and Emde, F., *Tables of Functions*, p. 149; B. Teubner, Berlin, 1938. (Also Dover Publications, New York, 1943.)

[11] Kemp, Nelson H., *On the Lift and Circulation of Airfoils in Some Unsteady-Flow Problems*, Journal of the Aeronautical Sciences, Vol. 19, No. 10, p. 713, October, 1952.

[12] Lowan, A. N., *Table of the Bessel Functions $J_0(z)$ and $J_1(z)$ for Complex Arguments*, WPA Tables; Columbia University Press, New York, 1943.

[13] Kemp, Nelson H., and Sears, W. R., *Aerodynamic Interference Between Moving Blade Rows*, submitted to Air Force R. & D. Command under contract AF 33 (038)-21406, December 1, 1952.

[14] Luke, Y. L., and Dengler, M. A., *Tables of the Theodorsen Function for Generalized Motion*, Journal of the Aeronautical Sciences, Vol. 18, No. 7, pp. 481–483, July, 1951.

IAS Twenty-Second Annual Meeting

Authors wishing to have papers considered for presentation at this meeting should submit outlines or short abstracts to the Meetings Committee, 2 East 64th St., New York 21, N.Y., no later than September 15, 1953.

Thermal Stresses in Conical Shells

J. H. HUTH*
The RAND Corporation

SUMMARY

This paper considers the stresses in a conical shell of revolution resulting from aerodynamic pressure and thermal gradients. In particular, the results are applicable to the conical tip of a missile flying at zero angle of attack; a numerical example is given for a temperature distribution typical of a laminar boundary layer. It is concluded that from the standpoint of eliminating high stresses, large temperature gradients both along a ray and across the shell thickness are most undesirable.

NOMENCLATURE

A_{1-4}	= constants of integration
D	= $Eh^3/12(1-\nu^2)$
E	= modulus of elasticity
ν	= Poisson's ratio
h	= shell thickness
λ	= $\sqrt[4]{(Eh/D)\operatorname{ctn}^2\alpha}$
α	= cone half-angle
p	= aerodynamic pressure
M_l, M_θ	= bending moments per unit length of shell section
N_l, N_θ	= membrane forces per unit length of shell section
ρ	= density of shell material
ω	= angular velocity of shell
l	= distance along cone element measured from vertex
Q	= shear per unit length of shell section
V, W	= components of displacement in the direction of increasing l and the inward normal to l, respectively
ξ	= outward radial displacement
ζ	= axial displacement
α_t	= thermal coefficient of expansion
T	= temperature
a-c	= temperature levels
(ΔT)	= mean shell temperature (at any point l), above a reference temperature T_0
(δT)	= temperature differential across the shell at any point (assumed linear)
s, ψ	= dummy variables
i	= $\sqrt{-1}$
L	= an operator defined by: $\left(l\frac{d^2}{dl^2}+\frac{d}{dl}-\frac{1}{l}\right)x = L(\psi)$
n	= $2\lambda\sqrt{il}$
m	= in
X	= $2\lambda\sqrt{l}$
J_2, Y_2	= Bessel functions of the first and second kind and of the second order
$Z_1(x)$	= $\operatorname{ber}(x)$; $Z_2(x) = -\operatorname{bei}(x)$; $Z_3 = -(2/\pi)\operatorname{kei}(x)$; $Z_4(x) = -(2/\pi)\operatorname{ker}(x)$, where the ber, bei, ker, and kei functions are Thompson's functions. $Z'(x)$ refers to the derivative of the function with respect to x

Received November 24, 1952.
* Missiles Division.

INTRODUCTION

AERODYNAMIC HEATING along the forward portion of a high-speed missile often results in large temperature gradients. In many cases such temperature variations may have a pronounced effect on the structural design of a missile.

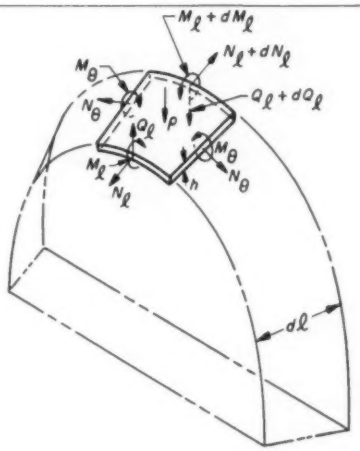

Fig. 1 — Forces and bending moments acting on an element of a conical shell of revolution

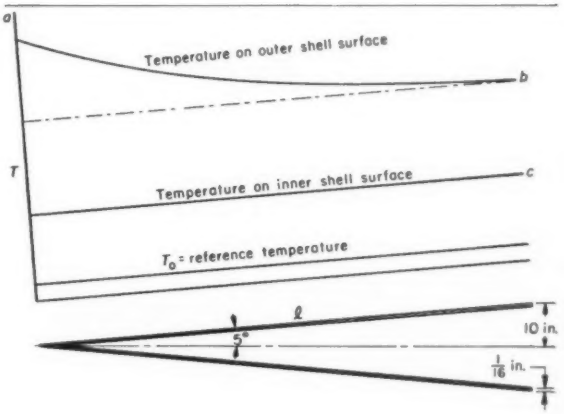

Fig. 2 — Temperature variations along the inner and outer shell surfaces

The case of thermal stresses in cylindrical shells has been treated by Timoshenko and others,[1, 2] while the present paper considers conical shells. In particular, the analysis will consider conditions in the conical nose of a supersonic missile at zero angle of attack. A further application can be made to aircraft gas-turbine tailpipes.

Analysis

In reference 3, Meriam has restated the general equations from the bending theory of shells specialized to rotating bodies of revolution. With the inclusion of appropriate temperature and aerodynamic pressure terms they appear as follows (refer to the Nomenclature and Fig. 1):

$$(d/dl)(N_l l) - N_\theta + \rho\omega^2 l^2 \sin^2\alpha = 0 \tag{1}$$

$$(d/dl)(Q_l l) + N_\theta \operatorname{ctn}\alpha - \rho\omega^2 l^2 \sin\alpha\cos\alpha + pl = 0 \tag{2}$$

$$(d/dl)(M_l l) - Q_l l - M_\theta = 0 \tag{3}$$

$$N_l = \frac{Eh}{(1-\nu^2)}\left[\frac{dV}{dl} + \frac{\nu}{l}(V - W\operatorname{ctn}\alpha) - (1+\nu)\alpha_t \Delta T\right] \tag{4}$$

$$N_\theta = \frac{Eh}{(1-\nu^2)}\left[\nu\frac{dV}{dl} + \frac{1}{l}(V - W\operatorname{ctn}\alpha) - (1+\nu)\alpha_t \Delta T\right] \tag{5}$$

$$M_l = -D\left[\frac{d^2W}{dl^2} + \frac{\nu}{l}\frac{dW}{dl} + (1+\nu)\frac{\alpha_t(\delta T)}{h}\right] \tag{6}$$

$$M_\theta = -D\left[\nu\frac{d^2W}{dl^2} + \frac{1}{l}\frac{dW}{dl} + (1+\nu)\frac{\alpha_t(\delta T)}{h}\right] \tag{7}$$

Here it is assumed that temperature and pressure depend only on l. This would be the case for a missile at zero angle of attack.

These equations may be handled in the standard manner developed by Meissner[4] and illustrated by Meriam.[3] In particular they lead to the following fourth-order differential equation for $(Q_l l)$:

$$l^2\frac{d^4(Q_l l)}{dl^4} + 4l\frac{d^3(Q_l l)}{dl^3} + \lambda^4(Q_l l) = -\frac{E(1+\nu)\alpha_t l}{\tan^2\alpha}\frac{d(\delta T)}{dl} + \frac{Eh\alpha_t}{\tan\alpha}\left[3l\frac{d^2\Delta T}{dl^2} + l^2\frac{d^3\Delta T}{dl^3}\right] + 3\rho\omega^2(3+\nu)\sin\alpha\cos\alpha = H(l) \tag{8}$$

Designating the particular integral of Eq. (8) by $(Q_l l)_p$, the complete solutions in terms of five constants of integration may be expressed as follows:

$$(Q_l l) = A_1\left(Z_1 + \frac{2}{x}Z_2'\right) + A_2\left(Z_2 - \frac{2}{x}Z_1'\right) + A_3\left(Z_3 + \frac{2}{x}Z_4'\right) + A_4\left(Z_4 - \frac{2}{x}Z_3'\right) + (Q_l l)_p \tag{9}$$

$$(N_l l) = A_5\tan\alpha - (Q_l l)\tan\alpha - (pl^2/2)\tan\alpha \tag{10}$$

$$N_\theta = \rho\omega^2 l^2\sin^2\alpha - \frac{pl^2}{2}\tan\alpha - \tan\alpha\frac{d}{dl}(Q_l l)_p - \tan\alpha\left[A_1\left(Z_1' - \frac{2}{X}Z_1 - \frac{4}{X^2}Z_2'\right) + A_2\left(Z_2' - \frac{2}{X}Z_2 + \frac{4}{X^2}Z_1'\right) + A_3\left(Z_3' - \frac{2}{X}Z_3 - \frac{4}{X^2}Z_4'\right) + A_4\left(Z_4' - \frac{2}{X}Z_4 + \frac{4}{X^2}Z_3'\right)\right]\frac{2\lambda^2}{X} \tag{11}$$

$$M_l = -D(1+\nu)\frac{\alpha_t(\delta T)}{h} + (2+\nu)l\tan\alpha\left[\frac{\rho\omega^2 D}{Eh}(3+\nu)\sin^2\alpha\right] + D(1-\nu)\frac{A_5\tan^2\alpha}{l^2 Eh} + D(1+\nu)\alpha_t\tan\alpha\frac{d(\Delta T)}{dl} + D\alpha_t l\tan\alpha\frac{d^2(\Delta T)}{dl^2} - D\frac{\tan\alpha}{Eh}\left\{\frac{d}{dl}[L(Q_l l)_p] + \frac{\nu}{l}L(Q_l l)_p\right\} - \frac{3D}{2Eh}(1+\nu)p\tan\alpha - \frac{2}{X}\left\{A_1\left[Z_2' - \frac{2(1-\nu)}{X}Z_2 + \frac{4(1-\nu)}{X^2}Z_1'\right] + A_2\left[-Z_1' + \frac{2(1-\nu)}{X}Z_1 + \frac{4(1-\nu)}{X^2}Z_2'\right]\right\} - \frac{2}{X}\left\{A_3\left[Z_4' - \frac{2(1-\nu)}{X}Z_4 + \frac{4(1-\nu)}{X^2}Z_3'\right] + A_4\left[-Z_3' + \frac{2(1-\nu)}{X}Z_3 + \frac{4(1-\nu)}{X^2}Z_4\right]\right\} \tag{12}$$

$$M_\theta = (d/dl)(M_l l) - (Q_l l) \tag{13}$$

$$dW/dl = [l/D(1 - \nu^2)](\nu M_l - M_\theta) - (l/h)\alpha_t(\delta T) \tag{14}$$

$$W = (l/Eh)\tan\alpha(\nu N_l - N_\theta) + V\tan\alpha - \alpha_t l\Delta T\tan\alpha \tag{15}$$

$$\zeta = V\sin\alpha - W\cos\alpha \tag{16}$$

$$\xi = V\cos\alpha + W\sin\alpha \tag{17}$$

$$\zeta = \alpha_t l\Delta T\sin\alpha + (l\sin\alpha/Eh)(N_\theta - \nu N_l) \tag{18}$$

In the general case of a truncated cone the five constants of integration could be evaluated by specifying either M_l and Q_l at both ends and N_l at one end, or appropriate combinations of stresses and displacements. However, in the following, the discussion will be limited to a complete cone. In this case A_3, A_4, and A_5 are all zero.

If ΔT and δT can be sufficiently well represented by a polynomial of only a few terms then clearly a series expansion for $(Q_l l)_p$ can be easily obtained from Eq. (8). In the case of transition to a turbulent boundary layer, the temperature variations may be too rapid to permit such a direct approach. However, as pointed out by Meriam, Eq. (8) may be factored into the two Bessel equations,

$$n^2\left(\frac{d^2\psi}{dn^2}\right) + n\left(\frac{d\psi}{dn}\right) + (n^2 - 4)\psi = \frac{n^2}{i\lambda^2}H(l) = H_1(l) \tag{19}$$

$$m^2\frac{d^2(Q_l l)}{dm^2} + m\frac{d(Q_l l)}{dm} + (m^2 - 4)(Q_l l) = \frac{-m^2}{i\lambda^2}\psi_p(m) \tag{20}$$

The particular integrals of these second-order equations are given by Kamke[5] and are of the form,

$$\psi_p = \frac{\pi}{2}Y_2(n)\int_0^n \frac{1}{s}J_2(s)H_1(s)\,ds - \frac{\pi}{2}J_2(n)\int_0^n \frac{1}{s}Y_2(s)H_1(s)\,ds \tag{21}$$

Consequently, the given temperature distribution may be approximated, for example, by parabolic segments, and the resulting particular integrals may be computed with the aid of Eq. (21).

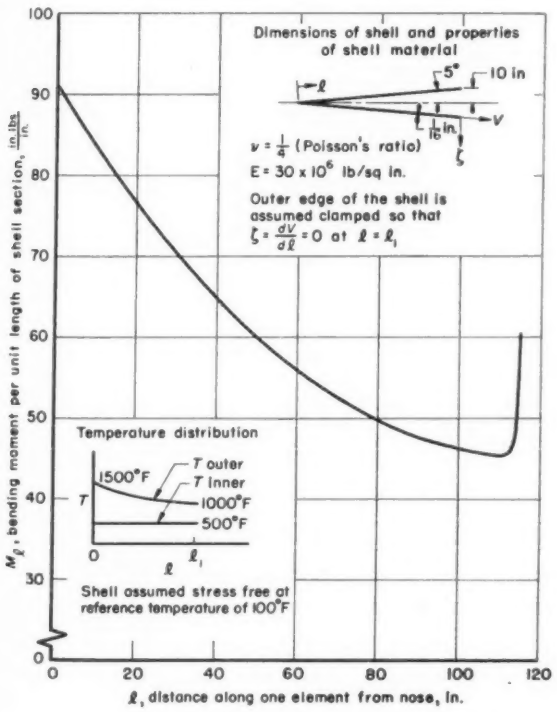

Fig. 3a — Bending moment, M_ℓ, as a function of ℓ in a heated conical shell

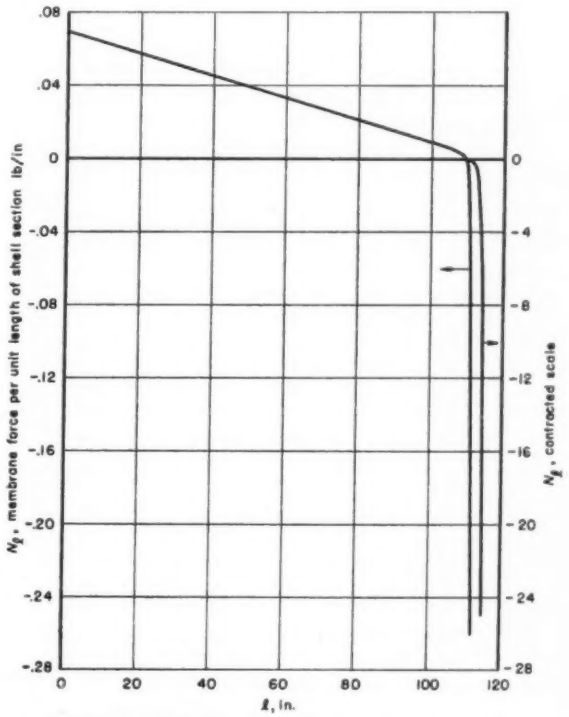

Fig. 3b — Membrane force, N_ℓ, as a function of ℓ in a heated conical shell

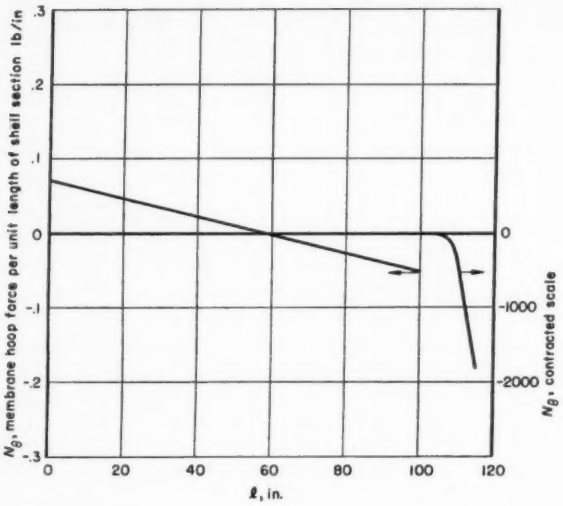

Fig. 3c — Membrane hoop force, N_θ, as a function of ℓ in a heated conical shell

Example

Consider a temperature distribution as shown in Fig. 2. Such a variation might occur in the case of a laminar boundary layer and is given analytically by Eqs. (22).

$$\left.\begin{aligned} \delta T &= C - [b + K(l - l_1)^2] \\ \Delta T &= 1/2[C + b + K(l - l_1)] \\ K &= (a - b)/l_1^2 \end{aligned}\right\} \qquad (22)$$

For this simple case (and for a nonrotating shell in the absence of aerodynamic pressure), the particular integral is given by Eq. (23),

$$(Q_l l)_p = \left[\frac{2KD(1 + \nu)\alpha_t}{h}\right] l^2 + l \times \left[\frac{3KDh\alpha_t \tan \alpha - 2KD(1 + \nu)\alpha_t l_1}{h}\right] \qquad (23)$$

The shell was considered as clamped so that the boundary conditions are as follows:

$$l = l_1, \quad \zeta = 0, \quad dW/dl = 0 \qquad (24)$$

The principal results for a typical choice of a-c are shown in Fig. 3.

Conclusions

The abrupt changes in behavior for $l \cong 110$ apparent in all figures is, of course, the effect of rigid clamping. In an actual missile configuration, rigid clamping certainly will not be achieved, so that the case under consideration represents an extreme. Moreover, the effects of clamping will always be extremely localized. The important thing is the appearance of a high bending moment at the tip of the nose. This bending moment is the result of the thermal gradients and will be affected little by any reasonable variation in clamping conditions at the outer edge. It is apparent that, if high stresses are to be avoided, then large temperature gradients must be eliminated.

The equations provided are sufficiently general to include aerodynamic pressure and rotational effects should this be found desirable in any given application.

References

[1] Timoshenko, S., *Theory of Plates and Shells*, pp. 422–427; McGraw-Hill Book Company, Inc., New York, 1940.

[2] Salzmann, T., *Wärmespannungen und Deformationen im elastischen Körper bei ebener stationärer Wärmestromung*, Zeitschrift für angewandte Mathematik und Physik, Vol. 3, pp. 129–148, March 15, 1952.

[3] Meriam, J. L., *Stresses and Displacements in a Rotating Conical Shell*, Yale University School of Engineering Publication No. 73, November, 1942.

[4] Meissner, E., *Das Elastizitätsprobleme für dünne Schalen von Ringflächen-Kugel- oder Kegelform*, Physikalische Zeitschrift, Vol. 14, pp. 343–349, 1913.

[5] Kamke, E., *Differentialgleichungen Lösungsmethoden und Lösungen*, pp. 437–442; Chelsea Publishing Company, New York, 1948.

Changes of Address

Since the Post Office Department does not as a rule forward magazines to forwarding addresses, it is important that the Institute be notified of changes in address 30 days in advance of publishing date to ensure receipt of every issue of the JOURNAL and REVIEW.

Notices should be printed legibly and sent directly to:

Institute of the Aeronautical Sciences, Inc.

2 East 64th Street, New York 21, New York

Diffusers for Supersonic Wind Tunnels

J. LUKASIEWICZ*

National Aeronautical Establishment, Canada

SUMMARY

A systematic review of published experimental data relating to performance and design of wind-tunnel diffusers for entry Mach Numbers up to 10 is presented. It is found that:

(1) Compressibility effects are negligible in diffusers for $M < 0.9$.

(2) Shock compression is more efficient in constant-area than in divergent ducts and usually requires appreciable duct length for completion.

(3) Pressure recovery of diffusers without contraction is improved by use of a long throat at entry but is always smaller than the theoretical normal shock recovery.

(4) At Mach Numbers below 4, maximum or starting contraction of constant geometry diffusers is closely predicted by simple theory, and better than normal shock pressure recoveries are achieved.

(5) With variable contraction diffusers, pressure recoveries of as much as twice the normal shock recovery are obtainable at hypersonic Mach Numbers. In general, optimum diffuser contraction angles increase with entry Mach Number increasing.

SYMBOLS

D	=	diameter or side of square
$\bar{D}$	=	hydraulic diameter, 4(area/perimeter) = D (for circular or square sections)
L	=	length of shock compression region
M	=	Mach Number
M_F	=	Mach Number based on static pressure and Fanno line of state
P	=	absolute pressure, static
P_0	=	absolute pressure, stagnation (at nozzle or diffuser inlet)
P_0'	=	stagnation pressure at diffuser outlet
Re_D	=	Reynolds Number based on free-stream velocity, density, viscosity, and length D
θ	=	total angle of divergence or contraction (all angles quoted in the text are total angles)
ψ	=	diffuser contraction ratio = (diffuser entry area)/(diffuser throat area)
$\psi_{max.}$	=	maximum theoretical diffuser contraction ratio (for flow starting)

INTRODUCTION

THE SUBJECT OF THIS PAPER was first reviewed by Crocco[1] in 1935. At that time little experimental data existed on supersonic diffusers, and most results quoted by Crocco related to shock compression in divergent ducts, such as Laval nozzles or subsonic diffusers. A second review[2] appeared in 1946; it included newer experimental data and dealt with the theory of supersonic diffusers. Since then scores of supersonic tunnels of various designs were built, and enough experimental data were accumulated to warrant the present attempt at a systematic treatment of supersonic diffuser design and performance. While in no way complete, it indicates the extent of available data and gaps to be filled in.

The subject has been divided up into a number of distinct problems, as follows:

(1) Performance of subsonic diffusers at high subsonic Mach Numbers (i.e., effects of compressibility).

(2) Shock compression in a simple divergent and constant-area duct as a phenomenon common to all supersonic diffusers.

(3) Performance of diffusers without contraction and influence of a long, constant-area section at entry.

(4) Maximum contraction of constant geometry diffusers and their performance.

(5) Contraction and performance of variable geometry diffusers.

Only diffusers used with fully closed wind-tunnel working sections are considered, with no models (unless otherwise stated) mounted in the working section. Insofar as possible, only reliable experimental data are quoted; in fact some well-known results, obtained with wet air or with an ill-defined diffuser setup, were omitted from this review.

In all cases the Reynolds Number of tests is given in terms of free-stream conditions at diffuser entry Mach Number and hydraulic diameter $\bar{D}$ of diffuser entry.

COMPRESSIBILITY EFFECTS IN SUBSONIC DIFFUSERS

Although outside the scope of supersonic diffuser problem, the operation of subsonic diffusers at high subsonic velocities is briefly considered as a particular aspect of compressibility effects in diffusers in general. It is found that the performance of diffusers of small divergence angle ($\leq 7°$ total cone angle) is practically independent of entry Mach Number (provided $M < 0.9$) when expressed as a fraction of theoretical pressure rise. This is shown by experimental results plotted in Fig. 1; about 85 to 90 per cent of theoretical pressure rise is obtained in practice. The former corresponds to a stagnation pressure loss of 3 per cent at $M = 0.6$ and 6 per cent at $M = 0.9$. Since these results were obtained with no model in the tunnel working section and with a particularly good velocity distribution at the diffuser entry, they must be regarded as upper limits of efficiencies attainable in actual subsonic wind-tunnel diffusers.

In some high-speed subsonic tunnels, an adjustable sonic choke or throat is fitted between the working sec-

Received December 11, 1952. Revised and received May 18, 1953.

* Head, High Speed Aerodynamics Laboratory.

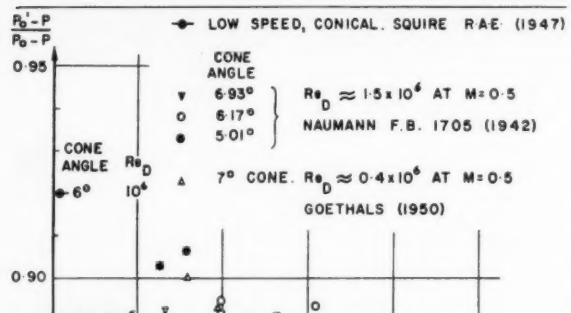

FIG. 1. Pressure rise in subsonic diffusers.

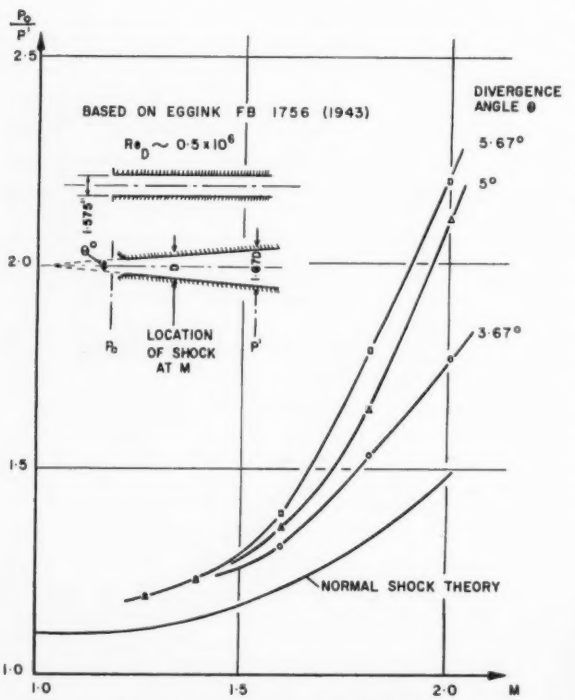

FIG. 2. Effect of duct divergence on shock compression.

tion and the diffuser entry. Its purpose is to provide control over working section Mach Number and/or to prevent disturbances originating in the diffuser or compressor from reaching the model. Following the choke, an expansion to slightly supersonic velocity and shock compression take place in the subsonic diffuser entry. The diffuser data just reviewed are therefore not applicable to subsonic tunnels equipped with a choke which, insofar as diffuser is concerned, are equivalent to supersonic tunnels operating at low Mach Numbers.

Shock Compression in Ducts

Experiment shows that, in general, a continuous deceleration of supersonic flow to subsonic velocity is not possible, the transition always occurring through shock compression. The corresponding simple theoretical model of flow postulates a normal shock but neglects viscous effects. It is not surprising, therefore, that shock compression as observed in ducts, in presence of wall boundary layer, usually differs from the theoretical model. Observations of shock compression in divergent ducts (such as Laval nozzles, downstream of throat) show a gradual rather than sudden increase of pressure at the wall, the static pressure never attaining the values prescribed by simple theory and stagnation pressure losses appreciably exceeding those appropriate to a normal shock. Typical of the latter are results of Castagna's[6] measurements of shock compression in a 6° conical pipe, shown in Fig. 9 in terms of Mach Number based on the lowest observed wall pressure (i.e., at the start of compression) and assumption of isentropic flow. Comparison with the normal shock curve indicates the inadequacy of the normal shock theory. However, the discrepancy is reduced, particularly at higher Mach Numbers, by making the angle of duct divergence smaller, as shown in Fig. 2.

The above overall characteristics of shock compression in divergent ducts are supplemented by schlieren observations, which indicate that, as a result of shock and boundary-layer interaction, the region of shock compression may involve several curved or oblique shocks, forming regular or Mach-type reflections, and, at the walls, extremely thick boundary layers and flow separations. The latter increase both with shock pressure ratio (i.e., flow Mach Number) and with duct divergence, approaching in extreme cases an essentially free-jet configuration, the flow being completely de-

FIG. 3. Detached flow in supersonic nozzle for $M = 4.4$.

tached from the walls following shock compression. An example of this is shown in Fig. 3, which is a schlieren photograph of flow in a 4.4 Mach Number tunnel nozzle operating at a pressure ratio insufficient to induce a fully supersonic flow. Both schlieren and pressure observations suggest that higher efficiencies of shock compression are obtained in small divergence or constant-area ducts. In such ducts there exists in the subsonic flow, downstream of the shock compression region, a positive velocity gradient that tends to stabilize the boundary layer and reduce the separation and resulting losses.

A number of observations of supersonic compression in constant-area ducts, in fact, indicate that this is the case, although the compression does not necessarily resemble a normal shock. Typical schlieren photographs taken in a 1-in. square duct are shown in Fig. 4. The compression consists of several shocks closely following one another, their shape presumably depending on boundary-layer thickness relative to duct diameter (at given Mach and Reynolds Numbers).

A similar flow configuration may be expected to occur in shock-tube flow and is believed to cause the hitherto unexplained appearance† of wave-speed camera photographs, examples of which are shown in Fig. 6.‡ The wave-speed photographs are taken with a schlieren optical system and a drum camera, the flow inside the tube being viewed through narrow and long windows parallel to the tube axis. The photographs can be interpreted with the aid of Fig. 5, in which shock-tube flow is represented diagrammatically in x, t coordinates. The region of tube flow corresponding to the photographs is marked in Fig. 5, and the tube-length (x) and time (t) coordinates are oriented in the same manner in Figs. 5 and 6. Following the bursting of the diaphragm, a shock wave is propagated in the low-pressure chamber of the shock tube and eventually is reflected from the closed tube end, as shown in Fig. 5. On its return travel, the shock enters tube sections in which boundary layer has already developed and presumably causes interaction similar to the stationary shock-boundary-layer system of Fig. 4. The multiple shocks, sketched in Fig. 5, appear as series of oblique ripples in the wave-speed photographs, Fig. 6. It will

† First evident in original photographs obtained by Payman and Shepherd, reference 8, Figs. 3, 4, and 8.

‡ The author is indebted to Dr. I. I. Glass and the Institute of Aerophysics, University of Toronto, for permission to make use of wave-speed photographs originally published in reference 9.

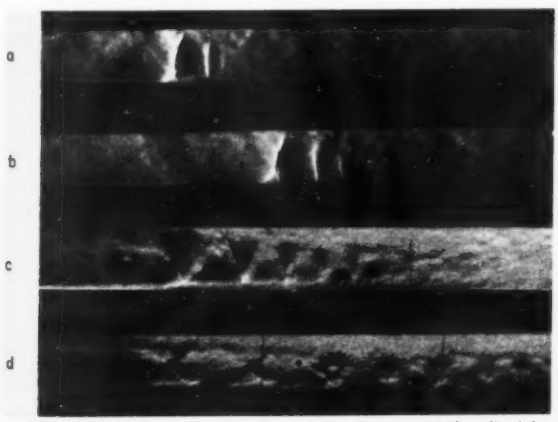

FIG. 4. Schlieren photographs of shock compression in 1-in. square duct ($Re_D \sim 0.2 \times 10^6$) in presence of thick boundary layer. *a*, *b*, *c* — $M \sim 1.5$, shock compression at increasing distances from nozzle. *d* — $M \sim 2.5$.

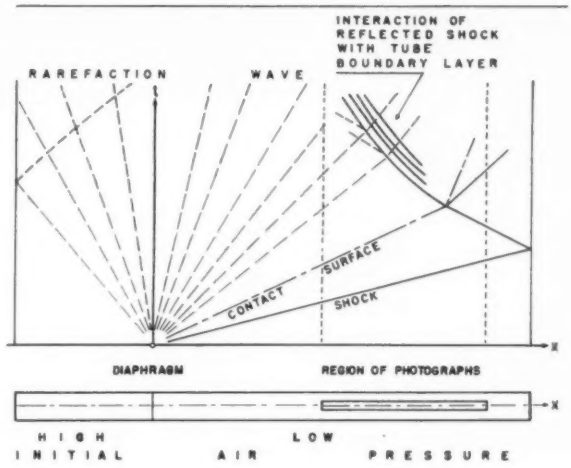

FIG. 5. x-t diagram of shock-tube flow.

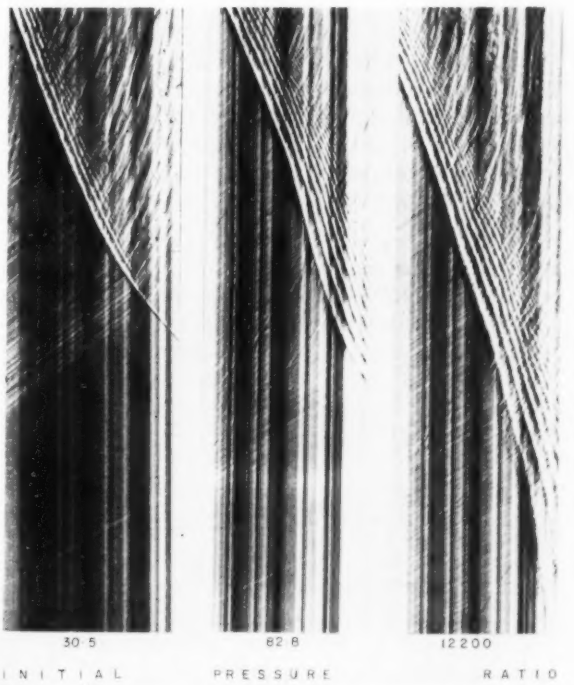

FIG. 6 Wave-speed camera schlieren photographs of shock compression in a shock tube.[9]

TABLE 1

Shock Compression in Tube in Presence of Thick Boundary Layer (Computed from Experimental Data of Reference 12)

1.	Station	Nozzle exit or tube entry	1	2	3	4	5	6	7	8
2.	L/D	0	2	3.75	8	14	21.5	26.4	30.5	40
3.	$(P_1/P_0) \times 10^3$ observed (shockless flow)	2.2	2.5	2.9	3.5	4.4	5.5	6.6	7.5	10.4
4.	M_{Fanno} (based on nominal conditions at tube entry, $M = 5$, $P_1/P_0 = 0.00189$)	5.0	4.28	3.94	3.53	3.08	2.69	2.39	2.19	1.95
5.	M (based on measured P_1/P_0 and isentropic flow)	4.87	4.76	4.64	4.49	4.31	4.14	4.0	3.9	3.67
6.	P_2/P_1 measured	..	19.6	16.6	13.4	10.1	7.6	6.1	5.1	...
7.	$(P_2/P_1)_{M\ \text{Fanno}}$	..	21.2	17.9	14.4	10.9	8.3	6.5	5.4	...
8.	$(P_2/P_1)_M$	..	26.3	24.9	23.3	21.5	19.8	38.8	38.4	...
9.	L/D (length of shock compression)	..	12	12.5	12	11.4	10.8	10	9	...

be noticed that the ripples are approximately parallel, indicating that the whole compression region moves with a substantially constant velocity. The phenomenon appears to gain strength with the initial tube-pressure ratio (given in Fig. 6) or shock intensity and, in fact, is hardly noticeable at extremely low tube-pressure ratios.[9]

So far, only few quantitative results are available on shock compression in constant-area ducts. Most extensive tests were carried out at M.I.T.[12] with relatively thick boundary layers and therefore under conditions not representative of conventional wind-tunnel practice.

The M.I.T. flow setup consisted of a circular supersonic nozzle, followed by a 50-in. long 1-in. diameter tube in which wall-pressure distribution was measured for different back pressures. Typical results obtained in M.I.T. tests are analyzed in Table 1. Because of the low Reynolds Number of tests (about 0.2 million based on tube diameter), appreciable compression occurred in the tube even for shockless flow, the static pressure P_1 (third line, Table 1) increasing about four and one-half times between the nozzle exit (or tube entrance) and station 8, 40 diameters downstream. Since the flow was, to a good approximation, adiabatic, its effective mean parameters could be obtained from pressure distribution and Fanno line of state (derived from equations of conservation of mass, energy, and area). In order to assess the boundary-layer thickness, the "Fanno line" Mach Number M_F is compared in Fig. 7 and Table 1, lines 4 and 5, with Mach Number M derived from static pressure ratio P_1/P_0 on the assumption of isentropic flow. The corresponding boundary-layer thickness can be roughly evaluated from the following consideration: Assuming that boundary layer does not fill completely the tube cross section, the isentropic Mach Numbers M and Mach Number-area ratio relationship can be used to estimate the boundary-layer displacement thickness at any station. Taking a one-seventh power-law velocity distribution in the boundary layer and $\delta^*/\delta \approx 0.4$ at $M = 4$, we find that at station 7 (Table 1) the boundary layer is about 0.44 in. thick, almost filling completely 0.5-in. radius tube.†

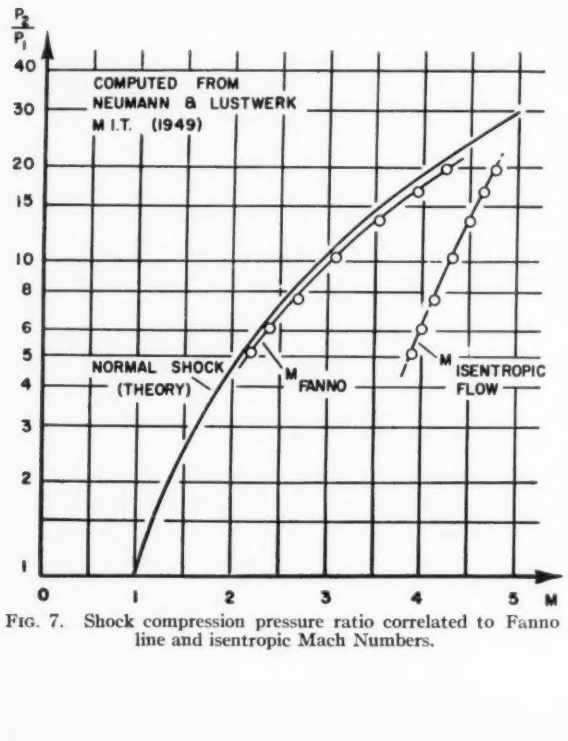

FIG. 7. Shock compression pressure ratio correlated to Fanno line and isentropic Mach Numbers.

With increased tube back pressure, a shock compression develops; pressure ratios P_2/P_1 recorded for compressions that started at stations 1 to 7 are given in Table 1, line 6. Here P_1 is the pressure immediately preceding the compression, and P_2 is the highest pressure attained downstream. As shown in the last line of Table 1, the shock compression region (defined as tube length from P_1 to P_2) is some 10 diameters long, and appears to increase in length with Mach Number.

Observed pressure ratios are compared in Table 1, lines 7 and 8, with the ones corresponding to a normal

† Incidentally, from the observed pressure rise in the tube and M_F it is possible to determine[10] the average friction coefficient $\bar{\lambda}$. For entry $M_F = 5$, the pressure rises (at 30 tube diameters) to three and four-tenths times the value at entry. This corresponds to $\bar{\lambda}L/D \approx 0.07$, whence $\bar{\lambda} \approx 0.0023$. This value agrees with $\bar{\lambda}$ determined at Reynolds Numbers from 0.2×10^5 to 5×10^5 at $L/D \approx 30$ and at inlet Mach Numbers between 2 and 4.[11]

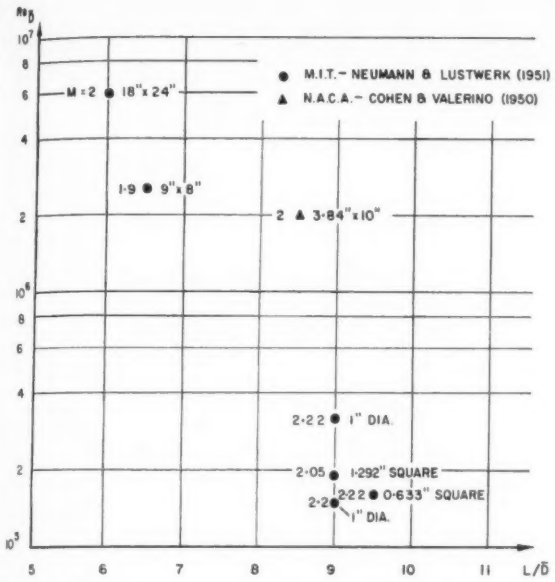

FIG. 8. Effect of Reynolds Number on length of shock compression in constant-area ducts, at $M \sim 2$.

shock at Mach Numbers M_F and M. The agreement is remarkably good with respect to normal shock at M_F (at all tube stations), the discrepancy with $(P_2/P_1)_M$ increasing downstream. This is also shown in Fig. 7.

Although, as seen in schlieren observations of flow, the shock compression in presence of thick boundary layers differs vastly from normal shock configuration, the above agreement in the overall pressure ratio is perhaps not surprising. The theoretical assumptions of normal shock transformation are *a priori* met with respect to conservation of energy (adiabatic flow) and area (constant tube diameter) so that, provided the frictional forces are small in the compression region (as is the case with separated flow), the normal shock solution is strictly applicable at tube sections between which compression takes place, irrespective of the details of shock transformation mechanism. Furthermore, the "Fanno line" Mach Number M_F, representing a mean value that corresponds to the actual energy flux and accounts for the upstream kinetic energy losses in the boundary layer, is the correct one to use in the calculations.

From the above consideration one would expect, in general, a good agreement between measured and predicted (on basis of M_F) shock compression in constant-area ducts, both with thick ($M_F \ll M$) and thin ($M_F \sim M$) boundary layers. However, in the latter case experimental data are scarce. Most published data, here reviewed in the next section, refer to diffusers that include a divergent subsonic portion, so that pressure ratios measured across them are subject to additional subsonic diffuser losses, in turn influenced by the velocity distribution following shock compression in constant-area entry.

On the other hand, more data, if less conclusive, are available on length of shock compression region. It was obtained directly from the above tube experiments (Table 1, bottom line), as well as indirectly from tunnel diffuser tests, in which the length of constant-area diffuser entry was determined to give maximum pressure recovery.

On the basis of tube experiments, a specific variation of shock compression length with Mach Number (M_F) was suggested,[12] whereas compilation of results obtained at Mach Numbers close to 2 was to determine the variation of compression length with Reynolds Number.[13] This is seen in Fig. 8, which indicates, as expected, smaller compression length $L/\bar{D}$ at higher Reynolds Numbers. However, small $L/\bar{D}$ results need further corroboration since they were obtained with M.I.T. tunnels, which show higher pressure recoveries than other tunnels of similar geometry (cf. Fig. 10).

Whereas pressure ratio of shock compression may be adequately correlated to Mach Number M_F, the length and structure of the compression region may be expected to depend on M, on Reynolds Number based on duct diameter, and on Reynolds Number based on boundary-layer thickness.† The last parameter was not included in the attempted correlations we just mentioned.‡

The information available on shock compression in ducts, although inadequate in detail, clearly indicates that (1) the efficiency of shock compression is higher in constant-area than in divergent ducts and (2) several duct diameters are required for compression to run its full course. The advantages resulting from inclusion of a constant-area section at entry or at throat of supersonic diffusers are examined below.

DIFFUSERS WITHOUT CONTRACTION

Under this heading come subsonic geometry diffusers operating with supersonic entry velocities. Their performance is given in Figs. 9 and 10 in terms of diffuser entry Mach Number and stagnation pressure ratio P_0/P_0' across the diffuser.

Least efficient are diffusers without a long constant-area entry section and with large divergence. Castagna's results (6° conical) and Stewart's tests (about 12°, two-dimensional expansion), Fig. 9, are in good agreement, but the M.I.T. result, Fig. 10, obtained at $M = 1.75$ with a square, 6° divergent (in both planes) diffuser, falls a long way below and lies in line with

† Provided a fully turbulent pipe flow has not developed.

‡ The phenomenon of shock compression in ducts is analogous to flow at the base of bodies moving at supersonic speeds in that it involves interaction of shock waves with boundary layers and separated regions. The base flow phenomena were correlated in terms of ratio of boundary-layer thickness to base diameter by Chapman.[18]

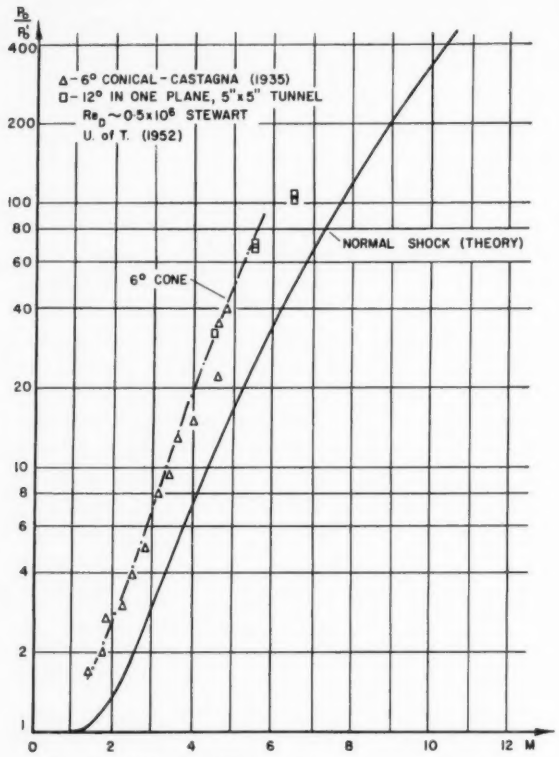

FIG. 9. Diffusers without contraction: pressure ratio.

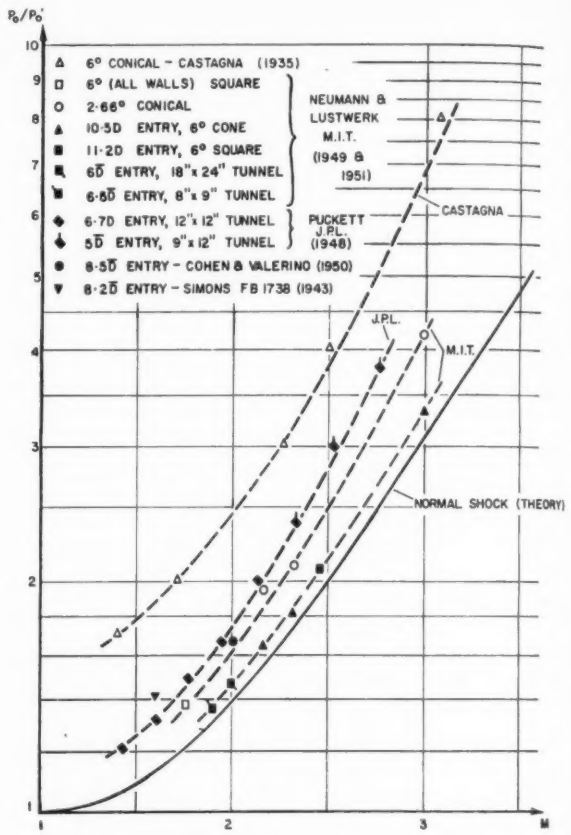

FIG. 10. Diffusers without contraction: pressure ratio.

other M.I.T. tests made with a small divergence (2.66°) conical diffuser.†

The expected favorable effect of a constant-area section at diffuser entry was demonstrated by NACA[17] tests of a 10- by 3.84-in. wind tunnel, fitted with a $M = 2$ nozzle, which was followed by 46 in. of constant-area section joined to a 5.5° (average, in both planes) rectangular diffuser. In Fig. 11, the pressure ratios recorded for various distances of the start of the pressure rise (or shock compression) in the constant-area duct from divergent diffuser entry are given. The required pressure ratio is reduced from 1.86 to 1.65, with length of compression in constant-area duct increased from 17 to 46 in.

In Fig. 10, pressure ratios for diffusers with a long constant-area entry are indicated by filled-in symbols. M.I.T. tests show smallest pressure ratios, which closely approach the ideal normal shock values and indicate the favorable effect of a constant-area entry. Comparable JPL,[15] NACA,[17] and German[16] results lie much higher, even exceeding already mentioned M.I.T. data for diffusers without a long constant-area entry.

Diffusers of the geometry here considered are not subject to large hysteresis effects. The pressure ratio required to obtain and maintain a given Mach Number in the working section is practically the same whether

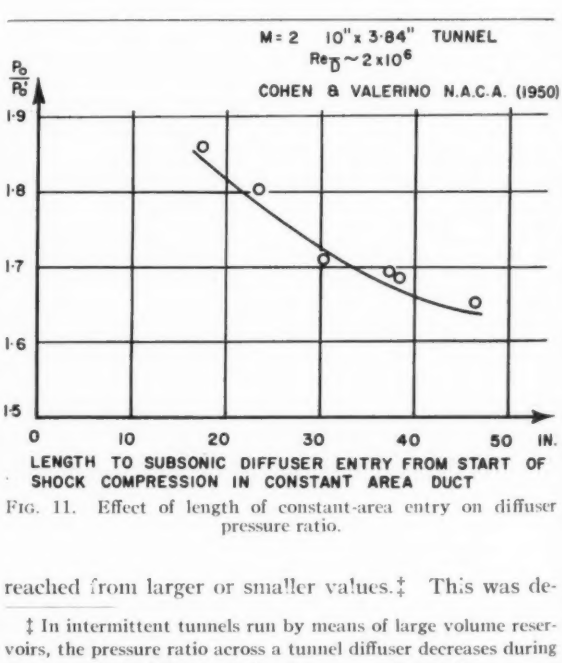
M = 2 10"x 3·84" TUNNEL
Re_D ~ 2x10⁶
COHEN & VALERINO N.A.C.A. (1950)
LENGTH TO SUBSONIC DIFFUSER ENTRY FROM START OF SHOCK COMPRESSION IN CONSTANT AREA DUCT
IN.

FIG. 11. Effect of length of constant-area entry on diffuser pressure ratio.

reached from larger or smaller values.‡ This was de-

† In general (cf. below), the M.I.T. tests show a smaller pressure ratio than obtained in other comparable experiments.

‡ In intermittent tunnels run by means of large volume reservoirs, the pressure ratio across a tunnel diffuser decreases during the run. With diffusers of the above type, the minimum starting and the actual flow breakdown pressure ratios are practically equal.

TABLE 2
Maximum Theoretical Diffuser Starting Contraction Ratio and Pressure Recovery ($\gamma = 1.4$)

M	ψ_{max}	$(P_0/P_0')\psi_{max.}$
1.0	1.000	1.00
1.2	1.023	1.00
1.4	1.068	1.01
1.6	1.120	1.04
1.8	1.170	1.11
2.0	1.216	1.20
2.5	1.316	1.59
3.0	1.391	2.27
3.5	1.445	3.33
4.0	1.488	5.00
4.5	1.520	7.14
5.0	1.543	10.75
6	1.577	21.79
7	1.598	41.15
8	1.614	73.53
9	1.624	124.69
10	1.632	202.43
∞	1.667	∞

termined for M.I.T. circular diffusers[12] and also in Stewart's[14] tests; of the two values of pressure ratios shown in Fig. 9 at $M = 5.5$ and 6.5, the higher (by less than 10 per cent) ones were required to start the flow.

Diffusers with Constant Contraction

Diffusers grouped in this category are characterized by a convergent entry section in which appreciable compression is achieved at supersonic speeds. They are therefore usually known as supersonic diffusers, in distinction to purely divergent, subsonic ones. The final compression to subsonic velocity occurs in supersonic diffusers by means of shock compression of the type already considered near the minimum or throat diffuser cross section, on its downstream side.

One of the fundamental design parameters is the diffuser contraction ratio $\psi = A_1/A^{*\prime}$, where A_1 = diffuser entry or nozzle exit area and $A^{*\prime}$ = diffuser minimum or throat area.

The maximum possible value of ψ at any entry diffuser Mach Number was derived theoretically† from considerations of starting the flow in a supersonic nozzle-supersonic diffuser system and corresponds to a normal shock at the diffuser entry Mach Number and sonic flow in the diffuser throat. The theoretical results are given in Table 2, where $\psi_{max.}$ denotes the maximum theoretically permissible contraction and $(P_0/P'_0)\psi_{max.}$ is the corresponding stagnation pressure ratio across the diffuser on the assumption of isentropic flow except for shock located at throat.

Typical variation of pressure ratio with contraction ratio for constant geometry diffusers is shown in Fig. 12. The top curve marked "starting" shows that supersonic flow at diffuser entry cannot be obtained for $\psi > 1.4$, irrespective of the pressure ratio applied. This limiting contraction closely agrees with the theoretical $\psi_{max.}$. The optimum contraction, at which smallest pressure ratio (≈ 3) is required to initiate the flow, is only slightly smaller than the limiting contraction.

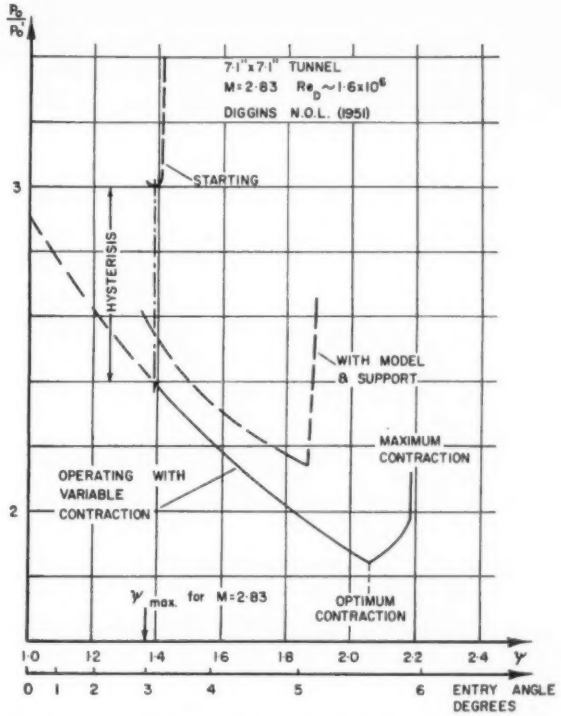

FIG. 12. Typical effects of contraction and model on diffuser pressure ratio.

Also in Fig. 12, a curve is included for a variable diffuser, whose contraction can be increased after supersonic flow at entry has started. Comparison of this curve with the one for starting or, in effect, constant contraction diffuser, shows that at the limiting contraction of 1.4, a pressure ratio of only 2.4 is required to maintain the flow compared with the starting pressure ratio of 3.

In Figs. 13 and 14, experimental contraction and pressure ratios of constant geometry diffusers are given in terms of entry Mach Number. At $M < 3.5$, maximum contraction ratios for starting,‡ Fig. 13, agree closely with the theoretical $\psi_{max.}$ values—a result somewhat unexpected in view of the already considered large discrepancies between theoretical and actual "normal shock" compression in ducts. The agreement is presumably due to the favorable influence on the boundary layer of the accelerated subsonic flow (during starting) downstream of the shock compression, in the diffuser contraction. In general, a smaller contraction is possible with diffusers having a long constant-area throat, because of additional losses in the throat section.

† See reference 2. This criterion was first established and experimentally checked in Germany.[7, 16]

‡ Practically equal to optimum contraction (for minimum pressure ratio), as pointed out above.

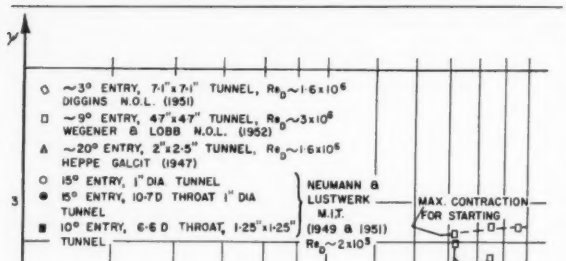
~3° ENTRY, 7·1"x7·1" TUNNEL, Re_D~1·6x10^6 DIGGINS N.O.L. (1951)
~9° ENTRY, 47"x47" TUNNEL, Re_D~3x10^6 WEGENER & LOBB N.O.L. (1952)
~20° ENTRY, 2"x2·5" TUNNEL, Re_D~1·6x10^5 HEPPE GALCIT (1947)
15° ENTRY, 1" DIA TUNNEL
15° ENTRY, 10·7D THROAT 1" DIA TUNNEL
10° ENTRY, 6·6D THROAT, 1·25"x1·25" TUNNEL
NEUMANN & LUSTWERK M.I.T. (1949 & 1951) Re_D~2x10^5
MAX. CONTRACTION FOR STARTING
OPTIMUM CONTRACTION
ψ max.
M

FIG. 13. Maximum contraction of constant geometry diffusers or for starting.

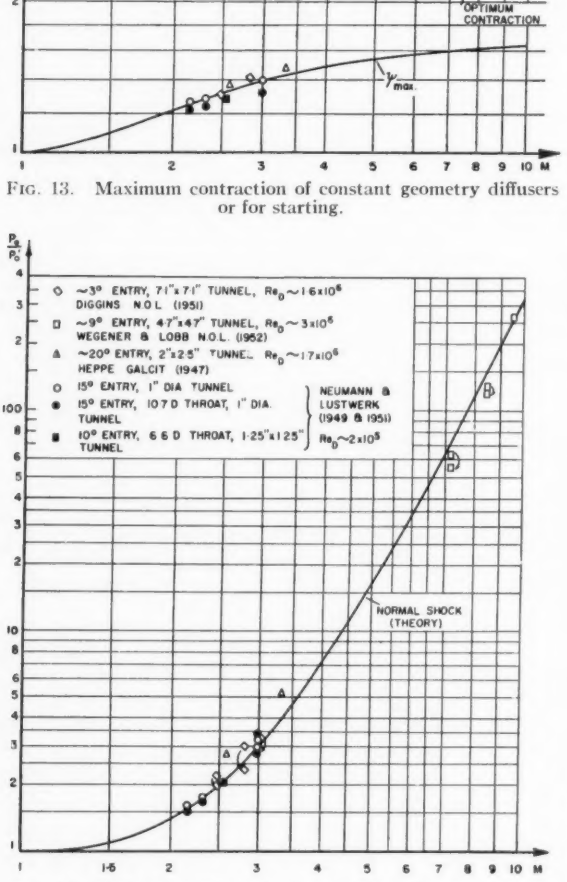
~3° ENTRY, 7·1"x7·1" TUNNEL, Re_D~1·6x10^6 DIGGINS N.O.L. (1951)
~9° ENTRY, 47"x47" TUNNEL, Re_D~3x10^6 WEGENER & LOBB N.O.L. (1952)
~20° ENTRY, 2"x2·5" TUNNEL, Re_D~1·7x10^6 HEPPE GALCIT (1947)
15° ENTRY, 1" DIA TUNNEL
15° ENTRY, 10·7D THROAT, 1" DIA. TUNNEL
10° ENTRY, 6·6D THROAT, 1·25"x1·25" TUNNEL
NEUMANN & LUSTWERK (1949 & 1951) Re_D~2x10^5
NORMAL SHOCK (THEORY)
M

FIG. 14. Diffusers with constant contraction: pressure ratio.

At Mach Numbers between 7 and 10 results from only one set of experiments[20] are available and give contraction ratios much in excess of $\psi_{max.}$. No explanation of this discrepancy with results at lower Mach Numbers can be offered at present.

The diffuser pressure ratios are given in Fig. 14 and, in general, closely follow the theoretical normal shock values. Hysteresis effects, already considered, are indicated in Fig. 14 by arrows, which connect pressure ratios required for starting and for maintaining the flow. Although long-throat diffusers require a smaller operating pressure ratio, their starting performance is similar to diffusers without a long throat.

In square or rectangular tunnels the supersonic diffuser contraction is usually two-dimensional and the question of optimum contraction angle arises. Since, for a given contraction ratio, shock losses increase and frictional wall losses decrease with increasing contraction angle, an optimum contraction angle might be expected to exist. The limited data available† indicate that at $M < 4$ small contraction angles, of the order of 3° to 4°, are favorable, higher pressure ratios being required with large contraction angles.‡ This is in agreement with further evidence obtained from tests of variable diffusers.

Variable Contraction Diffusers

Following the establishment of supersonic flow, a further contraction is possible with variable diffusers, the pressure ratio at which the flow breaks down being much lower than the starting pressure ratio. In order to take advantage of variable diffusers, a tunnel drive capable of providing momentarily (for starting) a higher than operating pressure ratio is usually required. Intermittent tunnels run by means of pressurized and/or evacuated reservoirs lend themselves very well to this type of operation.

Typical characteristics of variable contraction diffusers are shown in Fig. 12 at $M = 2.83$. Comparison of "starting" and "variable contraction" curves indicates that in the latter case much larger contractions and smaller pressure ratios are possible. The optimum contraction, at which a minimum pressure ratio is obtained, is significantly smaller than the maximum possible contraction.

Experimental results for variable diffusers are collected in Figs. 15 and 16. From Fig. 15 the maximum and optimum contraction and the effect of model mounted in the working section on optimum contraction can be estimated. Diffuser pressure ratios are given in Fig. 16. The minimum values indicated by the broken line are somewhat smaller than the theoretical ones for diffusers having $\psi_{max.}$ contraction.

With regard to the optimum contraction angle of variable diffusers, it appears that it increases with the Mach Number. In the NOL tests[19] (diffuser without long constant-area throat), an optimum throat location was determined, while the total (including convergence and divergence) diffuser length was kept constant. The optimum throat position was found to be at $5.35D$ from the diffuser entry for $M = 2.48$ and 2.83 and at $3.9D$ for $M = 4.92$, where D is the height of square tunnel working section. The corresponding

† Insufficient to separate Reynolds and Mach Number effects.

‡ This statement is based on comparison of NOL data with GALCIT results, Fig. 14. The M.I.T. results show lower pressure ratios with large contraction angles but also indicate the desirability of a small angle.[12]

entry angles were 4.5° and 5.6° at optimum contractions for the two lower Mach Numbers.

The above results were confirmed by R.A.E. tests at $M = 2.48$ with incomplete diffuser,[23] Fig. 17, which show that contraction ratio (and, hence, pressure recovery) increases with contraction angle decreasing.

Galcit tests,[21] Figs. 15 and 16, indicate relatively small optimum contraction ratios and pressure recoveries, which can be attributed to an excessively large diffuser entry angle (~28°).

On the other hand, apparently extremely low pressure ratios were obtained in M.I.T. tests at similar Mach Number, Fig. 16, in spite of a 20° contraction angle. It is not certain whether this was due to a long constant-area throat used in these tests.

Both NACA and NOL tests indicate that at hypersonic speeds (say $M > 5$) much larger diffuser entry angles (between 13° and 18°) should be used. The following results were obtained at NOL[20] with two different entry angles, at $M = 7.2$, $Re_D \sim 2 \times 10^6$:

Diffuser entry angle	= 7°	12.9°
Optimum ψ	= 5.5	5.5
Length to throat from diffuser entry	= 6.6D	3.6D
Subsonic diffuser angle	= 3°	3°
Min. P_0/P_0'	= 58	36

In the same series of experiments it was found that the effect of subsonic diffuser divergence (up to 5.5°) was negligible and that a constant-area throat† (3D length) had no effect on optimum contraction ratio and minimum pressure ratio; at contraction ratios smaller than optimum, parallel-throat diffuser gave slightly (about 10 per cent) smaller pressure ratios.

In two investigations the effect of Reynolds Number on diffuser performance was found to be small at hypersonic speeds. Bertram[22] found no change in the minimum diffuser pressure ratio with the variation of

† As pointed out in reference 20, in hypersonic tunnels operating at high stagnation temperature, it is advantageous to have a short diffuser throat in order to reduce regions of high heat-transfer rates and thus ease cooling problems.

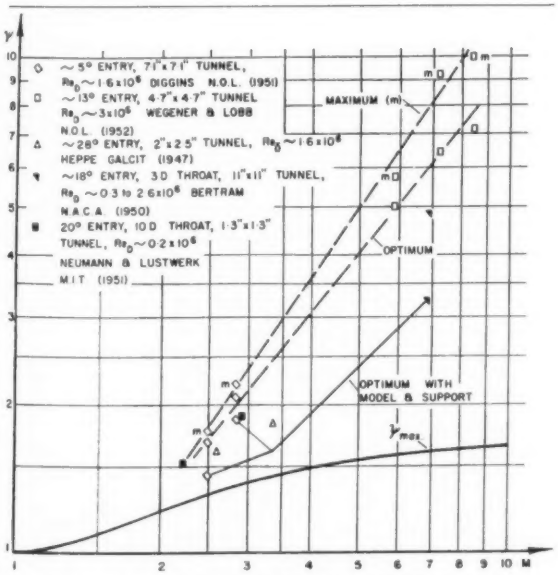
~5° ENTRY, 7.1"x7.1" TUNNEL, Re0~1.6x10^6 DIGGINS N.O.L. (1951)
~13° ENTRY, 4.7"x4.7" TUNNEL Re0~3x10^6 WEGENER & LOBB N.O.L. (1952)
~28° ENTRY, 2"x2.5" TUNNEL, Re0~1.6x10^6 HEPPE GALCIT (1947)
~18° ENTRY, 3D THROAT, 11"x11" TUNNEL, Re0~0.3 to 2.6x10^6 BERTRAM N.A.C.A. (1950)
20° ENTRY, 10D THROAT, 1.3"x1.3" TUNNEL, Re0~0.2x10^6 NEUMANN & LUSTWERK M.I.T. (1951)
MAXIMUM (m)
OPTIMUM
OPTIMUM WITH MODEL & SUPPORT
ψ max
ψ m
M

FIG. 15. Variable geometry diffusers: contraction ratio.

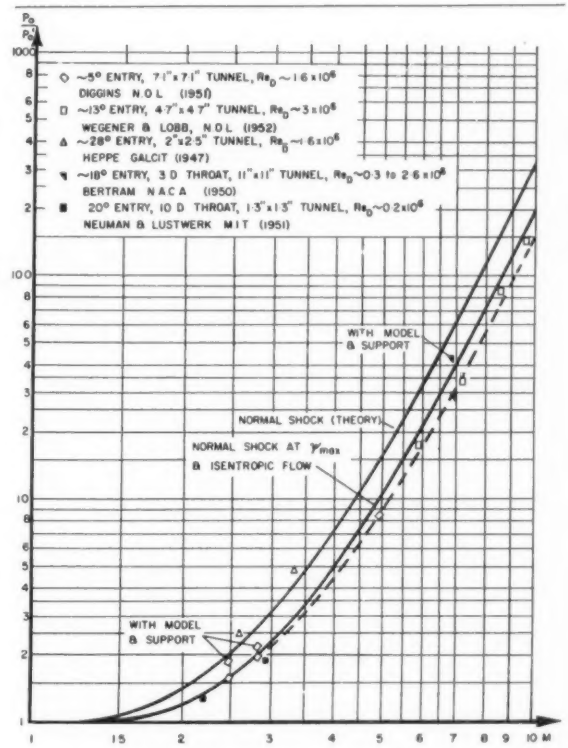
~5° ENTRY, 7.1"x7.1" TUNNEL, Re0~1.6x10^6 DIGGINS N.O.L. (1951)
~13° ENTRY, 4.7"x4.7" TUNNEL, Re0~3x10^6 WEGENER & LOBB N.O.L. (1952)
~28° ENTRY, 2"x2.5" TUNNEL, Re0~1.6x10^6 HEPPE GALCIT (1947)
~18° ENTRY, 3D THROAT, 11"x11" TUNNEL, Re0~0.3 to 2.6x10^6 BERTRAM N.A.C.A. (1950)
20° ENTRY, 10D THROAT, 1.3"x1.3" TUNNEL, Re0~0.2x10^6 NEUMAN & LUSTWERK M.I.T. (1951)
WITH MODEL & SUPPORT
NORMAL SHOCK (THEORY)
NORMAL SHOCK AT ψmax & ISENTROPIC FLOW
WITH MODEL & SUPPORT
M

FIG. 16. Variable geometry diffusers: pressure ratio.

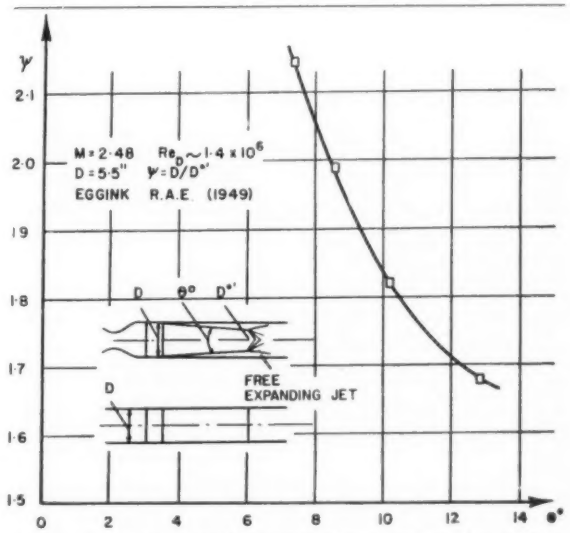

FIG. 17. Effect of angle of contraction on contraction ratio.

Re_D from 0.5 to 3 × 10^6, at $M \sim 6.86$ and $\psi = 2.8$. The NOL results, summarized below, indicate increase with Re_D in the maximum possible contraction but small change in the pressure ratio:

$M = 7.2$ $T_0 = 15°C$.

P_0 at.	5	10	20	30
$Re_D \times 10^{-6}$	1	2	4	6
ψ	6.6	7.5	9.2	10.4
P_0/P_0'	...	36	33.5	..

Conclusions

(1) About 88 per cent of theoretical pressure rise is obtained in subsonic small angle (7° cone) diffusers at $M \leq 0.9$.

(2) Shock compression in ducts may involve complete flow detachment in divergent ducts or flow separation in constant-area ducts with multiple shock systems extending over several diameters of duct length. The latter type of shock compression can be observed in wave-speed camera records of shock-tube flow. Shock compression losses decrease with duct divergence decreasing and static pressure ratios observed in constant-area tubes correspond (at least in one case) to theoretical normal shock values taken at mean or Fanno line Mach Numbers. In general, the phenomenon of shock compression in constant-area ducts can be expected to depend on Mach Number and Reynolds Numbers based on tube diameter and boundary-layer thickness (for a given boundary-layer flow).

(3) Pressure recovery of diffusers without contraction is improved by use of a long constant-area entry but is always smaller than the theoretical normal shock (i.e., Pitot tube) recovery.

(4) At Mach Numbers below 4, maximum contraction of constant geometry diffusers (or starting contraction of variable diffusers) is closely predicted by the simple theory. At optimum contractions (which are practically equal to maximum contractions) normal shock pressure recoveries are achieved, although appreciably larger starting pressure ratios are usually required at $M > 2$. Small angles of two-dimensional contractions, of the order of 3° to 4°, are favorable at $M < 4$ and increase to about 9° at $M = 7$ to 10.

(5) With variable diffusers, optimum contraction increases with Mach Number and is appreciably larger than starting or $\psi_{max.}$ contraction but smaller than maximum possible contraction. Contraction angles of the order of 5° are best at $M < 3$ and increase to 15° and more at $M = 7$ to 10. Minimum pressure ratios, appreciably smaller than the normal shock values, are obtained at $M > 2$ and amount to only half the normal shock stagnation pressure ratio at $M \sim 7$. Although performance of variable diffusers deteriorates when models are mounted in the working section, it is advantageous to use this diffuser type in hypersonic tunnels.

References

[1] Crocco, L., *Gallerie aerodinamiche per alter velocita (High Speed Wind Tunnels)*, L'Aerotechnica, Vol. 15, No. 3, pp. 237–75 and No. 7–8, pp. 734–778, 1935; Trans. No. 366, AMC, Dayton, Ohio, 1943.

[2] Lukasiewicz, J., *Supersonic Diffusers*, R.A.E. (Farnborough) Report Gas 8, 1946, and British A.R.C., R. & M. No. 2501, H.M.S.O., London, 1952.

[3] Naumann, *Efficiency of Diffusers at High Subsonic Speeds*, F.B. 1705, Germany, 1942, and British Trans. MAP-VG-RT321.

[4] Goethals, R., *Contribution a l'étude des diffuseurs en vue de l'application aux souffleries aérodynamiques subsoniques*, P. Sc. Tech. No. 243, Paris, 1950.

[5] Squire, H. B., *Experiments on Conical Diffusers*, R.A.E. (Farnborough) Report Aero 2216, 1947.

[6] Castagna, A., *Experimental Research on the Transformation of Energy of a Gas Flowing in a Pipe*, Atti della Reale Accademia delle Scienze di Torino, Vol. 70, pp. 284–317, 1935.

[7] Eggink, H., *Flow Structure and Pressure Recovery in Supersonic Tunnels*, F.B. 1756, Germany, 1943.

[8] Payman, W., and Shepherd, F., *Explosion Waves and Shock Waves, VI, The Disturbance Produced by Bursting Diaphragms with Compressed Air*, Proc. Roy. Soc. London, Series A, Vol. 186, 1946.

[9] Glass, I. I., *The Design of a Wave Interaction Tube*, Institute of Aerophysics, University of Toronto, Report No. 6, 1950.

[10] Lukasiewicz, J., *Adiabatic Flow in Pipes*, Aircraft Engineering, February and March, 1947.

[11] Keenan, J. H., and Neumann, E. P., *Friction in Pipes at Supersonic and Subsonic Velocities*, NACA TN No. 963, 1945.

[12] Neumann, E. P., and Lustwerk, F., *Supersonic Diffusers for Wind Tunnels*, J. Appl. Mech., pp. 195–202, June, 1949.

[13] Neumann, E. P., and Lustwerk, F., *High-Efficiency Supersonic Diffusers*, Journal of the Aeronautical Sciences, Vol. 18, No. 6, pp. 369–374, June, 1951.

[14] Stewart, J. D., *A Preliminary Investigation of the Effects of Condensation and Slip Flow in the UTIA 5" x 5" Supersonic Wind Tunnel*, Institute of Aerophysics, University of Toronto, Report No. 22, 1952.

[15] Puckett, A. E., *Design and Operation of a 12 inch Supersonic Wind Tunnel*, Institute of the Aeronautical Sciences, Preprint No. 160, July, 1948.

[16] Simons, F. P., *Investigations of Diffusers for Supersonic Wind Tunnels*, F.B. 1738, Germany, 1943.

[17] Cohen, C. B., and Valerino, A. S., *Investigation of Operating Pressure Ratio of a Supersonic Wind Tunnel Utilizing Distributed Boundary-layer Suction in Test Section*, NACA RM E50H04, 1950.

[18] Chapman, Dean R., *An Analysis of Base Pressure at Supersonic Velocities and Comparison with Experiment*, NACA Report No. 1051, 1951.

[19] Diggins, J. L., *Diffuser Investigations in a Supersonic Wind Tunnel*, NOL NAVORD Report 1570, 1951.

[20] Wegener, P. P., and Lobb, R. K., *N.O.L. Hypersonic Tunnel No. 4, Results II—Diffuser Investigation*, NOL NAVORD Report 2376, 1952.† Also *An Experimental Study of a Hypersonic Wind-Tunnel Diffuser*, Journal of the Aeronautical Sciences, Vol. 20, No. 2, pp. 105–110, February, 1953.

[21] Heppe, R. R., *Investigation of a Variable Geometry Supersonic Diffuser*, GALCIT Thesis, 1947.

[22] Bertram, M. H., *Investigation of the Pressure Ratio Requirements of the Langley 11 inch Hypersonic Tunnel with a Variable Geometry Diffuser*, NACA RM L50113, 1950.

[23] Eggink, H., *The Improvement in Pressure Recovery in Supersonic Wind Tunnels*, R.A.E. (Farnborough) Report Aero 2326, S.D. 34, 1949.

† Hypersonic diffuser test data quoted from this reference is based on experiments carried out with air at room stagnation temperature and therefore in presence of air condensation. Mach Numbers were obtained from Pitot/stagnation pressure ratios (insensitive to condensation) and it was ascertained that at $M = 7.2$ diffuser performance was only little affected by condensation, the minimum operating pressure ratio being about 10 per cent larger for condensation-free flow.

Transonic Flow Past Simple Bodies*

J. D. COLE,† G. E. SOLOMON,‡ AND W. W. WILLMARTH‡
California Institute of Technology

ABSTRACT

Transonic flow past conical tips, a lifting wedge, and a lifting flat plate is investigated theoretically and experimentally. Results on the drag and lift forces are presented. The existence of a closed smooth subsonic zone embedded in a supersonic flow field is demonstrated experimentally for transonic flow past conical tips. The cases discussed, together with the flow past wedge sections previously investigated, represent simple but fundamental cases for which the flow pattern from subsonic through sonic to supersonic flow can be obtained with relative ease. An understanding of these cases is extremely useful for handling the general transonic-flow problem.

(1) INTRODUCTION

IN THIS PAPER THE RESULTS of some experiments on transonic flow past two simple shapes—namely, a cone-cylinder and a double-wedge airfoil—are presented. The main aim of these experiments and the small amount of theory given here is to bring out some of the general features of transonic flow, especially over the whole transonic range of Mach Numbers. The authors wish to thank Prof. H. W. Liepmann for many discussions.

The special problems studied are the finite cone at zero angle of incidence and the symmetric double-wedge airfoil at extremely small angles of attack. The experiments were carried out in the 4- by 10-in. transonic Tunnel at GALCIT, which is described in reference 1. Details of the experimental technique are given in references 2 and 3. The main problem studied here for the cone is the breakdown of conical flow, or Taylor-Maccoll theory,[4] and the details of shock detachment. The behavior of the head drag curve in passing from subsonic to supersonic speeds is also discussed. For the double-wedge airfoil, the main problem studied is the behavior of the lift-curve slope and center of lift as the Mach Number varies. All of the results are presented in Figs. 1–17, which will now be discussed.

(2) FLOW PAST CONE-CYLINDERS

Consider first the cone at zero angle. Figs. 1 and 2 are schlieren photographs showing attached shock waves on 25° semiangle cones at $M_\infty = 1.415$ and 1.328, respectively. In Fig. 1 the shock is straight near the tip but curved at some distance away. In Fig. 2, at a lower Mach Number, the shock is curved right from the nose. Now, a curved shock indicates that the flow field is not conical and that the corner influences the nose. This implies the existence of a subsonic region extending from the corner to the nose. The location of the sonic line is easily found experimentally by reflecting weak waves from it as shown in Fig 3. The sonic lines found that way are shown in Figs. 4 and 5. Thus, for a given cone, as M_∞ decreases conical flow breaks down as soon as the Mach Number on the surface reaches 1, as would be expected. It can also be noticed on Figs. 4 and 5 that the sonic lines run from the shoulder to the nose, that they are straight near the nose, and that their location agrees well with the conical theory. From this the possibility that the flow is locally conical near the tip can be inferred.

For a more detailed investigation the entire density field was found by means of an interferometer. Also

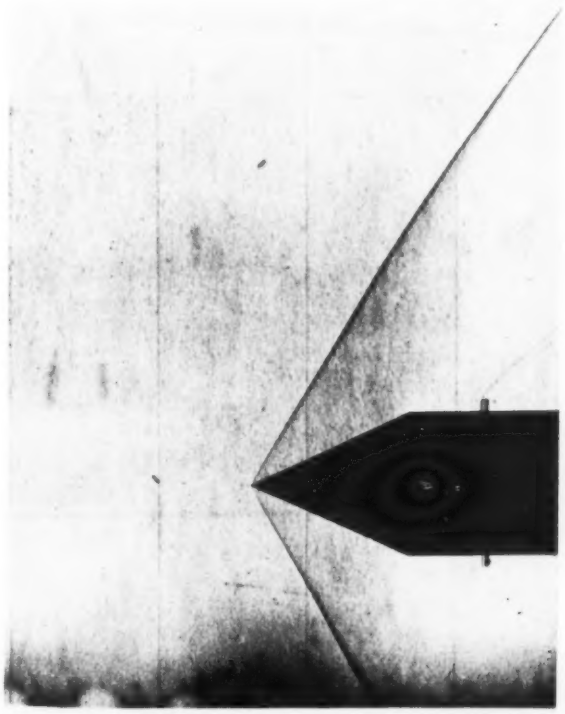

25° SEMI-ANGLE CONE-CYLINDER
$M_\infty = 1.415$
FIG. 1

Presented at the Aerodynamics Session, Twenty-First Annual Meeting, IAS, New York, January 26–29, 1953.

* Theoretical research supported by U.S. Air Force contract AF 18(600)383. Experimental research partially sponsored by the NACA, contract NAw-6154.

† Assistant Professor of Aeronautics and Applied Mechanics.

‡ Research Assistant.

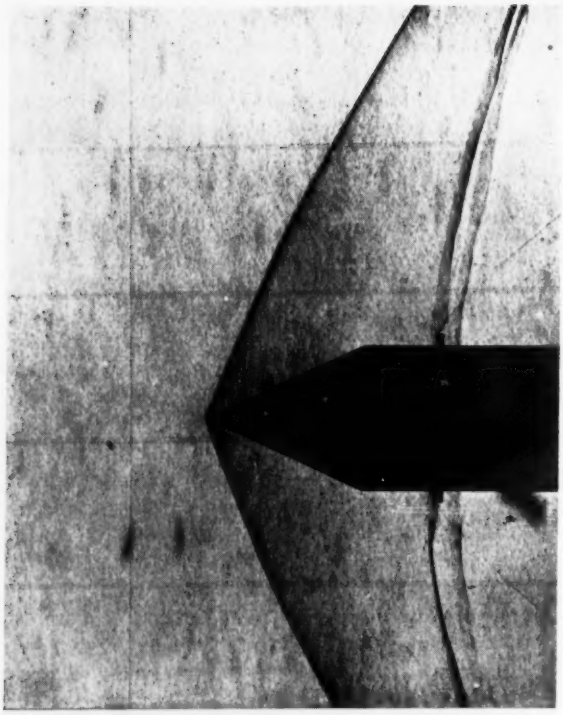

25° SEMI-ANGLE CONE-CYLINDER
$M_\infty = 1.328$
FIG. 2

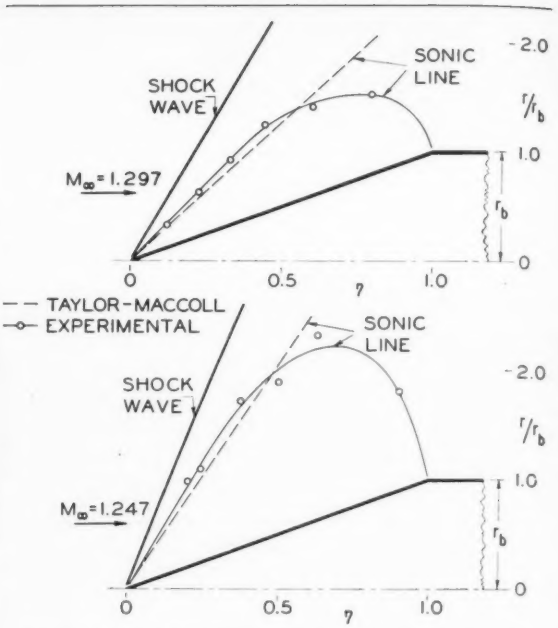

SONIC LINE LOCATION BY SHOCK REFLECTION
20° SEMI-ANGLE CONE-CYLINDER

FIG. 4

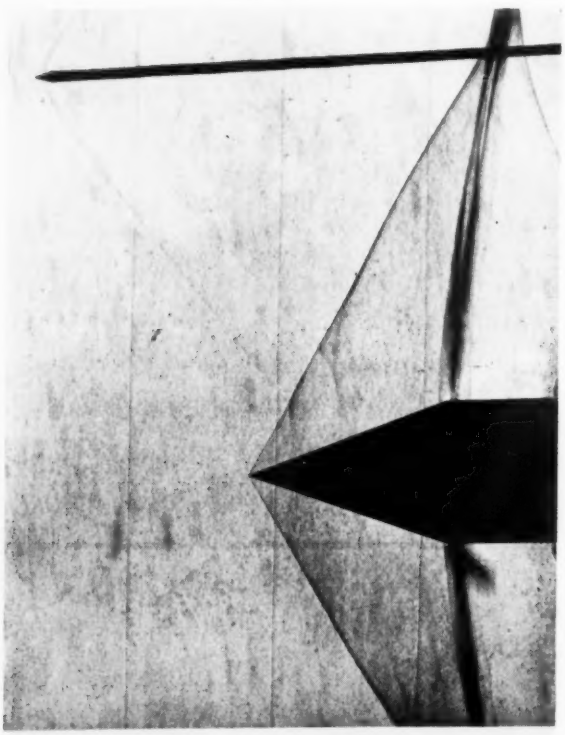

WAVE REFLECTION FROM SONIC LINE
20° SEMI-ANGLE CONE-CYLINDER
$M_\infty = 1.297$
FIG. 3

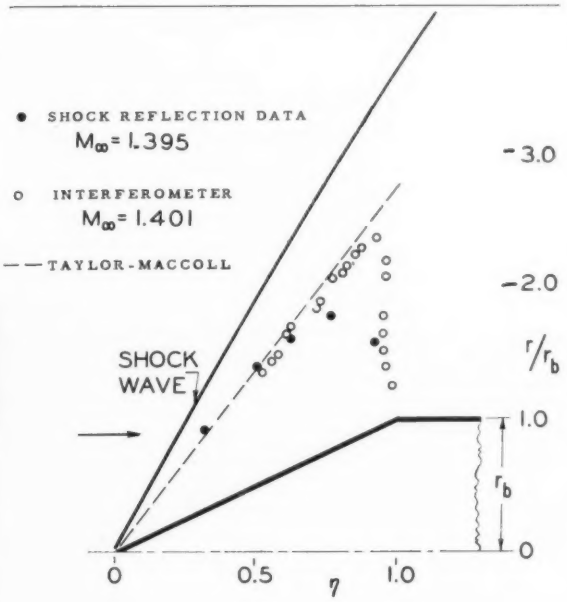

SONIC LINE LOCATION
25° SEMI-ANGLE CONE-CYLINDER

FIG. 5

FINITE FRINGE INTERFEROGRAM
30° SEMI-ANGLE CONE-CYLINDER
$M_\infty = 1.280$
FIG. 6

pressure measurements were obtained on the surface of various cones by means of models with pressure taps. A typical axially symmetric interferogram (30° cone, $M_\infty = 1.280$) is given in Fig. 6. Interferometric results presented in Figs. 7, 8, and 9 show the Mach Number fields for a 25° semiangle cone for a series of three decreasing Mach Numbers 1.401, 1.273, and 1.229. The theoretical Mach Number at which the flow on the surface becomes sonic for this cone is 1.500. Already at $M_\infty = 1.401$ there is a considerable subsonic region. The sonic line runs from the corner to the tip, and both the sonic line and the shock are straight near the nose. The pressures measured near the nose (Fig. 12) check the Taylor-Maccoll theory, thus verifying the idea of locally conical flow near the tip. As the Mach Number decreases to 1.273; Fig. 8 shows how the sonic region is enlarged and how the sonic line now runs from the corner to the shock. The shock is curved from the tip. Fig. 9 shows a further decrease in M_∞ and the pattern when the wave is detached.

Some explanation of the various régimes observed is given in Fig. 10. In Fig. 10 a transonic form of the shock polar is shown, with abscissa u = component of velocity perturbation from sonic and v = radial component of velocity. The points on the shock polar represent all possible downstream states that can be

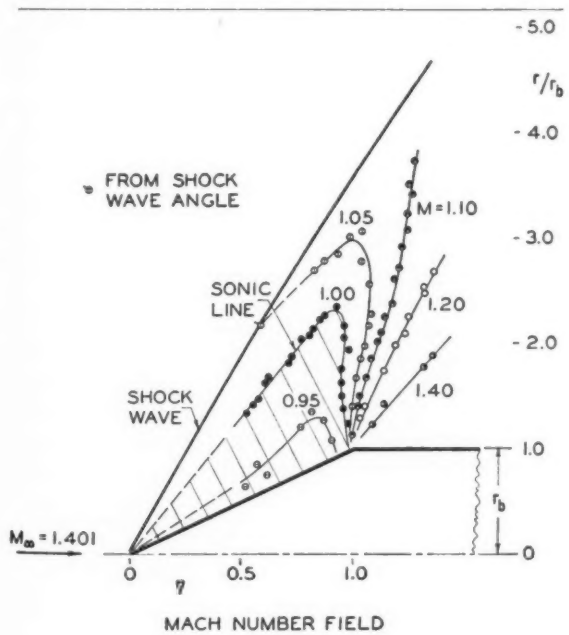

MACH NUMBER FIELD
FOR
25° SEMI-ANGLE CONE-CYLINDER
FIG. 7

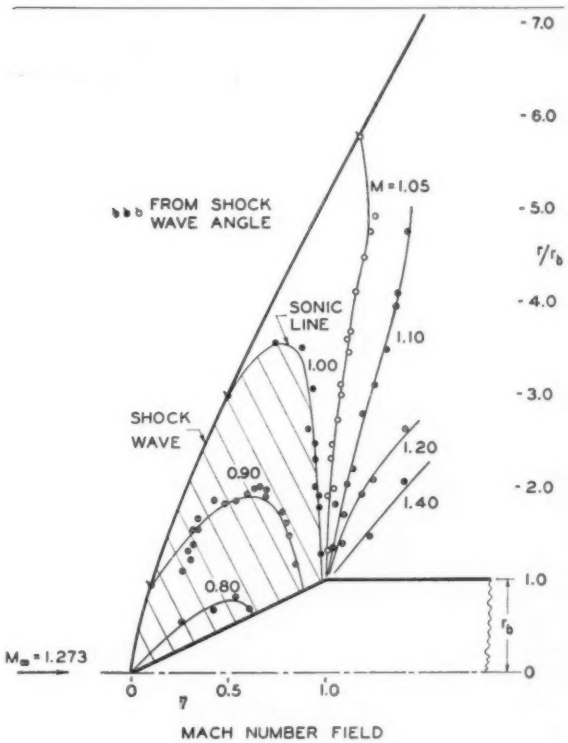

MACH NUMBER FIELD
FOR
25° SEMI-ANGLE CONE-CYLINDER
FIG. 8

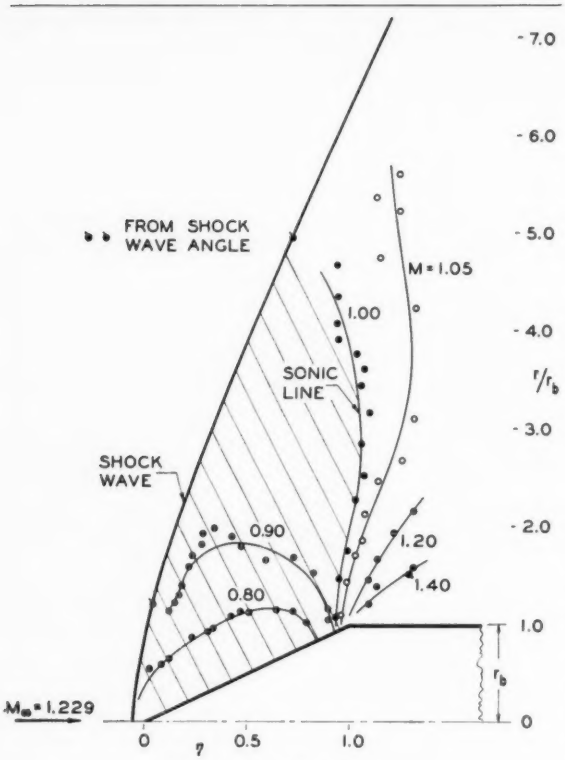

MACH NUMBER FIELD
FOR
25° SEMI-ANGLE CONE-CYLINDER

FIG. 9

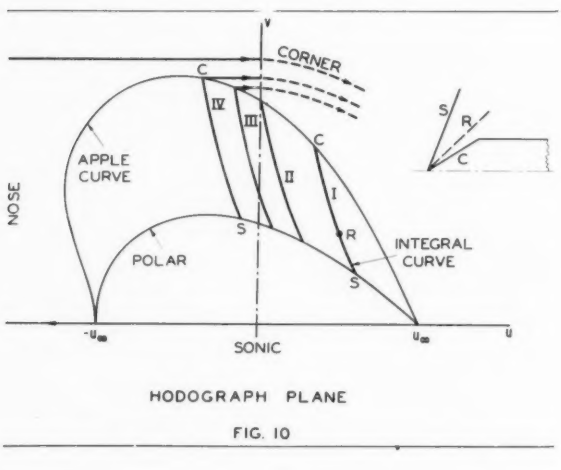

HODOGRAPH PLANE

FIG. 10

reached through a shock with the initial state $u = u_\infty$, $v = 0$. Corresponding to each point on the polar is a given wave angle. Thus the points immediately behind the shock wave S on the cone appear as a point or points on the shock polar. The curves I to IV are integral curves of the equations of motion and are found as follows (see reference 4 or 5): It is assumed that the flow field is conical so that the physical properties p, u, v, etc., are constant on rays, like R in Fig. 10. The partial differential equations of motion can be expressed as a second-order ordinary (nonlinear) differential equation for v as a function of u. The solutions of this differential equation are the integral curves. Two boundary conditions for the integral curve are given on the shock polar—namely, v and dv/du. The slope of the integral curve at a point, dv/du, determines the slope of the corresponding ray in the physical plane. An end point C for the integral curve is determined by the requirement that the slope of the ray, depending on dv/du, should equal v/a^* so that, approximately, a solid cone surface can be inserted in the flow. The locus of all the possible end points of integral curves starting on the shock polar is called the "apple" curve. A typical integral curve corresponding to a purely supersonic field is represented by I in Fig. 10. The point S corresponds to the state immediately behind the shock. Each point R on the integral curve corresponds to the entire ray R in the physical plane. The end point C on the "apple" curve represents the ray that lies along the cone surface. If now we think of increasing the cone angle, with M_∞ fixed, the integral curve moves to the left in Fig. 10 until a curve like II is obtained. At II the end point is sonic so that sonic velocity is reached on the cone surface. If the cone angle is increased further, subsonic flow occurs next to the surface, the corner influences the nose, and conical flow in the large is no longer possible. However, the flow may still be locally conical, as indicated by the integral curve III. As the cone angle is increased from II, the velocity at the corner remains sonic. The velocity near the tip is given by the end point of III, and the cone surface is represented by the horizontal line from the end point of III to the sonic line. The entire integral curve maps to the nose point in the physical plane; each point on the integral curve corresponds to a ray in the neighborhood of the nose. The sonic line intersects III or runs from the corner to the nose. Now as the cone angle is increased further, integral curves like IV are obtained which are the same as III, except that the sonic line runs from the nose to the shock. As the cone angle is increased still further, the cone surface cannot be reached as a point on the "apple" curve, or by a locally conical flow, so that the shock must be detached. Thus the detachment is given by the largest possible deflection that can be obtained by conical flow or is correctly given by Taylor-Maccoll theory. It should be remarked that an experimental determination of the detachment Mach Number is difficult because of the slow rate of detachment for a cone. Thus, we have a description in the hodograph plane of all the régimes observed experimentally.

The effect of these various régimes as M_∞ decreases, for a fixed cone, is shown in the head-drag curves, based on p_∞, in Fig. 11. For high values of M_∞ there

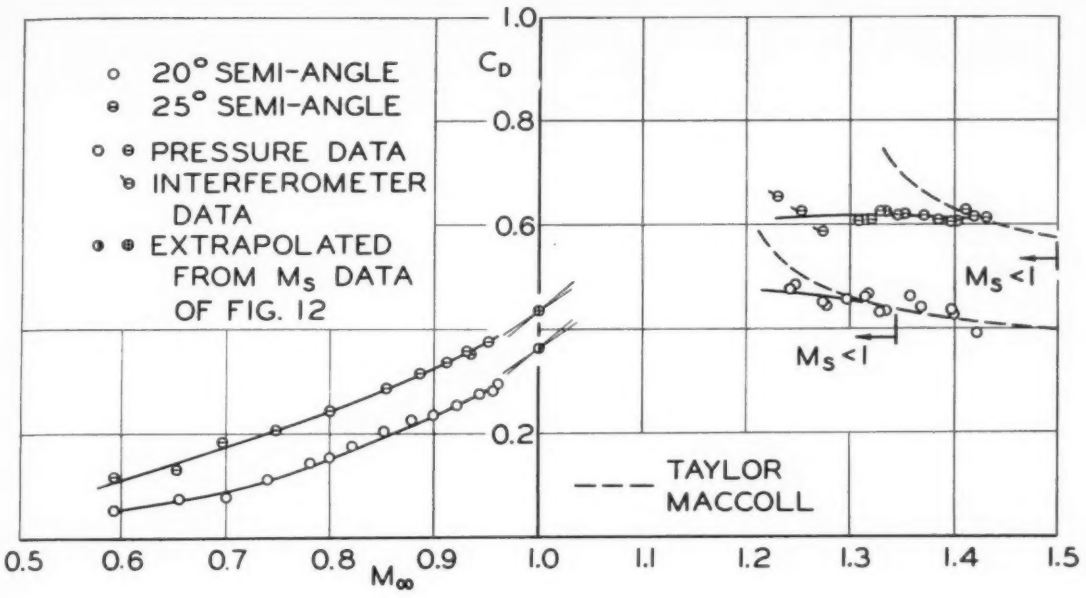

DRAG COEFFICIENTS FOR CONE-CYLINDERS

FIG. 11

is good agreement with conical-flow theory. As M_∞ decreases, conical-flow theory breaks down when the surface Mach Number is 1. As M_∞ is decreased further, the pressure is increased only near the tip and remains sonic near the shoulder. Thus, the drag curve falls below the conical theory. Subsonic points are also given on the figure and show a gradual rise of drag as $M_\infty \to 1$. The slope of the head-drag curve at $M_\infty = 1$ can be given approximately by applying the Principle of Stationarity of Local Mach Number. This Principle was enunciated and verified for two-dimensional flows in reference 7. The Principle states that $(\partial M/\partial M_\infty)_{M_\infty=1} = 0$; it is based on the idea that, as $M_\infty \to 1$, the head shock is infinitely distant from the body. For $M_\infty{}^2 = 1 + \epsilon$, the Mach Number behind the normal shock is $M_n{}^2 = 1 - \epsilon$. Then the flow field at large distances is effectively subsonic with a Mach Number $M_{\ell\infty}{}^2 = 1 - \epsilon$. Thus the local Mach Number remains the same as the free-stream Mach Number passes through 1. By applying the Principle and using the pressure-Mach Number relations, it can be deduced that

$$\left(\frac{\partial C_D}{\partial M_\infty}\right)_{M_\infty=1} = \frac{4}{\gamma+1}\left(1 - \frac{C_{DM_\infty=1}}{2}\right)$$

where C_D = head-drag coefficient. Roughly estimating $C_{DM_\infty=1}$ gives a good estimate for the slope as shown in Fig. 11. The stationarity of the local Mach Number was also checked experimentally. The results are shown in Fig. 12, where the local Mach Number is plotted as a function of the free-stream Mach Number for various chordwise stations. The flattening of the local Mach Number curves as $M_\infty \to 1$ is evident.

The Principle of Stationarity can be extended to the curvature of local Mach Number $(\partial^2 M/\partial M_\infty{}^2)_{M_\infty=1} = 0$. This result follows from the plausible assumption that the local Mach Number is a nondecreasing function of the free-stream Mach Number near $M_\infty = 1$ or $\partial M/\partial M_\infty \geqslant 0$. This assumption is verified experimentally in reference 7 and in Fig. 12.†

It should also be remarked that Yoshihara has computed, by relaxation calculations, the pressure on a slender cone at $M_\infty = 1.00$ and has experimentally verified the results.[8]

The above experimental results cannot be used to test the transonic axially symmetric similarity rules as derived by von Kármán[9] and Oswatitsch and Berndt.[10] The derivation of the similarity rules employs some linearized surface tangency condition that is probably valid for small cone angles. The nose angles of the experimental models were too large for the linearization of the boundary conditions to be valid.

It can be shown, however, that the axially symmetric transonic equations are a good approximation to the exact equations. A second-order solution for the flow past a semi-infinite cone has been found[3] using the transonic equations, and the results for local Mach Number agree well with the exact conical solution (see Fig. 13).

† The same results can be deduced analytically (for example, see reference 13).

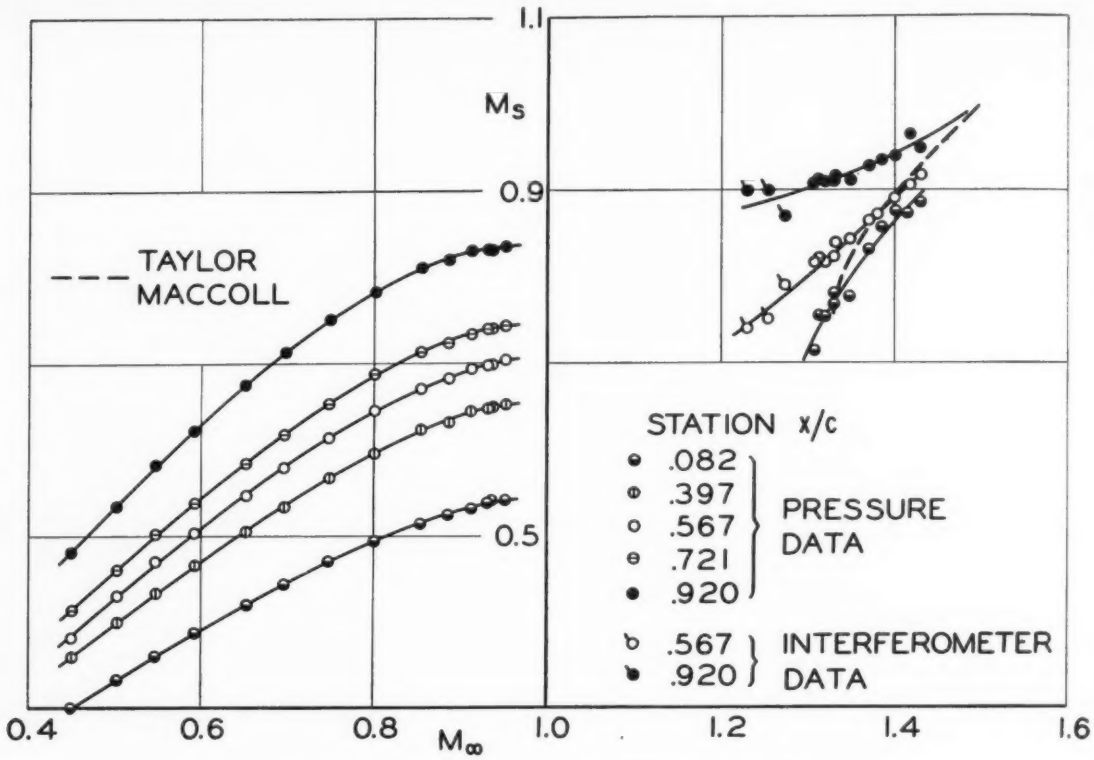

SURFACE MACH NUMBER, M_S
ON
25° SEMI-ANGLE CONE - CYLINDER

FIG. 12

Fig. 14, a schlieren picture of the typical flow pattern of a cone at $M_\infty < 1$, is the last figure pertaining to the cone. It is noteworthy that there is no shock of appreciable strength emanating from the corner.

(3) Double-Wedge Airfoil

Surface pressure measurements were made for the completely symmetric 5 per cent thick double-wedge airfoil at small angles of attack by sliding a static pressure probe along a line touching the wedge shoulder and parallel to the wedge chord line. The details of the technique are given in reference 2. The lift coefficients are obtained by integration of the pressure distributions, and the results are plotted in transonic similarity form in Fig. 15. The lift-curve slope $\bar{C}_L/\alpha$ for small angles is given, and it should be remarked that over the range of angles tested, $\alpha = 0°$ to $2°$, the lift was a linear function of α for all M_∞. The salient features of Fig. 15 are as follows: For low M_∞, the lift-curve slope follows the Prandtl-Glauert correction, but the incompressible slope for this airfoil is somewhat less than 2π. There is a striking drop in lift coefficient as M_∞ increases near

$$\xi_\infty = (M_\infty^2 - 1)/[(\gamma + 1)\,(t/c)]^{2/3} = -1$$

As $M_\infty \to 1$, the lift-curve slope goes toward the theoretical value given by Guderley and Yoshihara in reference 11. An explanation of the drop in lift is the following: As M_∞ increases, a supersonic zone forms behind the shoulder. Near $\xi_\infty = -1$, this supersonic zone grows rapidly in size, and its terminating shock moves from the corner to the trailing edge with a small increase in ξ_∞. The rear half of the airfoil operating supersonically is inefficient in the production of lift. It should be emphasized that the phenomenon is not one of separation or stalling, since the boundary layer remained attached during the experiments.

The arrival of the terminating shock at the trailing edge is interesting from the point of view of theory. It means that the conditions for the flow leaving the trailing edge can be satisfied locally. The problem of satisfying the Kutta condition disappears. This

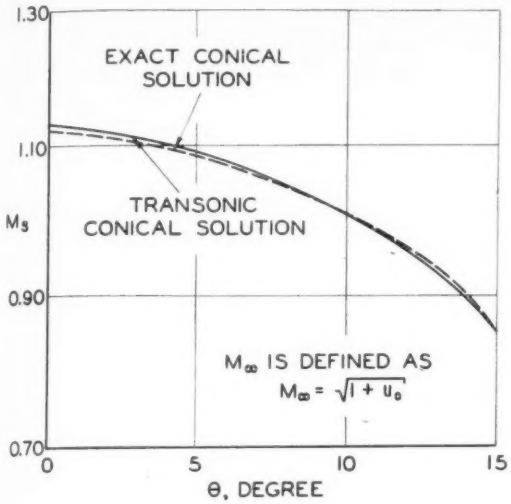

TRANSONIC CONICAL SOLUTION
SURFACE MACH NUMBER vs. CONE SEMI-ANGLE
$u_\infty = 0.25$ $M_\infty = 1.12$

FIG. 13

20° SEMI-ANGLE CONE-CYLINDER
$M_\infty = 0.942$

FIG. 14

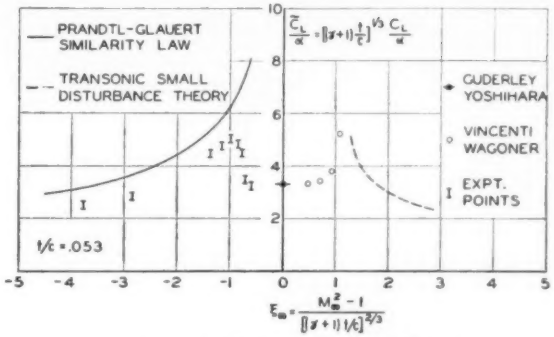

LIFT CURVE SLOPE OF A DOUBLE WEDGE AT SMALL ANGLES OF ATTACK

FIG. 15

fact was used by Guderley and Yoshihara in their solution at $M_\infty = 1$.[11]

Pressure distributions showing the three typical cases—practically no shock, shock partway back, and shock off the trailing edge—are shown in Fig. 16. It might be remarked that it is the effect of the boundary layer which prevents any supersonic zone from forming at $M_\infty = 0.309$.

Another interesting quantity is the location of the center of lift. If the local pressure difference across the airfoil is linear in the angle of attack, so are the lift and moment. The center of lift is thus independent of the angle of attack. However, the center of lift moves rearward to a maximum value and then forward as $M_\infty \to 1$. At low subsonic speeds, the center of lift is located at one-quarter chord; for $M_\infty = 1$, the center of lift is located at 30 per cent chord, according to the solution of Guderley and Yoshihara.[11] Fig. 17 shows the experimental result illustrating the rearward trend of center of lift as M_∞ increases. The maximum rearward position of center of lift (40 per cent chord) corresponds to M_∞ such that the terminating shock waves of the supersonic zone leave the airfoil. The center of lift travel can be explained as follows: As M_∞ increases from zero, supersonic zones terminated by shocks appear behind the corner. Because of the small angle of attack, the terminating shocks occur at different chordwise stations (Fig. 16) resulting in an appreciable lift over the rear half. This shifts the center of lift toward the rear. The effect increases with increasing free-stream Mach Number until the shocks leave the trailing edge. Any further increase in Mach Number produces relatively little change in lift on the rear half, and the center of lift moves forward. Theoretically, at $M_\infty = 1$, only 25 per cent of the lift comes from the rear half.[11] The theoretical center of lift for $M_\infty > 1$ is a continuation of the subsonic curve. The center of lift moves forward as M_∞ increases until a Mach Number close to the attachment Mach Number is reached. The center of lift then moves rearward to the one-half chord point, its supersonic value. The theory for $M_\infty > 1$ is presented by Vincenti and Wagoner.[12]

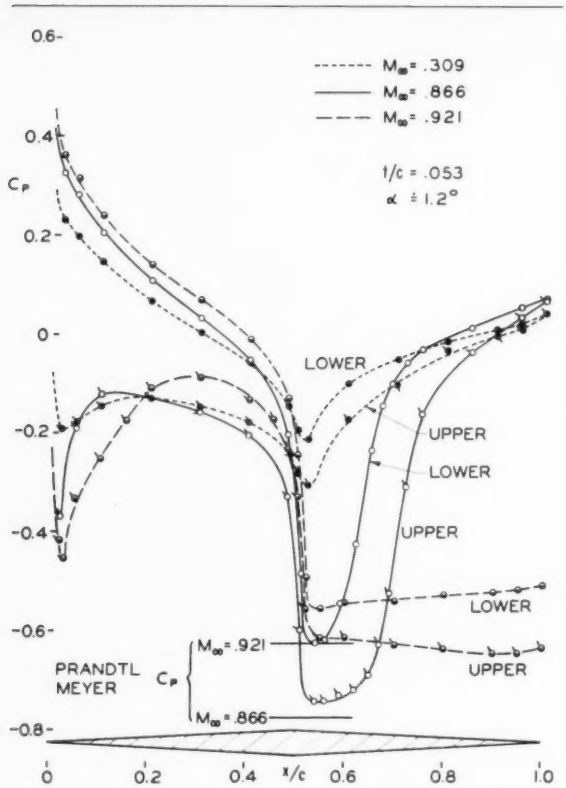

PRESSURE DISTRIBUTION ON A DOUBLE WEDGE AT SUBSONIC MACH NUMBERS

FIG. 16

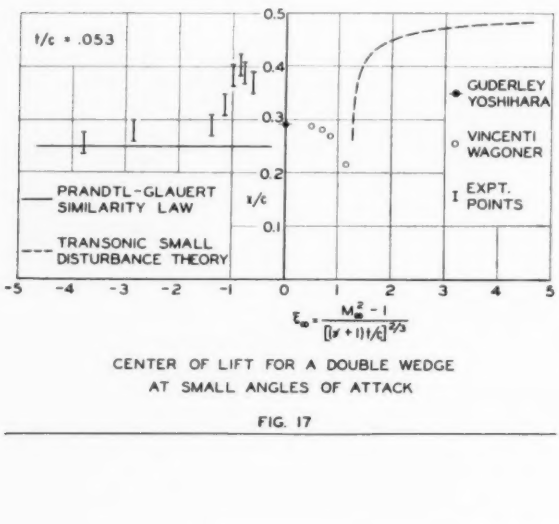

CENTER OF LIFT FOR A DOUBLE WEDGE AT SMALL ANGLES OF ATTACK

FIG. 17

A nonlinear effect also appears for the higher Mach Numbers. When the terminating shock waves are no longer on the airfoil, the center of lift travels forward as the angle of attack increases. This means that the moment is not linear in α. The forward shift comes from the strong expansion evident on the upper surface near the leading edge (Fig. 16, $M_\infty = 0.921$). It is interesting that there are deviations from linear behavior at angles of attack which are less than the wedge-nose semiangle (3°).

Two problems are interesting for future experiments—namely (a) evaluating the range of validity of the assumption of linearity in α (theoretically a flat plate has $C_L \sim \alpha^{2/3}$ at $M_\infty = 1$); (b) behavior of lift near the wing tips.

References

[1] Liepmann, H. W., Roshko, A., and Dhawan, S., *On Reflection of Shock Waves from Boundary Layers*, NACA TN No. 2334, 1951.

[2] Willmarth, W. W., *On the Measurement of Surface Pressure with a Static Probe*, to appear in the Journal of the Aeronautical Sciences.

[3] Solomon, G. E., *Transonic Flow Past Cone-Cylinders*, Ph.D. Thesis, California Institute of Technology, March, 1953. (To appear soon as an NACA TN.)

[4] Taylor, G. I., and Maccoll, J. W., *The Air Pressure on a Cone Moving at High Speeds*, Proc. Roy. Soc. of London, Ser. A. Vol. 139, p. 278, 1933.

[5] Busemann, A., *Drücke auf kegelförmige Spitzen bei Bewegung mit Überschallgeschwindigkeit*, Zeit. f. Ang. Math. u. Mech., Vol. 9, p. 496, 1929.

[6] Courant and Friedrichs, *Supersonic Flow and Shock Waves*; Interscience Publishers, New York, 1948.

[7] Liepmann, H. W., and Bryson, A. E., *Transonic Flow Past Wedge Sections*, Journal of the Aeronautical Sciences, Vol. 17, No. 12, p. 745, December, 1950.

[8] Yoshihara, H., *On the Flow Over a Cone-Cylinder Body at Mach Number One*, to be published as an Air Force Technical Report.

[9] von Kármán, Th., *The Similarity Law of Transonic Flow*, Jour. of Math. & Physics, Vol. 26, October, 1947.

[10] Oswatitsch, K., and Berndt, S. B., *Aerodynamic Similarity at Axisymmetric Transonic Flow Around Slender Bodies*, Royal Inst. of Tech., Sweden, Aero. TN 15, 1950.

[11] Guderley, G., and Yoshihara, H., *Two-Dimensional Unsymmetric Flow Patterns at Mach Number One*, Air Force Tech. Rept. 6883, 1952.

[12] Vincenti, W., and Wagoner, C., *Theoretical Study of the Transonic Lift of a Double Wedge Profile with Detached Bow Wave*, NACA TN No. 2832, 1952.

[13] Guderley, Gottfried, *Two-Dimensional Flow Patterns with a Free-Stream Mach Number Close to One*, U.S. Air Force Technical Report No. 6343, 1951.

Free-Flight Determinations of the Drag Coefficients of Spheres

ALBERT MAY* AND W. R. WITT, JR.†
U.S. Naval Ordnance Laboratory

SUMMARY

Drag coefficients have been determined in the NOL Pressurized Ballistics Range for steel and aluminum spheres 1/4 to 3/4 in. in diameter. The Mach Number ranged from 0.8 to 4.7, and, by using air pressures from 1/120 to 1 atmosphere, the Reynolds Number was varied separately over a range of 1.14×10^3 to 8.4×10^6. The drag-coefficient data obtained, together with the results of other investigators, permit a plotting of the variation of drag coefficient over a large region of Mach Numbers and Reynolds Numbers. The variation of C_D was found to be only about 10 per cent in the range $1.6 < M < 4.7$ and $4.0 \times 10^3 < Re < 1.0 \times 10^6$.

INTRODUCTION

DETERMINATIONS OF THE DRAG COEFFICIENTS of spheres at various Mach and Reynolds Numbers have been made in the NOL Pressurized Ballistics Range for the Engineering Research Institute at the University of Michigan in connection with upper-atmosphere research for the Meteorological Branch of the Signal Corps. Because of the low air densities in the upper atmosphere, the Reynolds Number is much lower for a given Mach Number and sphere size than it would be at sea level. The purpose of the present program was to provide data on the drag coefficient of spheres in a supersonic region ($1.4 < M < 3.3$, $10^3 < Re < 10^5$) in which reliable data were almost entirely lacking.

The Pressurized Ballistics Range, shown in Fig. 1, is an enclosed tube 318 ft. long permitting the firing of projectiles through air at any pressure from 6 atmospheres to less than 1/100 atmosphere. The air temperature of the room in which the range is located is maintained at 74°F., and the temperature in the range is changed only a few degrees from this value by variations of the range pressure. Photographs can be taken by the spark-shadowgraph method at any number of the 25 stations with which the range is equipped. The positions of these stations are known to an accuracy better than 0.002 ft., and readings of the shadowgraph plates can be made to the same accuracy. The relative times at which eight of these shadowgraphs are taken can be determined by the use of an RCA counter chronograph. The counters read to 10^{-7} sec., and inaccuracies in the time determinations are less than 0.2 microsec.

EXPERIMENTAL DETAILS

The spheres were fired from a smooth-bore gun having a caliber of 20 mm., with the sphere mounted in a light plastic sabot as shown in Fig. 2. After the sphere and sabot are ejected from the gun, the gas pressure that has built up between sphere and sabot causes them to separate, and the sabot is left behind because of its large deceleration. At very low air pressures, the drag on the sabot was inadequate to effect proper separation of sabot and projectile. This difficulty was obviated by using a sabot split lengthwise so that the halves of the sabot were blown apart rapidly.

In order to obtain drag-coefficient values for a Reynolds Number range of 100 to 1 while the Mach Number varied only by a factor of 2.4, both sphere size and air pressure were changed. The Reynolds Number, $\rho v d/\mu$,

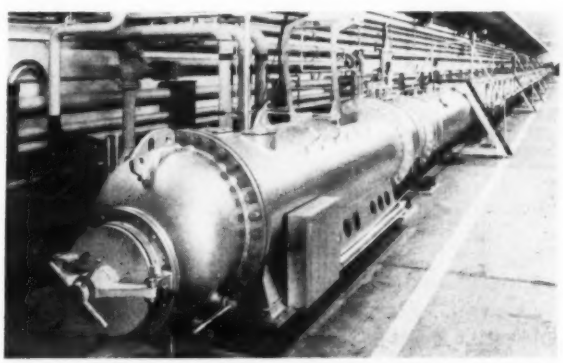

FIG. 1. NOL Pressurized Ballistics Range permitting independent variation of Mach Number and Reynolds Number.

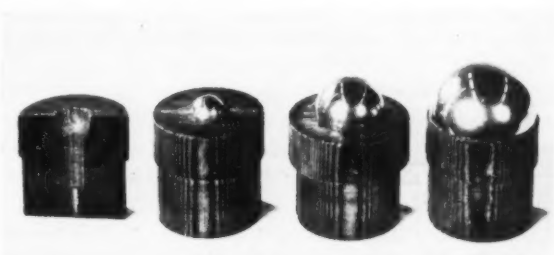

FIG. 2. Several sizes of spheres with their launching sabots. *Left*, half a sabot split to hasten separation from the sphere.

Received March 4, 1953.

* Chief, Range Branch, Aerodynamics Division.

† Project Engineer.

TABLE 1

Drag Coefficients from the Firing of Spheres

Round	Diameter, In.	Material	Pressure, Mm. per Hg	Mach Number	Reynolds Number $\times 10^{-4}$	C_D
362D	3/4	Steel	441	1.90	47.1	0.999
362C	3/4	Steel	290	1.94	31.6	1.000
361D	3/4	Steel	271	2.62	40.0	0.972
364D	3/4	Steel	184	2.66	27.5	0.950
363D	3/4	Steel	184	1.78	18.32	1.012
358D	3/4	Steel	174	2.77	27.0	0.947
360D	3/4	Steel	127	2.62	18.61	0.947
363C	3/4	Steel	124.5	1.60	11.11	1.019
364C	3/4	Steel	109.2	2.71	16.53	0.941
438C	3/4	Steel	62.3	2.85	9.79	0.932
441B	1/2	Steel	648.0	3.48	84.5	0.964
440C	1/2	Steel	311.0	4.20	48.9	0.934
361C	1/2	Steel	185.0	1.44	9.96	1.012
439B	1/2	Steel	124.1	1.25	5.80	0.955
441A	1/2	Steel	120.5	4.69	21.0	0.906
358C	1/2	Steel	105.0	2.15	8.40	0.942
438D	1/2	Steel	101.8	2.96	11.28	0.955
360C	1/2	Steel	76.5	2.62	7.45	0.937
360A	1/2	Steel	75.5	1.66	4.67	0.942
437D	1/2	Aluminum	76.6	1.52	4.32	0.923
437A	1/2	Aluminum	34.4	2.57	3.31	0.923
436A	1/2	Aluminum	13.0	3.01	1.518	0.938
491C	1/2	Aluminum	6.85	2.94	0.810	0.978
490B	1/2	Aluminum	6.84	2.45	0.671	0.985
489B	1/2	Aluminum	6.65	3.26	0.870	0.957
490C	1/2	Aluminum	6.55	2.70	0.712	0.986
491B	1/2	Aluminum	6.32	2.19	0.559	0.995
442B	1/2	Magnesium	24.4	1.28	1.161	0.850
438B	1/2	Magnesium	21.2	1.46	1.155	0.884
440D	3/8	Steel	761.4	3.13	73.5	0.962
435	3/8	Steel	81.6	3.01	6.88	0.934
443C	5/16	Aluminum	88.0	4.58	9.38	0.906
367B	9/32	Steel	143.3	1.66	5.04	0.948
367A	9/32	Steel	103.9	1.79	3.89	0.943
362A	9/32	Steel	36.5	2.83	2.15	0.938
366B	9/32	Steel	35.0	2.67	1.942	0.940
366A	9/32	Steel	23.0	2.80	1.333	0.951
365A	9/32	Steel	16.8	2.53	0.926	0.895
361B	1/4	Steel	70.0	1.46	3.20	0.916
439A	1/4	Bronze	181.8	2.71	9.23	0.940
437B	1/4	Aluminum	30.2	2.71	1.514	0.955
442A	1/4	Aluminum	9.01	1.66	0.449	0.986
443A	1/4	Aluminum	7.60	1.17	0.166	0.956
444A	1/4	Aluminum	7.60	1.07	0.142	0.789
434C	1/4	Aluminum	7.40	1.80	0.266	1.022
432	1/4	Aluminum	7.40	1.72	0.262	0.980
444B	1/4	Aluminum	7.00	0.82	0.114	0.632
491A	1/4	Aluminum	6.75	2.27	0.308	1.033
489C	1/4	Aluminum	6.70	3.00	0.405	1.003
490A	1/4	Aluminum	6.70	2.38	0.315	1.022

is proportional to the air density ρ and the sphere diameter d. The values of the coefficient of viscosity μ and of the speed of sound depend little on the air pressure, and their change with temperature is small in the firing range because of the approximate constancy of temperature. Hence, the Mach Number, M, is roughly proportional to the velocity, v, and the Reynolds Number is approximately proportional to the product $M\rho d$.

The lowest values of pressure used (about 1/120 atmosphere) were near the minimum easily attainable in the Pressurized Ballistics Range. Because of the small value of the drag force at such pressures, aluminum spheres were used to increase the deceleration. On the other hand, elevated pressures were avoided since above 1 atmosphere, even with steel spheres, the change of speed becomes so great that a simple dependence of C_D on Mach Number cannot be assumed throughout the speed range. The sphere diameter was varied between $^1/_4$ in. and $^3/_4$ in. only.

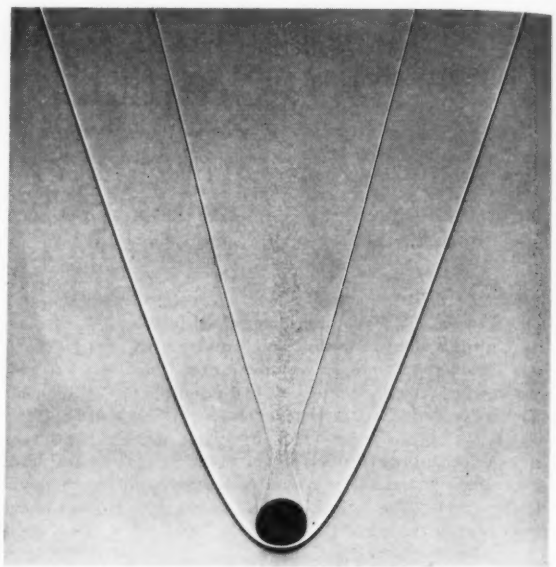

FIG. 3. Spark shadowgraph of a $^1/_2$-in. steel sphere traveling at $M = 3.48$, $Re = 8.45 \times 10^5$, in air at 0.85 atmosphere pressure.

Fig. 3 is a print obtained from a typical spark shadowgraph (round 441B; see Table 1) of this program. This round consisted of a $^1/_2$-in. steel sphere fired at $M = 3.48$ with an air pressure of 0.85 atmosphere. At lower pressures, the shock waves become less pronounced in the photograph, and at the lowest pressures used nothing is seen in the shadowgraphs but the sphere itself. Measurements for drag determinations are made at the rear of the sphere to avoid the optical distortion in front of it.

Spark shadowgraphs were taken only at the eight timing stations. Position-time data for determination of the drag coefficient were obtained by measurements of the sphere position (relative to a fiducial mark) on the photographic plates and from readings of the timing counters. From these data, values of C_D were calculated by a least-square technique.

PREVIOUS DRAG DETERMINATIONS

On the Mach Number-Reynolds Number coordinates of Fig. 4, the shaded areas indicate those regions in which reasonably reliable drag data for spheres were already available. Values of C_D for low Mach Numbers had been compiled by various authors[1, 2] for a wide range of Reynolds Numbers terminating just above the critical value. These are indicated by the shaded area immediately adjacent to the abscissa in Fig. 4.

The area that branches off from the one already described (near $Re = 4 \times 10^4$) was investigated by Charters and Thomas in the free-flight range at Aber-

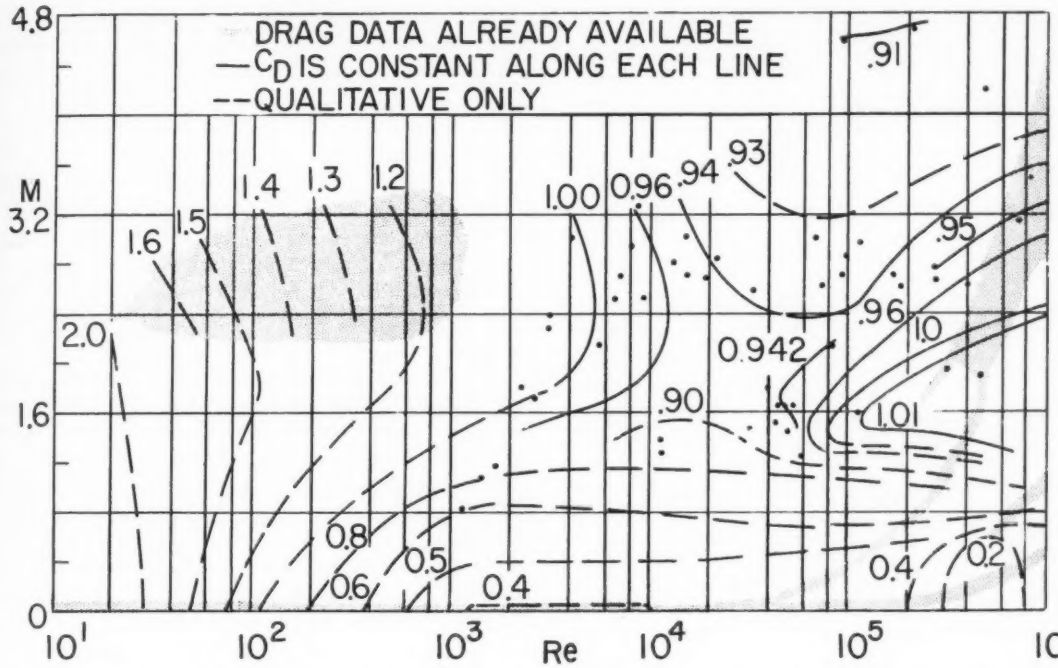

FIG. 4. Contour plot of C_D of spheres. The drag coefficient is constant along each line. Dashed lines are approximate only. Shaded areas are regions where reliable data were already available, and the dots show by their positions the Mach Numbers and Reynolds Numbers of the determinations made in the NOL Pressurized Ballistics Range.

deen, and their research is the subject of a comprehensive report.[3]

Other free-flight determinations at higher Mach Numbers and Reynolds Numbers were carried out at the New Mexico School of Mines[4] and in England.[5] Zahm[6] investigated a small transonic region at high Reynolds Numbers by free-flight tests. The large supersonic region indicated at small Reynolds Numbers was investigated in a wind tunnel at the University of California by Sherman and Kane[7] and by Jensen.[8]

Experimental Results

In the present program, 50 rounds were fired to provide C_D data. The Mach Numbers and Reynolds Numbers of these shots are indicated by the positions of the dots on Fig. 4. The experimental data for the rounds are given in Table 1.

The three-parameter data for these rounds (C_D, M, and Re) are represented in Fig. 4 by a contour plot using lines of constant C_D. These lines were determined by inserting on the M-Re coordinate axes the C_D values found in previous investigations and the 50 values found in the present study and by estimating the best lines of constant C_D. In some areas, too little data were available to permit dependable estimates, and the contours in these areas have been dashed to indicate that they are qualitative only. It will be seen that the variation of C_D is only about 10 per cent throughout the region in which $1.6 < M < 4.7$ and $4.0 \times 10^3 < Re < 1.0 \times 10^6$.

There appears to be unmistakable evidence of a saddle point in the vicinity of $M = 2.0$, $Re = 3 \times 10^4$. In passing along the line $Re = 3 \times 10^4$, a maximum is found near this point, while a minimum is encountered on the line $M = 2.0$.

No evidence was found of the existence of a critical Reynolds Number in that portion of the supersonic region investigated. Charters reported[3] that he found no critical Reynolds Number in a portion of this region. The curves of Fig. 4 indicate that over the range of Mach Number and Reynolds Number in that figure, any critical Reynolds Numbers are restricted to $M < 0.7$.

The drag data of Fig. 4 are presented in more familiar form in Figs. 5 and 6. Fig. 5 gives graphs of C_D against Re for various Mach Numbers. The lowest graph is the well-known plot[1, 2] for the incompressible case. Lack of data still permits only a guess as to the behavior immediately above this region. At Reynolds Numbers between 10^5 and 10^6, it is clear that C_D decreases as the Mach Number increases above about 1.6. From Fig. 4 it appears probable that such a decrease of C_D with increasing Mach Number may be expected at higher Mach Numbers throughout the Reynolds Number range from 10 to 10^6.

Fig. 6 gives graphs of C_D against Mach Number for several values of Reynolds Number. The similar graph given by Charters and Thomas[3] was obtained by firing spheres at various speeds using fixed air pressure and a diameter range of 5 to 1. Consequently, their plot is

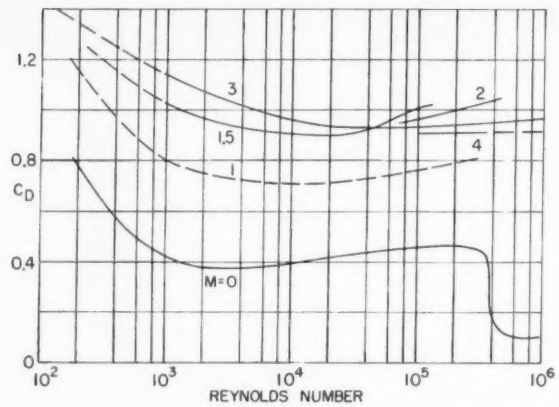

FIG. 5. Variation of C_D of spheres with Reynolds Number for various Mach Numbers. The dashed curve is only approximate.

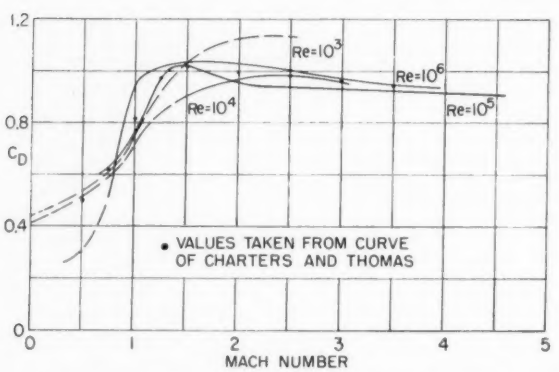

FIG. 6. Variation of C_D of spheres with Mach Number for several Reynolds Numbers. Dashed curves indicate that their positions are only approximate. The circles show values taken from a curve given by Charters and Thomas.[3]

an average over Reynolds Numbers varying by 5 to 1 for a given Mach Number. Values taken from Charters' curve are shown by the small circles superimposed on Fig. 6.

The accuracy of the drag-coefficient values is difficult to determine. Even the known sources of error vary greatly throughout the pressure and velocity ranges investigated and are difficult to appraise. At very low air pressures (6 to 7 mm.) accuracy was probably poorest because of errors in pressure measurement. For example, from a study of the consistency of readings made during calibration of the gage used for round 491B (pressure = 6.32 mm.), it appears that the drag coefficient for that round may be in error by as much as 2 per cent. For the $^3/_4$-in. spheres, known inaccuracies would not cause errors larger than 0.6 to 0.9 per cent.

The accuracy of the individual drag values is not easily estimated from a plot such as Fig. 4 since the placing of the contours depends on these values. Of the 50 values of C_D found, 36 appear to be in error by 1 per cent or less. Of the others, seven seem to have errors between 1 and 2 per cent, and seven to have errors greater than 2 per cent. In only one or two cases does it appear sure that the error is larger than 3 per cent.

Twenty values in the rather "flat" region between 0.03 and 0.95 contours (in general not shown) were averaged. The mean drag coefficient was 0.942, and the standard deviation was 0.010. It is thought that all contours shown by solid lines on Fig. 4 are accurate to 1 per cent and, in most regions, probably to $^1/_2$ per cent.

An attempt to correlate the angle at which the flow separates from the sphere with drag coefficient, as the Reynolds Number changes, was unsuccessful. This is not surprising in view of the small magnitude of the drag coefficient variations.

REFERENCES

[1] Goldstein, S., *Modern Developments in Fluid Dynamics*, 1st Ed., Vol. 1, p. 16; Oxford University Press, New York, 1938.

[2] Hoerner, S. F., *Aerodynamic Drag*, 1st Ed., p. 21; (published by the author) Midland Park, N.J., 1951.

[3] Charters, A. C., and Thomas, R. N., *The Aerodynamic Performance of Small Spheres from Subsonic to High Supersonic Velocities*, Journal of the Aeronautical Sciences, Vol. 12, No. 4, pp. 468–476, October, 1945.

[4] Hodges, A. J., *The Drag Coefficient of Very High Velocity Spheres*, NMSM/RDD/T-656, 1949.

[5] *The Retardation of Polished Steel Spheres Due to Air Resistance at Supersonic Velocities*, ARD Explosives Report 89/45, Ministry of Supply, 1945.

[6] Zahm, A. F., *Resistance of Air Below One Thousand Feet per Second*, Phil. Mag., 6S, Vol. 1, No. 5, pp. 530–535, May, 1901.

[7] Sherman, F. S., and Kane, E. D., *Supplementary Data on Sphere Drag Tests*, Technical Report HE-150-71, Institute of Engineering Research, University of California, 1950.

[8] Jensen, N. A., *Supplementary Data on Sphere Drag Tests*, Part 2, Technical Report HE-150-92, Institute of Engineering Research, University of California, 1951.

[9] Erdman, S., *Widerstandsbestimmung von Kegeln und Kugeln aus der Druckverteilung bei Ueberschallgeschwindigkeit*, Lilienthal Gesellschaft fuer Luftfahrtforschung, Bericht, 139, 1942.

Bending Tests of Thin-Walled Sandwich Cylinders*

GEORGE GERARD†
New York University

SUMMARY

A series of tests was conducted on thin-walled circular sandwich cylinders under bending loads using aluminum-alloy faces and either cellular cellulose acetate or end grain balsa cores. It was found that for cylinders with cellular cellulose acetate cores, the buckling strength averaged 32 per cent higher than the theoretical value. From previous tests under compressive loads, excellent agreement was obtained between the corresponding theoretical value and tests. Thus, it was concluded that, under bending loads, the buckling stress depends upon the average stress on the cross section rather than on the maximum stress. This behavior has been noted previously from tests on homogeneous cylinders.

INTRODUCTION

AS PART OF A PROGRAM involving a theoretical and experimental study of the buckling behavior of sandwich cylinders, this paper is concerned with buckling tests of thin-walled sandwich cylinders under bending loads. Tests were conducted on cylinders constructed with cores weak in shear (cellular cellulose acetate) and cores strong in shear (end grain balsa) to check the validity of a method for predicting overall buckling of sandwich cylinders under bending loads.

TEST PROGRAM

Test Specimens

The large number of variables which influences the behavior of a composite element such as sandwich construction requires that in a test program attention be directed toward the significant parameters only. Thus, in order to study the overall buckling characteristics of sandwich cylinders, it is necessary that the sandwich thickness be as small as possible. The $^1/_8$-in. thick sandwich used was considered to be the minimum thickness feasible. The nominal radius of 6 in. which was used for all cylinders was dictated by the capacity of the testing facilities. To ensure uniformity of introduction of bending load, the cylinders tested were 36 in. long.

The significant parameter in overall buckling of sandwich elements is the shear rigidity of the core material. Consequently, two different materials were selected for the core: cellular cellulose acetate (CCA) of approximately 6 lbs. per cu.ft. density and end grain balsa (EGB) of approximately 5 to 5.5 lbs. per cu.ft. density. For all cylinders, the face material used was 0.010-in. 24S-T3 aluminum alloy.

The cylinders used in this investigation were manufactured by Skydyne, Inc., of Port Jervis, N.Y. The fabrication details were briefly as follows. The aluminum-alloy faces were coated with a metal primer prior to assembly to the core. The core was planed to the proper thickness, and a secondary adhesive was used to bond the faces to the core. Although the adhesive used will polymerize at room temperature, sufficient heat was applied to accelerate setting of the adhesive. Pressure necessary to bring the surfaces in intimate contact was applied, and the assembly was molded for a period of 2 to 3 hours.

To facilitate installation of the test specimen in the loading jig, 2-in. wide hardwood blocks were bonded to both the inside and outside faces at each end of the cylinder (see Figs. 1 and 2). The end faces of these blocks were then turned down on a lathe to ensure planeness of the face, perpendicularity with the axis of the cylinder, and parallelism of the faces.

Test Procedure

The pertinent dimensions of each specimen were determined as follows. Four evenly spaced longitudinal stations were lightly scribed on the outside wall of the cylinder. The outside radius was then measured to the nearest 0.01 in. at each pair of stations at both ends.

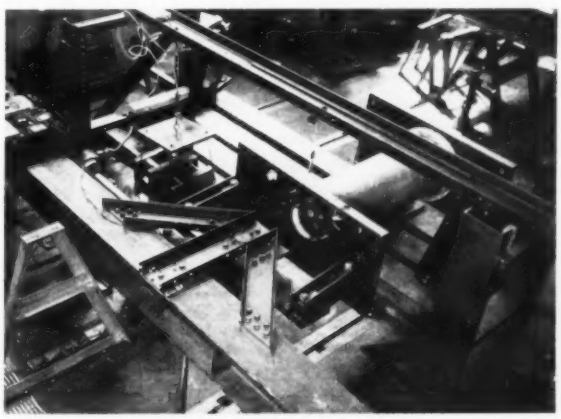

FIG. 1. Bending test setup.

Received December 12, 1952.

* Sponsored by the Office of Naval Research under Contract N6-onr-279, Task Order V.

† Assistant to the Director, Research Division, College of Engineering.

TABLE 1
Average Dimensions and Failing Loads of Sandwich Cylinders

Cylinder	Core Material	Length, In. L	Mean Radius, In. R	Total Thickness, In. $(h+t)$	Average Face Thickness, In. t	Failing Moment, In.Lbs. M_{cr}	Maximum Failing Load per In., Lbs. per Sq.In. $N_{cr} = M/\pi R^2$	Maximum Failing Stress, Lbs. per Sq.In. σ_{cr}
−1	CCA	32.09	6.48	0.141	0.0105	67,900	514	19,300
−2	CCA	32.13	6.50	0.125	0.0105	46,100	347	16,500
−3	CCA	32.13	6.49	0.125	0.0105	77,700	587	28,000
−4	CCA	32.16	6.53	0.141	0.0105	89,600	670	31,900
−5	EGB	31.29	6.47	0.141	0.0105	53,100	404	19,300
−6	EGB	31.09	6.55	0.156	0.0105	65,700	500	23,800

The length of the cylinder between hardwood blocks was also determined at each station to the nearest 0.01 in.

The total thickness of the cylinder wall was measured at each station at both ends just inside the hardwood blocks and at the center by means of a special dial gage with a least division of 0.001 in. The thickness of the faces was measured with a ten-thousandths micrometer on samples of the face material. The average dimensions for each cylinder are given in Table 1.

Installation of the specimens in the specially designed bending loading jig was accomplished by bolting the specimen to the steel end plates through the hardwood blocks at the ends of the cylinder. The loading jig is shown in Fig. 1 with a specimen installed and tested. Load was applied by means of a hydraulic tension jack and was measured by a calibrated strain-gage tension link at the jack which was accurate to ±2 per cent.

Physical Property Tests

The important physical properties in overall bending buckling of sandwich construction are the compressive stress-strain characteristics of the face material and the shear modulus of the core material. The shear moduli of the core materials were determined by testing as simple beams, strips of flat sandwich construction. The beams were fabricated by the manufacturer of the cylinders of the same materials and in the same manner as the cylinders themselves. The test consisted of obtaining load-deflection data from which the shear modulus of the core material was determined from the difference in deflection between the experimental value and that computed for the beam neglecting shear deflections. From at least four tests of each core material, the following values of shear modulus were obtained:

cellular cellulose acetate; $\bar{G}$ = 3,400 lbs. per sq.in. ± 17 per cent

end grain balsa; $\bar{G}$ = 17,600 lbs. per sq.in. ± 15 per cent

The with-grain compressive stress-strain characteristics of the 0.010-in. 24S–T3 aluminum alloy used for the faces of the sandwich cylinders was determined by use of a solid guide compression jig of the National Bureau of Standards type. The stress-strain data indicated that the proportional limit of this material was 34,000 lbs. per sq.in. Thus, the stress in the faces at failure of the sandwich cylinders (Table 1) was within the elastic range in all cases.

TABLE 2
Data on Instability Patterns

Cylinder	Type of Instability	Location	Longitudinal Wave Length, In., L_x	Circumferential Wave Length, In., L_θ
−1 1/8 in. CCA	Buckle	Central	1	3
−2 1/8 in. CCA	Buckle	Central	1	3
−3 1/8 in. CCA	Buckle	Central	1 1/4	3 1/2
−4 1/8 in. CCA	Antisymmetrical wrinkle	Both ends	7/16	πR
−5 1/8 in. EGB	Buckle	Central	1 1/4	3 1/2
−6 1/8 in. EGB	Antisymmetrical wrinkle	At end	7/16	πR

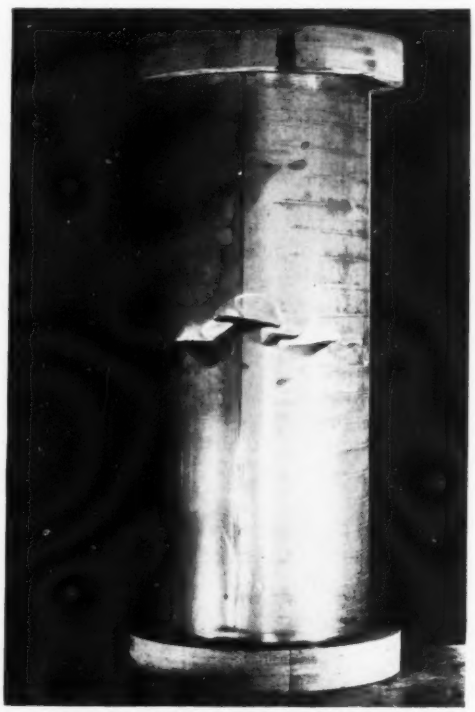

FIG. 2. Overall buckling of sandwich cylinder in bending.

Test Results

Average measured dimensions of the sandwich cylinders together with the failing loads are given in Table 1. A photograph of a typical buckle pattern taken after the conclusion of the test is shown in Fig. 2. Additional data on the buckling and wrinkling patterns are given in Table 2. The measured wave lengths were obtained in regions of relatively little distortion.

Correlation of Theory with Experimental Data

Theoretical work on buckling of a sandwich cylinder under bending loads is given in reference 1 for the case where the core is weak in shear. The results of this analysis indicate that for this case, the buckling load, N_{cr}, is equal to the shear rigidity of the core $\bar{h}\,\bar{G}$.

The $^1/_8$-in. CCA cylinders fall into this category, and, therefore, it is possible to check the theoretical work of reference 1 directly. The average centroidal height, $\bar{h}$, of cylinders -1 to -4 is 0.118 ± 6 per cent, and the average shear modulus is 3,400 lbs. per sq.in. ± 17 per cent. Therefore, the average shear rigidity of this group of cylinders is 400 lbs. per in. ± 23 per cent, which according to reference 1 is the theoretical buckling loading. The average experimental failing loading was found to be 530 lbs. per in. ± 33 per cent. Thus, the experimental failing loading is 32 per cent higher than the theoretical value, on the average.

In reference 2, comparable tests were run on sandwhich cylinders under axial compressive loads. The theory of reference 2 indicated that the buckling loading of cylinders weak in shear is also equal to the shear rigidity of the core. For an average $\bar{h} = 0.115$ in. ± 7 per cent and an average shear modulus $\bar{G} = 2{,}000$ lbs. per sq.in. ± 20 per cent, the average shear rigidity was 230 lbs. per in. ± 27 per cent. The average experimental failing load of eleven $^1/_8$-in. CCA sandwich cylinders given in reference 2 was 235 lbs. per in. ± 50 per cent. Thus, the experimental failing load was approximately 2 per cent higher than the theoretical value, on the average, indicating excellent agreement.

The fact that the bending buckling load is higher than the compressive buckling load for cylinders of the same dimensions has been observed in tests on homogeneous cylinders in reference 3. It has been suggested that this behavior may be due to the buckling phenomena responding to the average value of compressive stress on the cross section rather than the maximum stress. In the case of pure bending, the maximum stress would be 1.4 times as great as the average value.

For sandwich cylinders in compression, the theory of reference 2 indicates that value of the parameter Et/GR governs the behavior of the cylinder. Thus, it has been found that cylinders can be considered weak in shear when the value of $ET/\bar{G}R$ exceeds unity. To effect a comparison between the cylinders loaded in compression and bending which were differently constructed as concerns $\bar{G}$ and R, it appears that, if the values of $Et/\bar{G}R$ were equal or at least greater than unity for each group, a direct comparison would be valid.

The value of this parameter for the compression specimens averaged 5, and for the bending specimens $Et/\bar{G}R = 5$ also. Thus, since the compressive test data check theory well, it can be concluded that in bending the 32 per cent higher experimental value is in agreement with the behavior observed for homogeneous cylinders, thus accounting for the discrepancy.

Although these conclusions are based on data with which large percentage variations are associated, it appears that the trend is clearly indicated. The fact that the scatter of the experimental values is considerably higher than that for the core properties is based on the fact that the latter values were established from beam bending tests. In a beam test, the results are a statistical average of the core properties, whereas a structure subject to buckling responds to local weak spots caused by defects in the core properties. Thus, the scatter would tend to be greater for the buckling data.

The $^1/_8$-in. end grain balsa cylinders, -5 and -6, can be considered to be in the weak-in-shear category, since, for this group, $Et/\bar{G}R = 1.4$. These cylinders, therefore, failed at a small fraction of the theoretical load. This is evidenced by the fact that the average failing loading of this group was 452 lbs. per in. as compared to 530 lbs. per in. for the $^1/_8$-in. CCA cylinders, although the shear modulus of the EGB core was over five times as great as the CCA core. The fact that the EGB cylinders were not even as strong as the CCA cylinders is difficult to reconcile with the core properties. Unless some other mode of buckling is responsible for this anomalous behavior, it appears that poor bonding to the EGB core may be responsible for the low values of failing load.

References

[1] Wang, C. T., and Sullivan, D. F., *Buckling of Sandwich Cylinders Under Bending and Combined Bending and Axial Compression*, Journal of the Aeronautical Sciences, Vol. 19, No. 7, pp. 468–470, 485, July, 1952.

[2] Teichmann, F. K., Wang, C. T., and Gerard, G., *Buckling of Sandwich Cylinders Under Axial Compression*, Journal of the Aeronautical Sciences, Vol. 18, No. 6, pp. 338–406, June, 1951.

[3] Donnell, L. H., *A New Theory for the Buckling of Thin Cylinders Under Axial Compression and Bending*, Trans., ASME, Vol. 56, No. 11, pp. 795–806, November, 1934.

Readers' Forum

BRIEF REPORTS of investigations in the aeronautical sciences and discussions of papers published in the JOURNAL are presented in this special department. Publication will be completed as soon as possible after receipt of the material. The Editorial Committee does not hold itself responsible for the opinions expressed by the correspondents. Contributions should not exceed 800 words in length.

Minimum Drag Cambered Rectangular Wing for Supersonic Speeds

N. Rott
Cornell University, Ithaca, N.Y.
May 12, 1953

FROM THE PRESSURE DISTRIBUTION on a thin rectangular wing in supersonic flow at a constant angle of attack α (originally given by Busemann), it may be derived immediately that the lift dL of a spanwise strip (with span b and width dx) at the chordwise station x is

$$dL = 2\beta\rho U^2\alpha(b - \beta x)\,dx \tag{1}$$

where

$$\beta = (M^2 - 1)^{-1/2}$$

In other words, the chordwise lift distribution decreases linearly from the Ackeret value, which is found at the leading edge, $x = 0$. The formula is valid beyond the intersection of the two wing-tip Mach cones, but it is limited to chordwise stations ahead of the intersection of the wing-tip Mach cone with the opposite side-edge. Thus, the chord c can be at most b/β.

With the same restriction, the lift for a cambered rectangular wing can be given. Let α be now a function of x. At a chordwise station x_1, the change in α over a length dx_1 is $d\alpha = \alpha'(x_1)dx_1$. The contribution of this *change* in α to the lift at a station $x > x_1$ can be expressed by taking a rectangular wing with leading edge at x_1 and a constant angle of attack $d\alpha = \alpha'(x_1)dx_1$:

$$d(dL) = 2\beta\rho U^2\alpha'(x_1)dx_1[b - \beta(x - x_1)]dx$$

Superimposing these contributions, dL at the station x becomes the Duhamel integral computed with this integrand, leading to the expression

$$\begin{aligned} dL &= 2\beta\rho U^2\alpha(0)(b - \beta x)dx + \int_{x_1 = 0}^{x} d(dL) \\ &= 2\beta\rho U^2[b\alpha(x) - \beta\int_0^x \alpha(x_1)\,dx_1]\,dx \end{aligned} \tag{2}$$

The contribution of the same strip to the drag D is given by

$$dD = \alpha(x)dL \tag{3}$$

Put

$$\alpha(x) = dz_0/dx \tag{4}$$

where z_0 is the wing ordinate (positive downward.) Let $z_0 = 0$ at the leading edge $x = 0$. Introducing the nondimensional quantities

$$\zeta = z_0/c, \qquad \xi = x/c$$

the following expressions are obtained for the lift and drag coefficients:

$$C_L = 4\beta\left(\zeta(1) - \frac{1}{\Lambda}\int_0^1 \zeta\,d\xi\right) \tag{5}$$

$$C_D = 4\beta\left[\int_0^1 \zeta'^2 d\xi - \frac{1}{2\Lambda}\zeta^2(1)\right] \tag{6}$$

where

$$\Lambda = b/\beta c$$

is the "reduced" aspect ratio ≥ 1.

The present note is concerned with the determination of a camber $\zeta(\xi)$, which renders the drag due to lift a minimum. (In linearized theory this drag is independent of thickness drag.) Because of the assumption of no twist, the minimum is only a restricted one.

The question is: What function $\zeta(\xi)$ renders C_D a minimum, for fixed C_L? First, let $\zeta(1)$ be constant; a simple problem of the calculus of variation results which leads to the solution $\zeta'' =$ constant, or a parabola,

$$\zeta = a_0 + a_1\xi + a_2\xi^2$$

With this result in mind, put

$$\zeta = \alpha_0\xi - (\Delta z_0/c)4\xi(1 - \xi) \tag{7}$$

where $|\Delta z_0|$ is the maximum ordinate for $\alpha_0 = 0$. Introduced in Eq. (5) and (6), this leads to the result

$$C_L = 4\beta\left(\alpha_0 - \frac{1}{2\Lambda}\alpha_0 + \frac{2}{3\Lambda}\frac{\Delta z_0}{c}\right) \tag{8}$$

$$C_D = 4\beta\left[\alpha_0^2 - \frac{1}{2\Lambda}\alpha_0^2 + \frac{16}{3}\left(\frac{\Delta z_0}{c}\right)^2\right] \tag{9}$$

The effect of camber becomes evident in these formulas. A positive camber reduces the lift loss in the domain of the wing-tip Mach cones and thus increases C_L, but it also increases C_D on the whole wing. A gain in C_D at constant C_L is possible. Evaluating the optimal conditions by elementary means, it follows that $C_{Dmin.}$ will be found for a camber

$$\Delta z_0/c = \alpha_0/8\Lambda \tag{10}$$

and that the gain over the flat plate (for the same lift) is

$$\frac{C_{DFP} - C_{D_{min.}}}{C_{DFP}} = \frac{1}{12\Lambda^2 - 6\Lambda + 1} \tag{11}$$

The biggest gain is naturally expected at the lowest aspect ratios; taking $\Lambda = 1$, which is the limit of the present theory, the gain is 14.3 per cent. For $\Lambda = 2$, the gain is only 2.7 per cent.

The chordwise lift distribution for optimal conditions is symmetrical about the mid-chord,

$$\frac{dC_L}{d\xi} = 4\beta\alpha_0\left[1 - \frac{1}{2\Lambda} + \frac{1}{2\Lambda^2}\xi(1 - \xi)\right] \tag{12}$$

The results of this calculation are in excellent agreement with results of an approximate minimizing procedure given by Graham.[1] The present example illustrates also the well-understandable general conclusion of Graham—namely, that camber yields only small reductions of the drag due to lift for higher aspect ratio supersonic wings.

Reference

[1] Graham, E. W., *A Drag Reduction Method for Wings of Fixed Plan Form*, Journal of the Aeronautical Sciences, Vol. 19, No. 12, pp. 823–825, December, 1952.

On Asymptotic Solutions for the Heat Transfer at Varying Wall Temperatures in a Laminar Boundary Layer with Hartree's Velocity Profiles*

Arthur N. Tifford and Sheng To Chu
The Ohio State University, Columbus Ohio
May 22, 1953

SCHUH IN A READERS' FORUM NOTE of the same title[1] presents an independent derivation of the asymptotic solution described in reference 2 and given in greater detail in reference 3. There are some "fine" differences between the two analyses, however, which lead to different evaluations of the "inherent" error. For that reason we reproduce some of our findings.

The differential equation under consideration is

$$Y_{\bar{n}}'' + \sigma \bar{f} Y_{\bar{n}}' - \sigma \bar{n}(2 - \beta) \bar{f}' Y_{\bar{n}} = 0 \qquad (1)$$

with the boundary conditions, $Y_{\bar{n}}(0) = 1$ and $Y_{\bar{n}}(\infty) = 0$, where

$\bar{f}'$ = Hartree's velocity function
$\bar{n}$ = exponent in the surface temperature representation $T_w - T_a = \sum b_{\bar{n}} x^{\bar{n}}$
T_a = temperature acquired by the surface when insulated
T_w = wall temperature
$Y_{\bar{n}}$ = thermal functions in the solution, $T = T_t + (u_1^2/gc_pJ)\,\Psi + \Sigma b_{\bar{n}} Y_{\bar{n}} x^{\bar{n}}$
β = pressure gradient parameter, $2m/(m + 1)$
$\bar{\eta}$ = independent variable, $\{[(m + 1)/2](u_1/x\nu)\}^{1/2} y$
σ = Prandtl Number

We note that the second term, $\sigma \bar{f} Y_{\bar{n}}'$, is of the same order of magnitude as the portion of the third term, $\sigma \bar{f}' Y_{\bar{n}}$. Therefore, when $\bar{n}(2 - \beta) \gg 1$—which is equivalent to $\bar{n} \gg 1$—the second term is negligible as compared with the third term. Now the effect of the value of $\bar{n}$ on the thermal boundary-layer function, $Y_{\bar{n}}$, is exactly the same as that of the Prandtl Number, σ. Just as for large Prandtl Numbers, the thermal boundary layer for large values of $\bar{n}$ is thin as compared with the velocity boundary layer. Consequently, the velocity profile, u/u_1, may be represented by the first few terms of the Taylor series,

$$u/u_1 = \bar{f}' = a_2 \bar{\eta} + (a_2/2!)\bar{\eta}^2 + \ldots$$

where $a_n = \bar{f}^n(0)$. (Note that the coefficients, a_0, a_1, and a_4, of the complete Taylor Series are zero for all laminar boundary layers on impervious surfaces.)

When $\bar{n}$ is extremely large, the first term, $a_2\bar{\eta}$, provides an adequate velocity profile representation for a nonseparating boundary layer. Under these circumstances, Eq. (1) reduces to

$$Y^{(2)} - \tilde{\eta} Y = 0 \qquad (2)$$

where $\tilde{\eta} = N\bar{\eta}$, $N = [\sigma(2 - \beta)a_2 n]^{1/3}$, and the superscript (i) denotes the ith order of differentiation with respect to $\tilde{\eta}$.

The solution satisfying the boundary conditions, $Y(0) = 1$ and $Y(\infty) = 0$, is

$$Y = \left[4\Gamma\left(\frac{11}{16}\right) \Big/ 5\Gamma\left(\frac{5}{3}\right)\right]\left(\frac{4}{3}\right)^{1/3} (\eta/\pi)^{1/2}[K_{1/3}(2\tilde{\eta}^{3/2}/3)]$$

or

$$Y = 0.5176\tilde{\eta}^{1/2}[K_{1/3}(2\tilde{\eta}^{3/2}/3)]$$

where $K_{1/3}$ is the modified Bessel function of the second kind of one-third order (see reference 4).

At the time of our original analysis (1950) Dr. K. Pohlhausen, of the Aerodynamic Research Laboratory, USAF, suggested the investigation of a perturbative improvement upon the asymptotic solution. Such an improvement was developed. However, a more rigorous treatment was found to result from the use of an asymptotic series expansion for the function, $Y_{\bar{n}}$. The latter treatment is given below.

Let the asymptotic series expansion for $Y_{\bar{n}}$ be

$$Y_{\bar{n}} = Y + \frac{1}{N} y_1 + \frac{1}{N^2} y_2 + \frac{1}{N^3} y_3 + \ldots$$

Substituting this series and the Taylor series expressions for $\bar{f}$ and $\bar{f}'$ into Eq. (1), we obtain

$$\left(Y^{(2)} + \frac{1}{N} y_1^{(2)} + \frac{1}{N^2} y_2^{(2)} + \ldots\right) + \sigma\left(\frac{a_2}{2!N^2}\bar{\eta}^2 + \frac{a_3}{3!N^4}\bar{\eta}^3 + \ldots\right)\left(Y^{(1)} + \frac{1}{N} y_1^{(1)} + \ldots\right) - \frac{1}{a_2}\left(a_2\bar{\eta} + \frac{a_3}{2!N}\bar{\eta}^2 + \ldots\right)\left(Y + \frac{1}{N} y_1 + \ldots\right) = 0 \qquad (3)$$

the independent variable having been changed throughout to $\tilde{\eta}$.

Collecting terms of the same power of N, the following system of equations is obtained:

$$y_s^{(2)} - \tilde{\eta} y_s = \sum_{j=0}^{(s-1)} C_i \tilde{\eta}^i y_j - \sum_{q=0}^{(s-3)} d_k \tilde{\eta}^k y_q^{(1)} \qquad (4)$$

where all the subscripts are positive integers, and

* Research supported by the Aerodynamic Research Laboratory, USAF.

TABLE 1
Values of $(D_{\tilde{\eta}} Y_{\bar{n}})_0$ for a Flat Plate
$\sigma = 0.72$

n	Asymptotic Result $(D_{\tilde{\eta}} Y)_0$	$(D_{\tilde{\eta}} Y)_0 + \frac{(D_{\tilde{\eta}} y_3)_0}{N^3}$	$(D_{\tilde{\eta}} Y)_0 + \frac{(D_{\tilde{\eta}} y_3)_0}{N^3} + \frac{(D_{\tilde{\eta}} y_4)_0}{N^4}$	$(D_{\tilde{\eta}} Y)_0 + \frac{(D_{\tilde{\eta}} y_3)_0}{N^3} + \frac{(D_{\tilde{\eta}} y_4)_0}{N^4} + \frac{(D_{\tilde{\eta}} y_5)_0}{N^5}$	"Exact" Values: Analog	"Exact" Values: Reference 5
10	−1.378	−1.404	−1.405	−1.405	−1.384	−1.423
5	−1.094	−1.135	−1.137	−1.136	−1.106	−1.130
4	−1.016	−1.063	−1.065	−1.065	−1.031	−1.053
3	−0.923	−0.980	−0.984	−0.983	−0.942	−0.967
2	−0.806	−0.881	−0.889	−0.886	−0.832	−0.845
1	−0.640	−0.759	−0.785	−0.762	−0.682	−0.691

$$i = (s - j + 1), \qquad k = (s - q - 1)$$

$$C_i = \frac{a_{i+1}}{a_2(i!)}, \qquad d_k = \frac{\sigma a_k}{(k!)}, \qquad y_0 = Y$$

The first equation in Eqs. (4)—i.e. $s = 0$—is identically the asymptotic equation, Eq. (2), obtained previously. The remaining equations have the common formulation

$$y_s^{(2)} - \bar{\eta} y_s = F_s[\bar{\eta};\ y_{s-1},\ y_{s-2},\ \ldots\ y_0;\ y_{s-3}^{(1)},\ y_{s-4}^{(1)},\ \ldots\ y_0^{(1)}]$$

They can be solved analytically in succession.

The solution for the case of the flat plate has been worked out in detail for $\sigma = 0.72$. This case is particularly simple numerically because in addition to a_0, a_1, and a_4, the coefficients a_7, a_8, a_7, a_9, a_{10}, etc., are also zero. The resulting values of $(D_{\bar{\eta}} Y_{\bar{n}})_0$ are given in Table 1. The corresponding "exact" values obtained on the REAC analog computers at Wright Field and obtained by Chapman and Rubesin in reference 5 are listed for comparison.

The original asymptotic analysis contains two different sources of error for applications at finite values of $\bar{n}$—namely, (1) the assumption that the second term of the differential equation has a relatively small influence on the solution, and (2) the additional assumption that the velocity profile may be adequately represented by the first term of a Taylor series. It is clear that the error due to (1) is independent of the Prandtl Number and depends only on the value of $\bar{n}(2 - \beta)$ as compared with unity. Errors due to (2), on the other hand, depend on both the value of $\bar{n}$ and the Prandtl Number. Although the improvement obtained by means of the asymptotic series approach tends to decrease both types of error, it inherently cannot fully eliminate the error arising from the first assumption. In other words, at large values of $\bar{n}(2 - \beta)$ the complete treatment is essentially exact; at smaller values of this parameter—e.g., values smaller than 10—even the improved analysis cannot fully compensate for the inherent error in the original asymptotic approach.

Addendum

The May, 1953, issue of the JOURNAL OF THE AERONAUTICAL SCIENCES containing the criticism by Tribus[6] of Schuh's Readers' Forum note has just reached us. We offer the following comment:

It is true that the results of Lighthill[7] are somewhat more general than those given by Schuh. Nevertheless, the implication that the asymptotic analysis is therefore hardly worthy of mention is not justified. Despite appearances, *the asymptotic analysis does not cover the same ground as did Lighthill.*

In addition to offering an independent evaluation of the surface rate of heat transfer, the asymptotic analysis contributes the following:

(a) A derivation showing explicitly that the surface rate of heat transfer varies as $\bar{n}^{1/3}$ at large values of $\bar{n}$. (Although Lighthill's analysis may be developed further so as to affirm this, the published analysis does not contain such an analytic finding.)

(b) A novel application of "order-of-magnitude" analysis.

(c) An analytic specification of the temperature profile within the boundary layer at large values of $\bar{n}$ (see references 2 and 3).

Furthermore, the asymptotic analysis is more readily subject to *analytic* improvement through the use of a more correct specification of the boundary-layer velocity profile (see asymptotic series solution given above). Such an improvement should prove particularly significant when strong surface pressure gradients—especially adverse ones—are present.

As a final remark, we bring to the reader's attention the improvement upon Lighthill's analysis given in reference 8.

References

[1] Schuh, H., *On Asymptotic Solutions for the Heat Transfer at Varying Wall Temperatures in a Laminar Boundary Layer with Hartree's Velocity Profiles*, Readers' Forum, Journal of the Aeronautical Sciences, Vol. 20, No. 2, pp 146–147, February, 1953.

[2] Tifford, A. N., and Chu, S. T., *On Heat Transfer, Recovery Factors, and Spin for Laminar Flows*, Readers' Forum, Journal of the Aeronautical Sciences, Vol. 19, No. 11, pp. 787–789, November, 1952.

[3] Tifford, A. N., and Chu, S. T., *Heat Transfer in Laminar Boundary Layers Subject to Surface Pressure and Temperature Distributions*, Proceedings of the Second Midwestern Conference on Fluid Mechanics, pp. 363–377, September, 1952.

[4] McLachlan, N. W., *Bessel Functions for Engineers*, Chapter VII; Oxford University Press, 1941.

[5] Chapman, D. R., and Rubesin, M. W., *Temperature and Velocity Profiles in the Compressible Laminar Boundary Layer with Arbitrary Distribution of Surface Temperature*, Journal of the Aeronautical Sciences, Vol. 16, No. 9, pp. 547–565, September, 1949.

[6] Tribus, M., *Theory of Heat Transfer Through a Laminar Boundary Layer*, Readers' Forum, Journal of the Aeronautical Sciences, Vol. 20, No. 5, p. 366, May, 1953.

[7] Lighthill, M. J., *Contributions to the Theory of Heat Transfer Through a Laminar Boundary Layer*, Proceedings of The Royal Society, Series A, Vol. 202, No. 1070, pp. 359–377, August, 1950.

[8] Tifford, A. N., *On the Theory of Heat Transfer Through a Laminar Boundary Layer*, Readers' Forum, Journal of the Aeronautical Sciences, Vol. 18, No. 4, pp. 283–284, April, 1951.

On the Behavior of a Sharp Leading Edge

Y. C. Fung

California Institute of Technology, Pasadena, California

May 21, 1953

BIOT[1] SHOWS THAT in a supersonic flow an airfoil having a sharp leading edge is unstable chordwise, in the sense that the leading edge will curl up. The supersonic part of the argument is unessential, the sharp leading edge will also curl up in a subsonic flow. It appears that the idealization of a sharp leading edge is unsatisfactory as a model for aeroelastic analyses. As the concept of sharp leading edge is prevailing in aerodynamics, it may be worth while to point out the elastic behavior of such an edge; it is important in comparing aerodynamic theory and experiments that require an aeroelastic model.

Consider a two-dimensional wedge of perfectly elastic material, as shown in Fig. 1. If one side of the wedge ($\theta = 0$) is loaded by a normal pressure distribution

$$p(r) = Pr^m \tag{1}$$

while the other side ($\theta = \alpha$) is stress-free, the Airy stress function $\phi(r, \theta)$ can be expressed in the following form:

(1) If $m \neq 0$,

$$\phi = r^{m+2}\,[a \cos(m + 2)\theta + b \sin(m + 2)\theta + c \cos m\theta + d \sin m\theta] \tag{2}$$

where

$$a = -Km\,[m + 2 - \cos 2(m + 1)\alpha - (m + 1)\cos 2\alpha]/2\Delta$$
$$b = Km\,[\sin 2(m + 1)\alpha + (m + 1)\sin 2\alpha]/2\Delta$$
$$c = K - a, \qquad d = -(m + 2)c/m$$

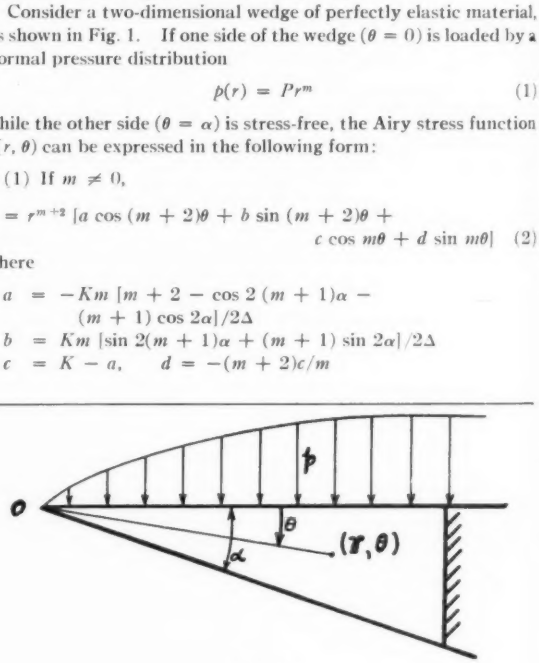

FIG. 1.

$$\Delta = -m(m+2) - \cos 2(m+1)\alpha + (m+1)^2 \cos 2\alpha$$
$$K = P/(m+1)(m+2)$$

(2) If $m = 0$,

$$\phi = Pr^2 [-\tan\alpha \cos^2\theta + (1/2)\sin 2\theta + \alpha - \theta]/2(\alpha - \tan\alpha) \quad (3)$$

where r, θ are polar coordinates and α is the wedge angle. $m = 0$ corresponds to a uniform pressure on the wedge; $m = 1$, a linear pressure distribution that decreases to zero at the leading edge. Eq. (2) is a simple generalization of a result given by Levy;[2] it is valid for real or complex values of m for which $\Delta \neq 0$.

The elastic behavior of the wedge at the leading edge, given by the limiting case $r \to 0$, is as follows, where $\sigma_\theta, \sigma_r, \tau_{r\theta}$ denote the normal and shearing stresses and u, v the components of displacement in the direction of increasing r and θ, respectively:

(a) $\sigma_r, \sigma_\theta, \tau_{r\theta}$ tend to zero if $m > 0$; tend to a finite value if $m = 0$; and tend to infinity if $m < 0$.

(b) The slope $\partial v/\partial r$ is finite if $m > 0$; it tends to infinity if $m \leq 0$.

(c) The curvature $\partial^2 v/\partial r^2$ is finite if $m \geq 1$, but tends to infinity if $m < 1$.

Note that the conclusions (b) and (c) agree with those of simple beam formulas, by considering the wedge as a beam of variable cross section. Hence, the above more elaborate analysis shows that, for small α, the beam formulas are justified either when the tip of the wedge is sharp or is cut off.

For example, in a subsonic flow the leading edge is a stagnation point, but small changes in local slope do not strongly change the pressure distribution. Hence, one may take $m \leqq 0$, and it is seen that an accidental disturbance will cause a sharp leading edge to curl up.

References

[1] Biot, M. A., *Aeroelastic Stability of Supersonic Wings—Chordwise Divergence*, Cornell Aero. Lab. Report, CAL-1-E-1, CM-427, December 8, 1947.

[2] See Southwell, R. V., *Theory of Elasticity*, p. 381; Oxford, 1941; or Timoshenko, S., *Theory of Elasticity*, p. 122, McGraw-Hill Book Company, Inc., New York, 1934.

The Effect of Dissociation in the Stagnation Region of a Blunt-Nosed Body

Ivan E. Beckwith

Langley Aeronautical Laboratory, NACA, Langley Field, Va.

May 21, 1953

In a recent paper by Moore,[1] the laminar boundary-layer characteristics with equilibrium dissociation were computed for a flat plate. An interesting conclusion obtained was that the heat-transfer rate per unit area is essentially unaffected by dissociation when the plate temperature is below 2,500°R. The question naturally arises as to whether the same conclusion can be made concerning the heat transfer in the stagnation region of a blunt-nosed body.

The purpose of this note is to discuss an approximate method for the calculation of the heat transfer on an arbitrary two-dimensional body in the presence of equilibrium dissociation. As a numerical example, the heat transfer is computed in the stagnation region of a blunt-nosed body.

The method used is similar to that of Kalikhman,[2] except for some details that have been modified so as to include dissociation. The boundary-layer equations are written as follows:

Momentum,

$$\left.\begin{aligned} \rho u \frac{\partial u}{\partial x} + \rho v \frac{\partial u}{\partial y} &= -\frac{\partial p}{\partial x} + \frac{\partial}{\partial y}\left(\mu \frac{\partial u}{\partial y}\right) \\ 0 &= \partial p/\partial y \end{aligned}\right\} \quad (1)$$

Continuity,

$$(\partial/\partial x)(\rho u) + (\partial/\partial y)(\rho v) = 0 \quad (2)$$

Energy,

$$\rho u \frac{\partial H}{\partial x} + \rho v \frac{\partial H}{\partial y} = \frac{\partial}{\partial y}\left(\mu \frac{\partial H}{\partial y}\right) + \frac{\partial}{\partial y}\left[\mu \frac{\partial h}{\partial y}\left(\frac{1}{\sigma} - 1\right)\right] \quad (3)$$

where $H = h + (u^2/2)$ is the stagnation enthalpy, h is the static enthalpy, and $\sigma = (\mu/k)(dh/dT)$ is the Prandtl Number.

Integration of Eqs. (1) and (3) across the boundary layer and the use of Eq. (2) result in

$$\frac{d}{dx}\int_0^\infty \left(\frac{u}{u_1} - \frac{u^2}{u_1^2}\right)d\eta + \left[2\int_0^\infty \left(\frac{u}{u_1} - \frac{u^2}{u_1^2}\right)d\eta + \int_0^\infty \left(\frac{\rho_1}{\rho} - \frac{u}{u_1}\right)d\eta\right]\frac{1}{u_1}\frac{du_1}{dx} = \frac{\mu_w \rho_w}{u_1 \rho_1^{*2}}\left[\frac{\partial}{\partial\eta}\left(\frac{u}{u_1}\right)\right]_w \quad (4)$$

$$\frac{d}{dx}\int_0^\infty \frac{u}{u_1}\left(1 - \frac{t^*}{t_1^*}\right)d\eta + \left[\frac{1}{u_1}\frac{du_1}{dx} - \frac{1}{t_1^*}\frac{dh_w}{dx}\right]\int_0^\infty \frac{u}{u_1} \times \left(1 - \frac{t^*}{t_1^*}\right)d\eta = \frac{\mu_w \rho_w}{\sigma_w \rho_1^{*2} u_1}\left[\frac{\partial}{\partial\eta}\left(\frac{t^*}{t_1^*}\right)\right]_w \quad (5)$$

where η is the Dorodnitsyn variable

$$\eta = \int_0^y \frac{\rho}{\rho_1^*}\, dy \quad (6)$$

ρ^* is the stagnation density, $t^* = H - h_w$ is the difference between the local stagnation enthalpy and wall enthalpy, and subscripts 1 and w refer to local free-stream values (behind the bow shock) and wall values, respectively.

The usual fourth-degree polynomial is used for the velocity

$$\frac{u}{u_1} = \frac{12+\lambda}{6}\eta^* - \frac{\lambda}{2}\eta^{*2} + \frac{3\lambda - 12}{6}\eta^{*3} + \frac{6-\lambda}{6}\eta^{*4} \quad (7)$$

where $\eta^* = \eta/\Delta$ (Δ is the nominal velocity boundary-layer thickness) and

$$\lambda = \frac{\rho_1}{\mu_w}\left(\frac{\rho_1^*}{\rho_w}\right)^2 \frac{du_1}{dx}\Delta^2 \quad (8)$$

Eq. (8) satisfies Eq. (1) evaluated at the wall with the restriction that $T_w < 2{,}500$°R., allowing the additional assumptions that, in the immediate vicinity of the wall,

$$\mu = (\mu_w/T_w)T \quad (9)$$

$$\rho = \rho_w T_w (1/T) \quad (10)$$

i.e., the wall temperature is always less than the dissociation temperature so that the conventional perfect gas assumptions can be used here.

The stagnation enthalpy profile is also taken as a fourth-degree polynomial in η^*

$$\frac{t^*}{t_1^*} = B_1\eta^* + B_2\eta^{*2} + (4 - 3B_1 - 2B_2)\eta^{*3} + (2B_1 + B_2 - 3)\eta^{*4} \quad (11)$$

where

$$B_2 = (1 - \sigma_w)\frac{u_1^2}{2t_1^*}\left(\frac{12+\lambda}{6}\right)^2 \quad (12)$$

which satisfies Eq. (3) evaluated at the wall. The assumption used in Eqs. (11) and (12) is that the thermal or enthalpy boundary-layer thickness is equal to the velocity boundary layer thickness Δ. Calculations made for a perfect gas indicate that this assumption gives results in close agreement with the exact computations of Brown and Donoughe,[3] as long as the ratio of the

surface temperature to stream temperature is less than about 0.7. Thus, instead of using the ratio of thermal to velocity boundary-layer thickness and λ as the unknowns in the solution of Eqs. (4) and (5) as in reference 2, B_1 and λ are used as the unknowns.

Before the solution can be carried out, some approximation must be made for the density profile ρ_1/ρ appearing in the third integral of Eq. (4). The dissociation data given by Moore can can be closely approximated by a fifth-degree polynomial in h

$$\frac{\rho_B}{\rho} = b_1 + b_2\frac{h}{h_B} + b_3\left(\frac{h}{h_B}\right)^2 + b_4\left(\frac{h}{h_B}\right)^3 + b_5\left(\frac{h}{h_B}\right)^4 + b_6\left(\frac{h}{h_B}\right)^5 \tag{13}$$

where $h_B = 96.8$ B.t.u. per lb. and, for $h_w = c_{p_w}T_w$,

$$\frac{h}{h_B} = \frac{C_{p_w}T_w}{h_B} - \frac{u_1^2}{2h_B}\left(\frac{u}{u_1}\right)^2 + \left(\frac{h_1}{h_B} - \frac{C_{p_w}T_w}{h_B} + \frac{u_1^2}{2h_B}\right)\frac{t^*}{t_1^*}$$

in terms of the velocity and stagnation enthalpy profiles.

Application of the above results to Eqs. (4) and (5) for the limiting case of $u_1 \to 0$ (stagnation flow) results in the following two simultaneous equations for λ and B_1:

$$k + k_1B_1 + k_2B_1^2 + k_3B_1^3 + k_4B_1^4 + k_5B_1^5 = \frac{\rho_B}{\rho_1}\left(\frac{7}{10} + \frac{\lambda}{120}\right) + \frac{\rho_B}{\rho_w}\frac{12+\lambda}{6\lambda} - \frac{\rho_B}{\rho_1}\frac{2}{315}\left(37 - \frac{\lambda}{3} - \frac{5\lambda^2}{144}\right) \tag{14}$$

$$B_1 = \frac{\sigma_w\lambda[a + (\lambda/6)a_2]}{(\rho_1/\rho_w) - \sigma_w\lambda[a_1 + (\lambda/6)a_4]} \tag{15}$$

$k, k_1, k_2, \ldots$, are constants depending on the values of $b_1, b_2, \ldots$, and the wall temperature and stream enthalpy; $a, a_1, \ldots$, are also constants.

The convective heat q transferred from a unit area of surface per unit time is

$$q_w = -k_w(\partial T/\partial y)_w$$

or using the definitions of t^*, t_1^*, λ, B_1, and Eq. (6)

$$q_wL = -\frac{k_w}{C_{p_w}}t_1^*B_1\left[\frac{\rho_1}{\mu_w}\frac{L^2}{\lambda}\frac{du_1}{dx}\right]^{1/2} \tag{16}$$

where L is a characteristic dimension. Defining a wall Nusselt Number as

$$Nu_w = q_wL/k_w[T_w - (h_1/C_{p_w})]$$

there results

$$\frac{Nu_w}{\sqrt{(\rho_wL^2/\mu_w)(du_1/dx)}} = B_1\sqrt{\frac{\rho_1/\rho_w}{\lambda}} \tag{17}$$

for stagnation flow. This is plotted in Fig. 1 versus h_1/h_B for $T_w = 2{,}000$°R. with and without dissociation. The corresponding density variation is also shown.

The conclusion obtained here for stagnation flow is that equilibrium dissociation has only a small effect on the actual heat-transfer rate per unit area, provided the wall temperature is less than the dissociation temperature (3,000–4,000°R.).

The validity of this conclusion can be indicated by using the above methods to compute the heat transfer on a flat plate with and without dissociation and comparing the results with those of Moore.[1] The expression obtained by the present method for the heat transfer on a flat plate is

$$q_w = \frac{k_w}{C_{p_w}}\rho_w\frac{a\left(h_1 + \frac{u_1^2}{2} - C_{p_w}T_w\right) + 2a_2(1-\sigma_w)u_1^2}{a_1 - \frac{37}{630\sigma_w}\left(2\frac{315}{37}\frac{\mu_w\rho_wx}{u_1}\right)^{1/2}} \tag{18}$$

Thus, since the only values appearing in Eq. (18) depend on the wall temperature, stream velocity, and stream enthalpy, there can be no effect of dissociation so long as both the stream and wall temperatures are below dissociation values. This result is not surprising, since by the present method the velocity and enthalpy profiles depend only on wall and stream conditions. It is to be noted, however, that the temperature and density profiles would be different for dissociation even with the same wall and stream conditions, since the enthalpy profile is invariant. Apparently, the temperature and density profiles either have little effect or compensating effects on the heat transfer at the wall of both a flat plate and blunt body.

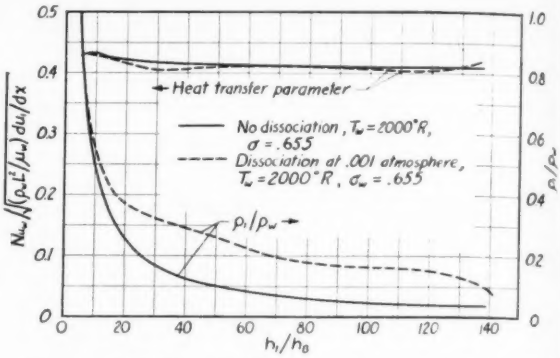

FIG. 1. Wall heat-transfer parameter versus enthalpy ratio at the forward stagnation point of a blunt-nosed body with and without dissociation. The lower curves show the corresponding density changes.

REFERENCES

[1] Moore, L. L., *A Solution of the Laminar Boundary-Layer Equations for a Compressible Fluid with Variable Properties, Including Dissociation*, Journal of the Aeronautical Sciences, Vol. 19, No. 8, p. 505, August, 1952.

[2] Kalikhman, L. E., *Heat Transmission in the Boundary Layer*, NACA TM No. 1229, April, 1949.

[3] Brown, W. Byron, and Donoughe, Patrick L., *Tables of Exact Laminar-Boundary-Layer Solutions When the Wall is Porous and Fluid Properties Are Variable*, NACA TN No. 2479, September, 1951.

Heat Transfer in a Transitional and Turbulent Boundary Layer at Supersonic Speeds

William B. Fallis*

Institute of Aerophysics, University of Toronto, Toronto, Canada

May 11, 1953

THE VARIATION IN TEMPERATURE RECOVERY and heat transmission with Reynolds Number in the laminar, transitional, and turbulent boundary layers on cone and cone-cylinder models has been recently reported by Eber.[1] His temperature measurements were made under transient conditions in the NOL 40- by 40-cm. Aeroballistics Tunnel. des Clers and Sternberg[2] have determined local recovery factors in the transitional and turbulent boundary-layer regions under temperature equilibrium conditions in the BRL tunnel also using cone and cone-cylinder models. The results do not support Eber's findings. Additional recovery factor and heat-transfer data[3] are available from transient temperature measurements made at a Mach Number of 2.5 in the transitional and turbulent boundary layers of a flat-plate model mounted in the UTIA 16- by 16-in. tunnel. Good agreement with Eber's results has been obtained.

Two geometrically similar models were used in the experiments: one a thermally insulated flat plate and the other a con-

* Now, Senior Aerodynamics Engineer, Consolidated Vultee Aircraft Corporation, Fort Worth, Tex.

ducting plate. The model span was $8^1/_2$ in. and the chord length 10 in. Eight plugs were inserted, flush with the surface, along the centerline of each plate and were spaced at 1-in. intervals beginning $1^1/_2$ in. aft of the leading edge. The plugs were completely interchangeable at all stations.

The thermocouple plug used with the nonconducting plate was made of bakelite with a thin copper disc set into its surface. A copper-eureka thermocouple junction was soldered to the under surface of the copper insert. This thermocouple plug was initially installed in the farthest aft station, and nonconducting plugs were inserted in the remaining stations. The insulated surface temperature was recorded for a series of tunnel runs by a high-speed photoelectric potentiometer. The thermocouple plug was then removed and interchanged with the plug in the next forward station. The process was repeated until temperature-time traces were obtained at each station.

Local recovery factors determined from adiabatic wall temperature measurements on the insulated plate are plotted in Fig. 1 as a function of Reynolds Number. The recovery factors are considered accurate to within ±1 per cent. The experimental curve may be divided into two regions: one where the variation in recovery factor is large and the other where it is constant. The recovery factors in the first region are higher than the theoretical laminar recovery curve and indicate that the boundary layer is transitional. In the second region the experimental data are represented to within 1.4 per cent by the theoretical relation $r = (Pr)_w^{1/3}$ derived for turbulent boundary-layer flow, where the fluid properties are evaluated at the adiabatic wall temperature. A liquid film method of flow visualization and schlieren photographs were also used to identify the turbulent boundary-layer region. The recovery factor in the transition region increased to a peak value approximately 4.5 per cent greater than the value in the turbulent boundary layer. These results bear out the work of Eber[1] and Stalder.[4]

The heat-transfer flat-plate model differed from the nonconducting model in that a sheet of $^1/_8$-in. thick copper was fitted to its surface. The centerline plugs were also made of copper. The thermocouple plug consisted of a $^1/_8$-in. thick copper core surrounded by an ebonite insulating jacket, with the thermocouple junction located midway between the upper and lower surfaces of the core. The conducting surface was uniformly heated to a temperature of about 40°C. above the adiabatic wall temperature. Heat-transfer measurements were made with heat flow occurring over the entire length of the plate. A series of tunnel runs and temperature records were made with the thermocouple plug installed in the trailing-edge station and then with it progressively moved forward toward the leading edge.

The local heat-transfer coefficient, calculated from a knowledge of the rate of cooling of the conducting model and the local adiabatic wall temperature, is plotted in Fig. 2 as the local Nusselt Number versus Reynolds Number, using the fluid properties corresponding to the adiabatic wall temperature. The local Nusselt Number predicted by the methods of Eckert and Drewitz for a laminar boundary layer and von Kármán and Colburn for a turbulent boundary layer are shown for comparison. The present experimental data indicate that the boundary layer on the flat-plate model was transitional for Reynolds Numbers less than approximately 4×10^6. The Nusselt Number for heat transfer in the fully developed turbulent boundary layer on the flat plate is in accord with Eber's cone-cylinder turbulent boundary-layer values and is well represented by the relation due to Colburn.

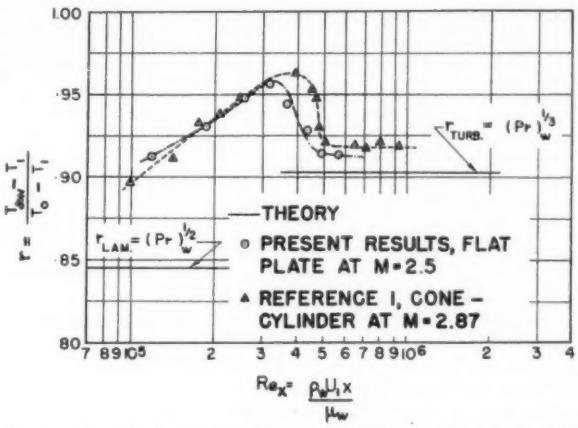
1.00
.95
.90
.85
80
$r_{TURB.} = (Pr)_w^{1/3}$
$r_{LAM.} = (Pr)_w^{1/2}$
THEORY
PRESENT RESULTS, FLAT PLATE AT M = 2.5
REFERENCE I, CONE – CYLINDER AT M = 2.87
7 8 9 10^5 2 3 4 5 6 7 8 9 10^6 2 3 4
$Re_x = \frac{\rho_w U_1 x}{\mu_w}$

FIG. 1. Local recovery factor variation with local Reynolds Number.

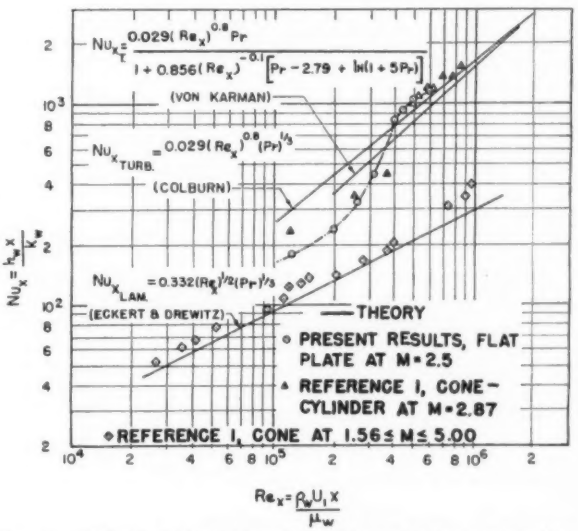
$Nu_{x_i} = \frac{0.029(Re_x)^{0.8} Pr}{1 + 0.856(Re_x)^{-0.1}[Pr - 2.79 + ln(1 + 5Pr)]}$
(VON KARMAN)
$Nu_{x_{TURB.}} = 0.029(Re_x)^{0.8}(Pr)^{1/3}$
(COLBURN)
$Nu_{x_{LAM.}} = 0.332(Re_x)^{1/2}(Pr)^{1/3}$
(ECKERT & DREWITZ)
THEORY
PRESENT RESULTS, FLAT PLATE AT M = 2.5
REFERENCE I, CONE – CYLINDER AT M = 2.87
REFERENCE I, CONE AT 1.56 ≤ M ≤ 5.00
$Nu_x = \frac{h_w x}{k_w}$
$Re_x = \frac{\rho_w U_1 x}{\mu_w}$

FIG. 2. Variation of local Nusselt Number with local Reynolds Number.

REFERENCES

[1] Eber, G., *Recent Investigation of Temperature Recovery and Heat Transmission on Cones and Cylinders in Axial Flow in the N.O.L. Aeroballistics Wind Tunnel*, Journal of the Aeronautical Sciences, Vol. 19, No. 1, p. 1, January, 1952.

[2] des Clers, B., and Sternberg, J., *On Boundary-Layer Temperature Recovery Factors*, Readers' Forum, Journal of the Aeronautical Sciences, Vol. 19, No. 9, p. 645, September, 1952.

[3] Fallis, W. B., *Heat Transfer in the Transitional and Turbulent Boundary Layers of a Flat Plate at Supersonic Speeds*, UTIA Report No. 19, May, 1952.

[4] Stalder, J. R., Rubesin, M. W., and Tendeland, T., *A Determination of the Laminar-, Transitional-, and Turbulent-Boundary-Layer Temperature-Recovery Factors on a Flat Plate in Supersonic Flow*, NACA TN No. 2077, June, 1950.

On the Operational Form of the Linearized Equation of Supersonic Flow

L. E. Fraenkel
Department of Aeronautics, the University, Glasgow, Scotland

May 25, 1953

AS IS WELL KNOWN, the linearized equation of supersonic flow,

$$\beta^2 \frac{\partial^2 \phi}{\partial x^2} - \frac{\partial^2 \phi}{\partial y^2} - \frac{\partial^2 \phi}{\partial z^2} = 0 \qquad (1)$$

may be written in operational form

$$\beta^2 p^2 \bar{\phi} - (\partial^2 \bar{\phi}/\partial y^2) - (\partial^2 \bar{\phi}/\partial z^2) = 0 \qquad (2)$$

where $\bar{\phi}(p, y, z)$ is the Laplace transform of the perturbation potential $\phi(x, y, z)$. However, the rigorous deduction of Eq. (2) from Eq. (1) is not so simple as it might at first appear, and the only justification given by many writers (see, for example, references 1, 2, and 3)—namely that "ϕ and $\partial\phi/\partial x$ vanish at $x = 0$"—is both insufficient and incorrect in the present case and may well mislead the uninitiated (as it did the present writer).

The first point to be noted in considering the transformation of Eq. (1) to Eq. (2) is that the relevant boundary values are those on the *downstream* side of the foremost Mach surface, which bounds the field of disturbed flow; and on this side ϕ vanishes, *but its derivatives in general do not.* Furthermore, in most flow fields there are a number of surfaces across which ϕ is continuous while its derivatives are discontinuous, and all these discontinuities must be taken into account when the operational form is derived.

We take the free stream to be in the direction of increasing x. The surfaces of discontinuity are denoted by $x = f_i(y, z)$, $(i = 0, 1, \ldots, n)$. The Heaviside operator is defined by

$$p^{-1} = \int_{f_0(y,\,z)}^{x} dx'$$

and the corresponding Laplace transform of any function $F(x, y, z)$ is

$$\bar{F}(p, y, z) = p \int_{f_0(y,\,z)}^{\infty} e^{-px} F(x, y, z)\, dx$$

We also adopt the notation

$$F[f_i(y, z) +, y, z] - F[f_i(y, z) -, y, z] = \Delta F(f_i, y, z)$$

We now multiply Eq. (1) by pe^{-px} and integrate from $x = f_0(y, z)$ to ∞, assuming that the resulting integrals exist for all the lines $y =$ constant, $z =$ constant on which Eq. (1) is satisfied for all x. [We cannot expect to justify Eq. (2) for values $y = y_1$, $z = z_1$ such that there are points $x = x_1$, $y = y_1$, $z = z_1$, where the solution will prove singular and Eq. (1) itself is not satisfied.]

Integrating twice by parts, we obtain

$$p \int_{f_0}^{\infty} e^{-px} \frac{\partial^2 \phi}{\partial x^2}\, dx \equiv \sum_{i=0}^{n-1} p \int_{f_i+}^{f_{i+1}-} e^{-px} \frac{\partial^2 \phi}{\partial x^2}\, dx + p \int_{f_n+}^{\infty} e^{-px} \frac{\partial^2 \phi}{\partial x^2}\, dx = -\sum_{i=0}^{n} pe^{-pf_i} \cdot \Delta \frac{\partial \phi}{\partial x}(f_i, y, z) + p^2 \bar{\phi}(p, y, z) \qquad (3)$$

Differentiating ϕ twice under the integral sign, we also find

$$\frac{\partial^2 \bar{\phi}}{\partial y^2} \equiv \frac{\partial^2}{\partial y^2}\left[\sum_{i=0}^{n-1} p \int_{f_i+}^{f_{i+1}-} e^{-px} \phi\, dx + p \int_{f_n+}^{\infty} e^{-px} \phi\, dx\right] = p \int_{f_0}^{\infty} e^{-px} \frac{\partial^2 \phi}{\partial y^2}\, dx - \sum_{i=0}^{n} pe^{-pf_i} \cdot \Delta \frac{\partial \phi}{\partial y}(f_i, y, z) \cdot \frac{\partial f_i}{\partial y} \qquad (4)$$

the expression for $\partial^2\bar{\phi}/\partial z^2$ being similar. Hence Eq. (1) becomes, by Eqs. (3) and (4),

$$\beta^2 p^2 \bar{\phi} - \frac{\partial^2 \bar{\phi}}{\partial y^2} - \frac{\partial^2 \bar{\phi}}{\partial z^2} - \sum_{i=0}^{n} pe^{-pf_i}\left[\beta^2 \Delta \frac{\partial \phi}{\partial x}(f_i, y, z) + \Delta \frac{\partial \phi}{\partial y}(f_i, y, z) \cdot \frac{\partial f_i}{\partial y} + \Delta \frac{\partial \phi}{\partial z}(f_i, y, z) \cdot \frac{\partial f_i}{\partial z}\right] = 0 \qquad (5)$$

We now complete the justification of Eq. (2) by proving that, for each i,

$$\beta^2 \Delta \frac{\partial \phi}{\partial x}(f_i, y, z) + \Delta \frac{\partial \phi}{\partial y}(f_i, y, z) \cdot \frac{\partial f_i}{\partial y} + \Delta \frac{\partial \phi}{\partial z}(f_i, y, z) \frac{\partial f_i}{\partial z} = 0 \qquad (6)$$

We introduce variables (ξ, η, ζ) such that $\xi = 0$ on the Mach surface $x = f_i(y, z)$,

$$\xi = x - f_i(y, z), \quad \eta = y, \quad \zeta = z$$

and we also write $\phi(x, y, z) = \varphi(\xi, \eta, \zeta)$. Then,

$$\left.\begin{aligned} \partial\phi/\partial x &= \partial\varphi/\partial\xi \\ \frac{\partial\phi}{\partial y} &= -\frac{\partial\varphi}{\partial\xi}\frac{\partial f_i}{\partial y} + \frac{\partial\varphi}{\partial\eta}, \\ \frac{\partial\phi}{\partial z} &= -\frac{\partial\varphi}{\partial\xi}\frac{\partial f_i}{\partial z} + \frac{\partial\varphi}{\partial\zeta} \end{aligned}\right\} \qquad (7)$$

and, since the equations of continuity and momentum ensure that ϕ and the tangential velocities are continuous across the surface $x = f_i(y, z)$, we have

$$\Delta \frac{\partial \varphi}{\partial \eta}(0, \eta, \zeta) = \Delta \frac{\partial \varphi}{\partial \zeta}(0, \eta, \zeta) = 0 \qquad (8)$$

Hence, the left side of Eq. (6) becomes, by Eqs. (7) and (8),

$$\Delta \frac{\partial \varphi}{\partial \xi}(0, \eta, \zeta)\left[\beta^2 - \left(\frac{\partial f_i}{\partial y}\right)^2 - \left(\frac{\partial f_i}{\partial z}\right)^2\right] \qquad (9)$$

Now the equation of any Mach cone may be written

$$x = x_1 + \beta\sqrt{(y - y_1)^2 + (z - z_1)^2}$$

so that

$$\frac{\partial x}{\partial y} = \frac{\beta(y - y_1)}{\sqrt{(y - y_1)^2 + (z - z_1)^2}}, \quad \frac{\partial x}{\partial z} = \frac{\beta(z - z_1)}{\sqrt{(y - y_1)^2 + (z - z_1)^2}}$$

whence

$$(\partial x/\partial y)^2 + (\partial x/\partial z)^2 = \beta^2 \qquad (10)$$

But the surface $x = f_i(y, z)$ is the envelope of a family of such Mach cones, so that Eq. (10), which is a relation between local surface slopes valid at every point of these constituent Mach cones, must also be valid on the Mach surface. Hence, the expression (9) is zero, Eq. (6) is proved, and the operational form, Eq. (2), is justified.

Finally, it may be worth mentioning that, when the generalized Fourier transform is applied to the differential equation (1), the above discussion still applies with only very slight changes.

References

[1] Gunn, J. C., *Linearized Supersonic Aerofoil Theory.* Phil. Trans. Roy. Soc. A, Vol. 240, p. 330, 1948.

[2] Stewartson, K., *On the Linearized Potential Theory of Unsteady Supersonic Motion,* Quart. Jour. Mech. Appl. Math., Vol. 3, pt. 2, p. 184, June, 1950.

[3] Adams, M. C., and Sears, W. R., *Slender Body Theory—Review and Extension,* Journal of the Aeronautical Sciences, Vol. 20, No. 2, p. 87, February, 1953.

On the Velocity Distribution in the Laminar Sublayer and Transition Region in Turbulent Shear Flows

Francis R. Hama

Iowa Institute of Hydraulic Research, State University of Iowa, Iowa City, Iowa

May 4, 1953

THE WELL-KNOWN RELATION on the mixing length

$$l = ky \qquad (1)$$

is chiefly based upon Nikuradse's experiments with flow in pipe. His result, however, is somewhat ambiguous in the region close to the wall. First, the measurement is done outside the pipe's

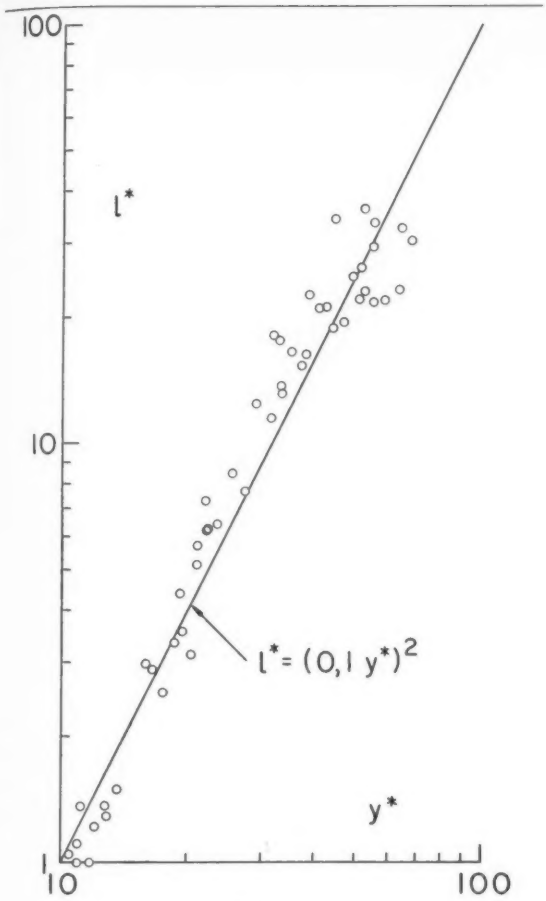

FIG. 1.

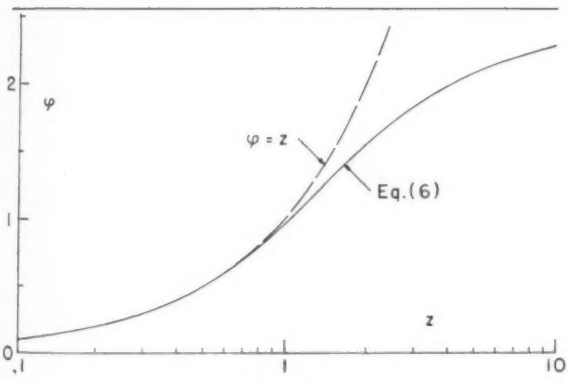

FIG. 2.

exit but not in the pipe. In fact, his result shows a finite velocity at $y = 0$. Second, the viscous term is neglected in the calculation of l. Furthermore, the logarithmic formula tends to minus infinity near the wall.

The writer[1] has calculated the mixing length from the velocity distribution in the turbulent boundary layer along a flat plate by using

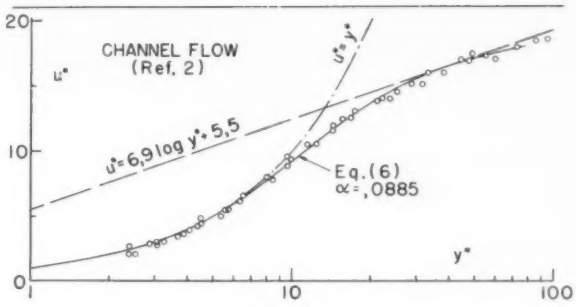

FIG. 3.

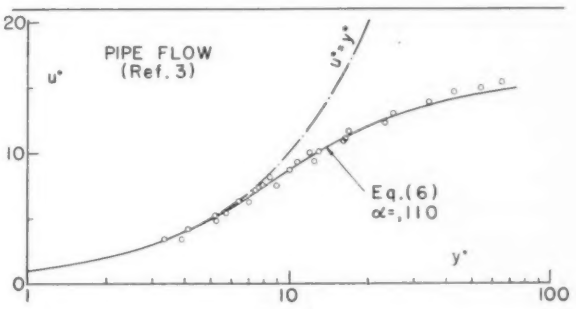

FIG. 4.

$$\frac{\tau}{\rho U^2} = \frac{\partial}{\partial x}\int_y^\infty \frac{u}{U}\left(1 - \frac{u}{U}\right)dy - \left(1 - \frac{u}{U}\right)\frac{\partial}{\partial x}\int_0^y \left(1 - \frac{u}{U}\right)dy \quad (2)$$

$$\tau = \rho l^2 (du/dy)^2 + \mu(du/dy) \quad (3)$$

and obtained a universal relation

$$l^* = (\alpha y^*)^2; \quad l^* \equiv lv^*/\nu, \quad y^* \equiv yv^*/\nu, \quad v^{*2} \equiv \tau_0/\rho \quad (4)$$

in the viscous region (laminar sublayer and transition region in which the viscous term is not negligible), α being a numerical constant, as shown in Fig. 1.

Once the universal relation, Eq. (4), is established, the velocity distribution in the viscous region can easily be obtained. Putting Eq. (4) into Eq. (3) and assuming $\tau = \tau_0 =$ constant, we have the differential equation

$$z^4(d\varphi/dz)^2 + 4(d\varphi/dz) - 4 = 0 \quad (5)$$

for which the solution is

$$\varphi = \frac{2}{3}\left[\frac{1 - \sqrt{1 + z^4}}{z^3} + F\left(\frac{1}{\sqrt{2}}, \psi\right)\right] \quad (6)$$

in which $\varphi \equiv \sqrt{2}\alpha u^*$, $z \equiv \sqrt{2}\alpha y^*$, and F is the elliptic integral of the first kind defined by

$$F\left(\frac{1}{\sqrt{2}}, \psi\right) \equiv \int_0^\psi \frac{d\psi}{\sqrt{1 - (1/2)\sin^2\psi}} = 2\int_0^z \frac{dz}{\sqrt{1 + z^4}} \quad \cos\psi \equiv (1 - z^2)/(1 + z^2) \quad (7)$$

The numerical value of $\varphi(z)$ is tabulated in Table 1 and plotted in Fig. 2. This solution includes the laminar sublayer profile

$$u^* = y^*; \qquad u^* \equiv u/v^* \quad (8)$$

for very small y^* and can be connected smoothly to the log-

TABLE 1

z	$\varphi(z)$
0	0
0.2	0.200
0.4	0.397
0.6	0.595
0.8	0.785
1.0	0.960
1.4	1.250
1.8	1.464
2.2	1.621
2.6	1.738
3.0	1.829
4.0	1.981
5.0	2.077
6.0	2.141
7.0	2.187
8.0	2.223
9.0	2.250
10.0	2.272
∞	2.472

arithmic distribution. The experimental results for the flat-plate boundary layer coincide well with Eq. (6) if the value $\alpha = 0.102$ is chosen. These facts and calculations have already been given by the writer.[1]

Now, if the relation (4) is also valid for channel or pipe flow, the velocity profile, Eq. (6), must be a good representation for that case, since the other assumption $\tau = \tau_0 =$ constant is allowable in the viscous region for channel or pipe flow. Comparison with some of the experimental results[2,3] is made in Figs. 3 and 4, in which α is chosen so that Eq. (6) connects smoothly to the logarithmic distribution for the channel flow or given arbitrarily for the pipe flow, since no logarithmic formula is given in the latter case.

In conclusion, the universal relation (4) is now well confirmed, and Eq. (6) gives a good representation for the velocity distribution in the viscous region either for boundary-layer or for channel or pipe flow. By use of the velocity distribution given here, a refinement in the calculation of friction or heat transfer can be expected. The numerical constant α cannot be determined definitely at the present stage, because of the lack of a consistent logarithmic law.

REFERENCES

[1] Hama, R., *Turbulent Boundary Layer along a Flat Plate*, Pt. 1 (in Japanese), Rep. Inst. Sci. Tech., Univ. of Tokyo, Vol. 1, No. 1, pp. 13–16, 1947.

[2] Laufer, John, *Investigation of Turbulent Flow in a Two-Dimensional Channel*, NACA TN No. 2123, 1950; or NACA TR No. 1053, 1951.

[3] Laufer, John, *The Structure of Turbulence in Fully Developed Pipe Flow*, NACA TN No. 2954, 1953.

The Medium in Fluid Mechanics

L. S. Dzung
Brown, Boveri & Cie., Baden, Switzerland

May 29, 1953

IT IS USUAL TO ASSUME certain idealized properties of the medium to simplify the mathematical theory of fluid mechanics. The most common assumption, in case the fluid is gaseous, is that of ideal gas with constant specific heat—i.e., polytropic gas.[1]

Traupel[2] shows that the equations of a polytropic gas

$$pv = RT \tag{1}$$
$$\kappa \equiv c_p/c_v = \text{const.} \tag{2}$$

can in most cases be relaxed and substituted by the less stringent ones,

$$z \equiv pv/RT = z(s) \tag{3}$$
$$k \equiv -(\partial \log p/\partial \log v)_s = \text{const.} \tag{4}$$

While Eq. (3) requires only that the "compressibility factor" z is a function of the entropy s alone, Eq. (1) requires that z is a constant. The isentropic exponent k becomes the ratio of specific heats κ for an ideal gas.

It can be shown, however, that Eq. (3) alone is sufficient to define a gaseous medium similar to the ideal gas defined by Eq. (1). The additional condition, Eq. (4), corresponds to the additional Eq. (2).

Define

$$\alpha \equiv (\partial \log v/\partial \log T)_p$$
$$\beta \equiv (\partial \log p/\partial \log T)_v$$
$$\gamma \equiv -(\partial \log p/\partial \log v)_T$$

From thermodynamic identities, it is known that[3]

$$\alpha\gamma = \beta, \quad k = \kappa\gamma, \quad \frac{T}{p}\left(\frac{\partial p}{\partial T}\right)_s = \frac{\kappa}{\kappa - 1}\cdot\beta \tag{5}$$

$$\left(\frac{\partial h}{\partial p}\right)_T = (1 - \alpha)v, \qquad \left(\frac{\partial u}{\partial v}\right)_T = (\beta - 1)p \tag{6}$$

where h and u denote enthalpy and energy, respectively. Now differentiate $pv = zRT$,

$$\frac{dp}{p} + \frac{dv}{v} = \frac{dz}{z} + \frac{dT}{T}$$

and substitute the definition of k for an isentropic

$$\left(1 - \frac{1}{k}\right)\frac{dp}{p} = \frac{dz}{z} + \frac{dT}{T} \quad (s = \text{const.})$$

or

$$\frac{k - 1}{k}\cdot\frac{T}{p}\left(\frac{\partial p}{\partial T}\right)_s = 1 + \frac{T}{z}\left(\frac{\partial z}{\partial T}\right)_s$$

Substituting Eqs. (5) into the left-hand side of the last equation and denoting the right-hand side by Z results in

$$\frac{k - 1}{k}\cdot\frac{\kappa}{\kappa - 1}\cdot\beta = \frac{k - 1}{\kappa - 1}\cdot\alpha = Z \tag{7}$$

For an *isothermal*, Eqs. (6) give

$$v\,dp = [1/(1 - \alpha)]dh$$
$$p\,dv = [1/(\beta - 1)]d(h - pv)$$

or, after adding,

$$d(pv) = \left(\frac{1}{1 - \alpha} + \frac{1}{\beta - 1}\right)dh - \frac{1}{\beta - 1}\,d(pv)$$

and by substituting α and β from Eq. (7),

$$dh = \frac{k\left[1 - Z\cdot\dfrac{\kappa - 1}{k - 1}\right]}{k - \kappa}\cdot d(pv) \quad (T = \text{const.}) \tag{8}$$

Now for an *isentropic*, $dh = v\,dp$. This can be written, together with the definition of k, as

$$dh = \frac{k}{k - 1}\cdot d(pv) \quad (s = \text{const.}) \tag{9}$$

Eqs. (8) and (9) become identical if $Z = 1$—i.e., if $(\partial z/\partial T)_s = 0$. This is Eq. (3). In this case

$$dh = [k/(k - 1)]\cdot d(pv) \tag{10}$$

Without restriction as to the constancy of a parameter.

Define

$$\tau \equiv pv/R \equiv zT, \quad \lambda \equiv k/(k - 1) \tag{11}$$

and consider τ and s as the independent variables of state. Eq.

(10) can be written more precisely as

$$(\partial h/\partial \tau)_s = \lambda R, \qquad (\partial h/\partial s)_\tau = 0$$

Differentiating the last equation with respect to τ and using the first one results in

$$\partial^2 h/\partial \tau \partial s = (\partial \lambda/\partial s)_\tau R = 0$$

The last equations show that h and λ (or k) do not depend on s and are, therefore, functions of τ alone,

$$h = h(\tau), \qquad k = k(\tau) = k(h) \tag{12}$$

These properties are exactly those of an ideal gas.

Define further a quantity σ corresponding to the entropy by $d\sigma = ds/z(s)$. If now Eqs. (10) and (11) are substituted into $Tds = dh - vdp$, one obtains

$$d\sigma = \lambda R(d\tau/\tau) - R(dp/p)$$

Because of Eq. (12), σ is "separable" as in case of the entropy of an ideal gas.

In fact, a medium defined by Eq. (3) has all the mathematical properties of an ideal gas as discussed in reference 1, Section 4, if T is substituted by τ, s by σ, c_p/R by λ, c_v/R by $\lambda - 1$, and κ by k. It seems, therefore, appropriate to call it an *ideal vapor* or a *perfect vapor*, following Leib.[4] If, in addition, Eq. (4) is true, then the medium can in most cases be treated as a polytropic gas and may be called a *polytropic vapor*. In this case, Eq. (10) can be integrated explicitly to give $h = \lambda pv$, corresponding to $h = c_p T$ for a polytropic gas. The integration constant has been set equal to zero.

Traupel[2] mentions that the equivalence breaks down if heat conduction is present. This situation can be saved sometimes, at least formally, if the gradients of T and of h can be considered as parallel. It is then possible to define an "enthalpy diffusivity" which relates the heat flux to grad. h as the thermal conductivity is related to grad. T. This diffusivity, unlike the conductivity, is, however, not a unique function of state unless the state path is prescribed.

References

[1] Courant, R., and Friedrichs, K. O., *Supersonic Flow and Shock Waves* Sections 3 and 4, pp. 6–10; Interscience Publishers, New York, 1948.

[2] Traupel, W., *Zur Dynamik realer Gase*, Forschung, Vol. 18, pp. 3–9. 1952.

[3] Dzung, L. S., *Beiträge zur Thermodynamik der realen Gase*, Schweize, Archiv, Vol. 10, pp. 305–313, 1944.

[4] Leib, E. F., *Thermodynamic Properties of Vapors*, Trans. ASME, Vol. 63, pp. 157–176, 1941.

Comments on Location of Detached Shock Waves Ahead of Plane Bodies

Robert Wesley Truitt

Professor of Aeronautical Engineering, Virginia Polytechnic Institute, Blacksburg, Va.

May 25, 1953

In his comment on my Readers' Forum paper,[1] Mr. Moeckel (in reference 2) correctly points out that both papers of references 1 and 3 are based on the same assumption concerning the body sonic point and, further, that experiment and theory shown in reference 1 confirms his geometrical method. My conclusions made in reference 1 were not intended to disprove Mr. Moeckel's original theory but rather to indicate the direct effect of nose angle on shock detachment distance. As stated in reference 1, the purpose of that paper was "to derive an expression for the shock detachment distance which is an *explicit* function of the opening angle of the wedge," which was done.

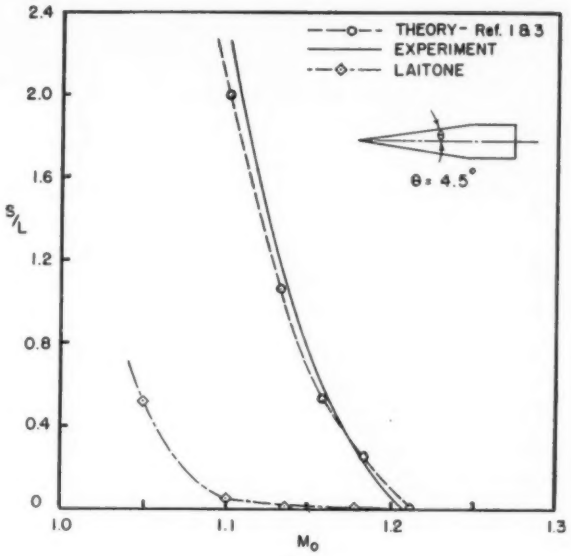

FIG. 1

In reference 4, Laitone erroneously states that the results of references 1 and 3 are only valid for relatively blunt bodies at the higher transonic Mach Numbers. Indeed, it is quite well known that for bodies with well-defined shoulders, such as slender simple wedges, the body sonic point is located at the shoulder, and, consequently, the *characteristic* distance is obviously from the foremost point of the shock to the shoulder of the wedge. This fact was the basis of the methods of references 1 and 3 and was shown in Fig. 2 of reference 1 to be in excellent agreement with experiment for *very slender* bodies. Laitone further claims that the only results valid for very slender wedges ($\theta \leq 5°$) at Mach Numbers near unity are his, given in Eq. (3) of reference 4. Laitone's results are plotted in Fig. 1 along with theoretical and experimental data of reference 1 for a $4^1/_2°$ wedge. It is clear that Laitone's results are in very poor agreement with experiment. On the other hand, theories of references 1 and 3 show excellent agreement.

References

[1] Truitt, R. W., *A Method for Location of Detached Shock Waves Ahead of Plane Bodies*, Readers' Forum, Journal of the Aeronautical Sciences, Vol. 20, No. 1, pp. 61–62, January, 1953.

[2] Moeckel, W. E., *Location of Detached Shock Waves Ahead of Plane Bodies*, Readers' Forum, Journal of the Aeronautical Sciences, Vol. 20, No. 5, p. 360, May, 1953.

[3] Moeckel, W. E., *Approximate Method for Predicting the Form and Location of Detached Shock Waves Ahead of Plane and Axially Symmetric Bodies*, NACA TN No. 1921, July, 1949.

[4] Laitone, E. V., *Comments on a Method for Location of Detached Shock Waves Ahead of Plane Bodies*, Readers' Forum, Journal of the Aeronautical Sciences, Vol. 20, No. 5, p. 360, May, 1953.

On the Transonic Drag of a Cone Cylinder

John W. Miles

Department of Engineering, University of California, Los Angeles; Consultant, Douglas Aircraft Company, Inc., Santa Monica

June 3, 1953

The differential equations governing the axisymmetric flow past a body of revolution in an otherwise undisturbed stream of near sonic velocity U are

$$u_r - v_x = 0 \tag{1}$$

$$r^{-1}(rv)_r = [(M^2 - 1) + (\gamma + 1)u]u_x \tag{2}$$

where the total axial (x) and radial (r) velocity components are $U(1 + u)$ and Uv and where γ is the usual specific heat ratio. We consider an approximate solution of these equations for a slender body ($\delta \ll 1$) consisting of a conical head of semicone angle δ and unit altitude and a cylindrical afterbody of constant radius δ, as shown in Fig. 1.

If it is assumed that the free-stream flow is only slightly supersonic or, more precisely, that the parameter

$$k = (M^2 - 1)/(\gamma + 1)\delta^2 \tag{3}$$

is a small positive number, there will be a detached shock far upstream of the body, and the flow will be subsonic between this shock and a sonic line, $r = f(x)$, which terminates at the shoulder ($x = 1$, $r = \delta$) of the cone-cylinder. The boundary condition at this sonic line, obtained by requiring the *local* Mach Number to be unity there, may be written

$$u + \frac{1}{2}v^2 = -k\delta^2, \qquad r = f(x) \tag{4}$$

Moreover, it is evident that the flow at the shoulder is locally Prandtl-Meyer, whence the sonic line must be perpendicular to the conical surface at the shoulder, viz.

$$f(1) = \delta, \qquad f'(1) = -\delta^{-1} \tag{5}$$

In the neighborhood of the body the right side of Eq. (2) may be neglected as $0(\delta^4)$; moreover, it is never large compared with the left in the region $0 < x < 1$, $0 < r < f(x)$, except possibly: (a) near $x = 0$, where there is a stagnation point at the nose of the cone; and (b) in the neighborhood of the shock. Accordingly, we pose the slender body approximation

$$u = \delta^2\left\{-k + \ln\left[\frac{r}{f(x)}\right] - \frac{\delta^2 x^2}{2f^2}\right\} \tag{6a}$$

$$v = \delta^2 x/r \tag{6b}$$

which satisfies Eq. (1), Eq. (2) with right side neglected, Eq. (4), and the boundary condition $v = \delta$ on the cone ($r = \delta x$).

The pressure on the cone is given by

$$p = -\rho U^2[u + (1/2)v^2]_{r=\delta x} \tag{7a}$$

$$= \rho U^2\delta^2\left\{k + \ln\left[\frac{f(x)}{\delta x}\right] + \frac{1}{2}\left(\frac{\delta^2 x^2}{f^2} - 1\right)\right\} \tag{7b}$$

The corresponding drag coefficient, based on the free-stream dynamic pressure $(1/2)\rho U^2$ and the base area $\pi\delta^2$, is (after integration by parts)

$$C_D = 2\delta^2\left[k - \int_0^1 x^2\frac{f'(x)}{f(x)}\,dx\right] \tag{8}$$

The term δ^2x^2/f^2 in Eq. (7) makes only a higher order (in δ) contribution to Eq. (8).

The integral in Eq. (8) can be evaluated approximately by noting that $f(x)$ is $0(\delta^{-1})$ except near $x = 1$, where it is $0(\delta)$, so that the contribution of the integrand is concentrated in the neighborhood of $x = 1$. It follows that only a small error will be committed by replacing the slowly varying numerator $x^2f'(x)$ by its value at $x = 1$, viz. $-\delta^{-1}$, and replacing $f(x)$ by the first two terms in its Taylor expansion about $x = 1$, whence

$$\int_0^1 x^2\frac{f'(x)}{f(x)}\,dx \simeq -\delta^{-1}\int_0^1 \frac{dx}{\delta - \delta^{-1}(x - 1)} \simeq \ln\delta^2 \tag{9}$$

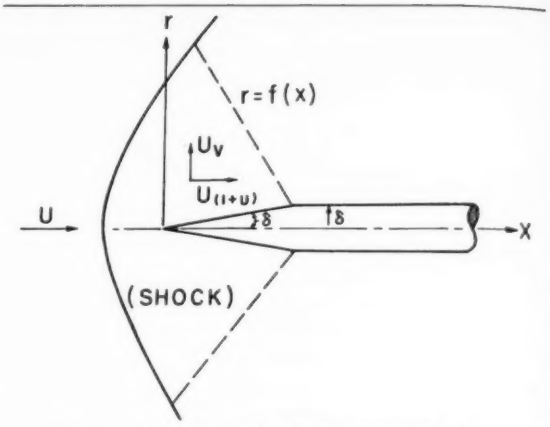

FIG. 1. Cone-cylinder in slightly supersonic flow.

[We emphasize that the approximation (9) does not assume $f(x)$ to be everywhere a straight line.] Substituting Eq. (9) in Eq. (8) yields

$$C_D = \delta^2(2k - 4\ln\delta) \tag{10}$$

The result, Eq. (10), may be subjected to two general checks. Firstly, provided that γ is held constant,* it satisfies the similarity law proposed by Oswatitsch and Berndt,[1] viz., $\delta^{-2}C_D + 4\ln\delta$ depends only on the similarity parameter k. Secondly, the slope of the C_D versus M curve at $M = 1$ is given by

$$\partial C_D/\partial M|_{M=1} = 4/(\gamma + 1) \tag{11}$$

as should be expected from the general considerations advanced by Liepmann and Bryson.[2] More directly,

$$\partial u/\partial M|_{M=1} = -[2/(\gamma + 1)]$$

The present problem has been solved numerically by Yoshihara[3] for $M = 1$. The result obtained by applying Simpson's rule to the integration of the pressure distribution over a 5° cone (Fig. 7 of reference 3) is $C_D = 0.0758$, while Eq. (10) yields 0.0747. Since the difference ($1^1/_2$ per cent) between these two numbers is of the same order as δ^4, the agreement is within the expected accuracy of the small disturbance theory, and it appears that Eq. (10) is a satisfactory approximation for sufficiently small values of k and δ. Nevertheless, it must be emphasized that this is in some measure fortuitous, and Eq. (10) probably still neglects some term of $0(\delta^2)$, even though the term of $0(\delta^2\ln\delta)$ is correctly predicted; moreover, it is not reliable for values of k sufficiently large to bring the intersection of the sonic line and bow shock close to the body. Since shock attachment occurs for values of k near unity (1.4 for a 5° cone), this last restriction implies $k \ll 1$.

REFERENCES

[1] Oswatitsch, K., and Berndt, S. B., *Aerodynamic Similarity at Axisymmetric Transonic Flow around Slender Bodies*, KTH-Aero TN 15, Stockholm, 1950.

[2] Liepmann, H. W., and Bryson, A. E., *Transonic Flow Past Wedge Sections*, Journal of the Aeronautical Sciences, Vol. 17, No. 12, pp. 745–755, December, 1950.

[3] Yoshihara, H., *On the Flow over a Cone-Cylinder at Mach Number One*, WADC TR 52-295, Wright Air Development Center, Dayton, Ohio, November, 1952.

* It is not clear whether the similarity law of reference 1 is valid with respect to changes in γ in the present problem due to the local Prandtl-Meyer expansion at the shoulder. On the other hand, the requirement that the sonic line be normal to the cone surface is not entirely consistent with the slender body approximation.

Similar Solutions of Compressible Boundary-Layer Equations

Ting-Yi Li and Henry T. Nagamatsu
California Institute of Technology, Pasadena, Calif.
June 1, 1953

THE COMPRESSIBLE BOUNDARY-LAYER EQUATIONS are rather well known. They are, in terms of the conventional symbols, as follows:

$$\rho u \frac{\partial u}{\partial x} + \rho v \frac{\partial u}{\partial y} = -\frac{\partial p}{\partial x} + \frac{\partial}{\partial y}\left(\mu \frac{\partial u}{\partial y}\right) \tag{1}$$

$$\partial p/\partial y = 0 \tag{2}$$

$$(\partial/\partial x)(\rho u) + (\partial/\partial y)(\rho v) = 0 \tag{3}$$

$$JC_p\left(\rho u \frac{\partial T}{\partial x} + \rho v \frac{\partial T}{\partial y}\right) = u \frac{\partial p}{\partial x} + u\left(\frac{\partial u}{\partial y}\right)^2 + \frac{\partial}{\partial y}\left(k \frac{\partial T}{\partial y}\right) \tag{4}$$

Assume Pr (Prandtl Number) = 1 and JC_p = constant, and introduce

$$S = \frac{JC_pT + (1/2)u^2}{JC_pT_1 + (1/2)u_1^2} - 1 \tag{5}$$

where suffix 1 refers to the main stream conditions. Then, the energy equation, Eq. (4), can be put into the following convenient form:

$$\rho u \frac{\partial S}{\partial x} + \rho v \frac{\partial S}{\partial y} = \frac{\partial}{\partial y}\left(\mu \frac{\partial S}{\partial y}\right) \tag{6}$$

Perform, next, Stewartson's transformation[1] from (x,y) plane to (Z,Y) plane where

$$Z = \int_{x_0}^{x} \left(\frac{a_1}{a_0}\right)^{(3\gamma-1)/(\gamma-1)} dx \tag{7}$$

$$Y = \frac{a_1}{a_0\sqrt{\nu_0}} \int_0^y \frac{\rho}{\rho_0}\, dy \tag{8}$$

If we take $\mu \propto T$, then Eqs. (1) and (6) become, respectively,

$$\frac{\partial^3\psi}{\partial Y^3} - \frac{\partial\psi}{\partial Y}\frac{\partial^2\psi}{\partial Y \partial Z} + \frac{\partial^2\psi}{\partial Y^2}\frac{\partial\psi}{\partial Z} = -V_1 \frac{dV_1}{dZ}(1 + S) \tag{9}$$

$$\frac{\partial\psi}{\partial Y}\frac{\partial S}{\partial Z} - \frac{\partial S}{\partial Y}\frac{\partial\psi}{\partial Z} = \frac{\partial^2 S}{\partial Y^2} \tag{10}$$

where ψ is the stream function defined as follows:

$$u = \frac{\rho_0}{\rho}\sqrt{\nu_0}\frac{\partial\psi}{\partial y} = \frac{a_1}{a_0}\frac{\partial\psi}{\partial Y} \tag{11}$$

$$v = -\frac{\rho_0}{\rho}\sqrt{\nu_0}\frac{\partial\psi}{\partial x} = -\frac{\rho_0}{\rho}\sqrt{\nu_0}\left[\left(\frac{a_1}{a_0}\right)^{(3\gamma-1)/(\gamma-1)}\frac{\partial\psi}{\partial Z} + \frac{\partial\psi}{\partial Y}\frac{\partial Y}{\partial x}\right] \tag{12}$$

$$V_1 = (a_0/a_1)u_1 = a_0 M_1 \tag{13}$$

Therefore, in the (Z, Y) plane the boundary-layer equations become Eqs. (9) and (10). The usual boundary conditions

$$\left.\begin{array}{lll} y = 0, & u = v = 0, & T = T_w \\ y \to \infty, & u \to u_1, & T \to T_1 \end{array}\right\} \tag{14}$$

can be represented as

$$\left.\begin{array}{lll} Y = 0, & \dfrac{\partial\psi}{\partial Y} = \psi = 0, & S = S_w \\ Y \to \infty, & \dfrac{\partial\psi}{\partial Y} \to V_1, & S \to 0 \end{array}\right\} \tag{15}$$

where the suffix w refers to the surface conditions. The condition of heat insulation at the surface is simply $S = S_w = 0$; in that case, Eq. (10) is an identity, while the problem reduces to the solution of the incompressible boundary-layer equation with a main stream velocity V_1.[1] For the general cases with heat flow across the surface, we must, however, consider Eqs. (9) and (10), together with the boundary conditions, Eqs. (15).

If, in Eq. (15), S_w = constant, we can construct similar solutions for the system, Eqs. (9), (10), and (15). To find such similar solutions of the compressible boundary-layer equations, we introduce f, g, η as follows:

$$\psi = Z^a V_1^p f(\eta) \tag{16}$$

$$S = S_w g(\eta) \tag{17}$$

$$Y = Z^b V_1^q \eta \tag{18}$$

where a, b, p, and q are constant parameters satisfying the following conditions simultaneously:

$$\frac{dV_1}{dZ} = K_9 Z^{-2b} V_1^{-2q} \tag{19}$$

$$\frac{dV_1}{dZ} = \frac{K_8}{p} Z^{-2a} V_1^{2-2p} - \frac{a}{p} Z^{-1} V_1 \quad (p \neq 0) \tag{20}$$

$$\frac{dV_1}{dZ} = \frac{K_{10}}{q} Z^{-2a} V_1^{2-2p} - \frac{b}{q} Z^{-1} V_1 \quad (q \neq 0) \tag{21}$$

The partial differential equations, Eqs. (9) and (10), then become ordinary equations

$$\frac{d^3f}{d\eta^3} - K_1\left(\frac{df}{d\eta}\right)^2 + K_2 f \frac{d^2f}{d\eta^2} = -K_3(1 + K_4 g) \tag{22}$$

$$(d^2g/d\eta^2) + K_5 f(dg/d\eta) = 0 \tag{23}$$

The boundary conditions, Eqs. (15), become

$$\left.\begin{array}{lll} \eta = 0, & f = df/d\eta = 0, & g = 1 \\ \eta \to \infty, & df/d\eta = K_6, & g = 0 \end{array}\right\} \tag{24}$$

In Eqs. (19)–(24), K_n are constants (n = 1–10). They are related simply as follows:

$$\left.\begin{array}{l} K_7 = \dfrac{K_1}{K_6}, \quad K_8 = \dfrac{K_2}{K_6}, \quad K_9 = \dfrac{K_3}{K_6}, \quad K_{10} = K_8 - K_7 \\ K_4 = S_w, \quad K_5 = 0 \end{array}\right\} \tag{25}$$

By examining the integrals of the differential equations [Eqs. (19)–(21)], we conclude that the following classes of similar solutions are possible:

(1) $p = 1 + q$, $a = b = 0$, $V_1 = [(1 + 2q)(K_9 Z + C)]^{1/(1+2q)}$ (26)*

Eqs. (22) and (23) become

$$\frac{d^3f}{d\eta^3} + (1 + q)K_1 f \frac{d^2f}{d\eta^2} = K_1\left[\left(\frac{df}{d\eta}\right)^2 - (1 + K_4 g)\right] \tag{22a}$$

$$(d^2g/d\eta^2) + (1 + q)K_1 f(dg/d\eta) = 0 \tag{23a}$$

The boundary conditions are

$$\left.\begin{array}{lll} \eta = 0, & f = df/d\eta = 0, & g = 1 \\ \eta \to \infty, & df/d\eta = 1, & g = 0 \end{array}\right\} \tag{25a}$$

(2) $p = 1/2$, $q = -(1/2)$, $a = b = 0$, $V_1 = ce^{K_1 Z}$ (27)*

Eqs. (22) and (23) become

$$\frac{d^3f}{d\eta^3} + \frac{1}{2}K_1 f \frac{d^2f}{d\eta^2} = K_1\left[\left(\frac{df}{d\eta}\right)^2 - (1 + K_4 g)\right] \tag{22b}$$

$$(d^2g/d\eta^2) + (1/2)K_1 f(dg/d\eta) = 0 \tag{23b}$$

The boundary conditions are the same as given in Eq. (25a).

* C is an arbitrary constant.

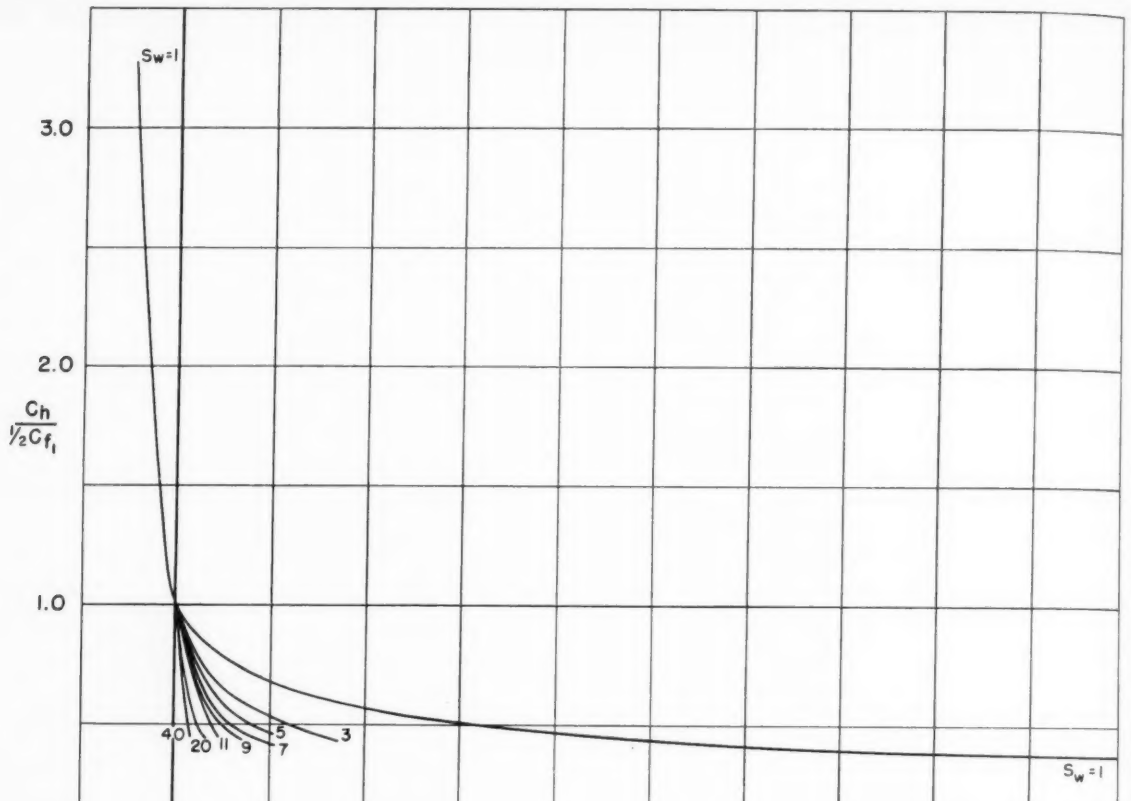

FIG. 1 — VALUES OF $\frac{C_{h_1}}{\frac{1}{2}C_{f_1}}$ FOR VARIOUS SURFACE TEMPERATURES WITH DIFFERENT FREE STRE PRESSURE GRADIENTS

$$(3)\quad \frac{a-b}{1+q-p}=\frac{1-2b}{2q+1}=\frac{1-2a}{2p-1}=m,\quad V_1=\frac{K_9}{m}Z^m \qquad (28)$$

$$(4)\quad p=\frac{1}{2},\quad q=-\frac{1}{2},\quad a=\frac{1}{2},\quad b=\frac{1}{2},\quad V_1=CZ^{K_3} \qquad (31)^*$$

(m being a constant).

Eqs. (22) and (23) become

$$\frac{d^3f}{d\eta^3}+K_2f\frac{d^2f}{d\eta^2}=K_1\left(\frac{df}{d\eta}\right)^2-K_3(1+K_4g) \qquad (22c)$$

$$(d^2g/d\eta^2)+K_2f(dg/d\eta)=0 \qquad (23c)$$

The boundary conditions are

$$\left.\begin{array}{lll}\eta=0, & f=df/d\eta=0, & g=1\\ \eta\to\infty, & df/d\eta=K_6, & g=0\end{array}\right\} \qquad (29)$$

K_1, K_2, K_3, and K_6 are mutually related as follows:

$$\left.\begin{aligned}K_3&=mK_6{}^{1+[m/(a-b)]}\\ K_2&=\frac{p-a}{2p-1}K_6{}^{1+[m(2p-1)/(a-b)]}\\ K_1&=\left[\frac{p-a}{2p-1}-(b+mq)\right]K_6{}^{1+[m(2p-1)/(a-b)]},\\ K_6&=\left(\frac{K_9}{m}\right)^{q-p+1}\end{aligned}\right\} \qquad (30)$$

Eqs. (22) and (23) become

$$\frac{d^3f}{d\eta^3}+\frac{1}{2}(1+K_3)f\frac{d^2f}{d\eta^2}=K_3\left[\left(\frac{df}{d\eta}\right)^2-(1+K_4g)\right] \qquad (22d)$$

$$(d^2g/d\eta^2)+(1/2)(1+K_3)f(dg/d\eta)=0 \qquad (23d)$$

The boundary conditions are the same as given in Eq. (25a).

In cases (3) and (4) above, the expressions for V_1 are similar, usually it is more convenient to deal with case (3), with, indeed, little sacrifice in generality. Hence, *similar solutions are possible if S_w = constant and if a, b, p, q, and V_1 are defined as in Eqs. (26), (27), (28), and (31).*

For a limited range of values of S_w and K_3, numerical integration of the ordinary differential equations, Eqs. (22d) and (23d), with the proper boundary conditions, Eq. (25a), has been carried out on the Reeves Electronic Analogue Computor.† To conclude the present note, we have shown in Fig. 1 a diagram of $2C_{h_1}/C_{f_1}$ versus K_3 obtained from analyzing these numerical results. C_{h_1} and C_{f_1} are the local coefficients of heat transfer

* C is an arbitrary constant.

† The authors are indebted to Arthur Presson, of the Jet Propulsion Laboratory, for his close cooperation in obtaining these numerical solutions.

and skin friction, respectively, defined as

$$C_{h_1} = -\frac{k_w(\partial T/\partial y)_w}{C_p\rho_1 u_1(T_w - T_{w\,\text{ins.}})}$$

$$C_{f_1} = \frac{\mu_w(\partial u/\partial y)_w}{(1/2)\rho_1 u_1^2} \tag{32}$$

where $T_{w\text{ins.}}$ is the temperature on an insulated surface,

$$T_{w\text{ins.}} = T_1\{1 + [(\gamma - 1)/2]M_1^2\}$$

It can easily be shown that

$$\frac{2C_{h_1}}{C_{f_1}} = -\left[\left(\frac{dg}{d\eta}\right)\Big/\left(\frac{d^2f}{d\eta^2}\right)\right]_{\eta=0} \tag{33}$$

The parameter K_2 is related to the pressure gradient in the free stream as follows:

$$K_2 = -\left(\frac{a_0}{a_1}\right)^{(3\gamma-1)/(\gamma-1)}\left[1 + \frac{\gamma - 1}{2}M_1^2\right]\times \frac{1}{\rho_1 u_1^2}\frac{dp}{dx}\int_{x_0}^{x}\left(\frac{a_1}{a_0}\right)^{(3\gamma-1)/(\gamma-1)}dx \tag{34}$$

Evidently, $K_2 = 0$ corresponds to the case of a flat surface with zero pressure gradient, for such case, $2C_{h_1}/C_{f_1} = 1$ as expected. For a flat surface with favorable pressure gradient, $dp/dx < 0$, $K_2 > 0$, it is found $2C_{h_1}/C_{f_1} < 1$; the curves in Fig. 1 become steeper as S_w (which for the range of S_w's computed are positive) increases. This seems to indicate that the effect of a favorable pressure gradient is to increase the skin-friction coefficient such that the ratio $2C_{h_1}/C_{f_1}$ becomes smaller than unity. This effect becomes more acute when the surface is much heated above the free-stream temperature. For a flat surface with adverse pressure gradient, $dp/dx > 0$, $K_2 < 0$, it is found $2C_{h_1}/C_{f_1} > 1$; the negative K_2 branch of the curve given in Fig. 1 is computed for $S_w = 1$. It is well known that a laminar boundary layer will separate under the influence of an adverse pressure gradient of certain magnitude. For a separating flow, $C_{f_1} \to 0$, this seems the reason for the rapid rise of the $2C_{h_1}/C_{f_1}$ curve for $K_2 < 0$ in Fig. 1.

Reference

[1] Stewartson, K., *Correlated Incompressible and Compressible Boundary Layers*, Proc. Roy. Soc. A, Vol. 200, 1949.

Turbulence Measurements in Flight

Max Kramer
Technical Director, Coleman Engineering Company, Inc., Los Angeles
May 25, 1953

Summary

For many reasons, it is desirable to obtain reliable and complete information about the turbulence structure of the atmosphere. For instance, the correct interpretation of wind-tunnel results on laminar profiles, maximum lift devices, etc., depends upon the knowledge of the structure of the turbulence encountered in flight. Also, gust loads and vibrations can be better predicted if the turbulence structure of the atmosphere is thoroughly known.

Many flight tests have dealt with the measurement of the turbulence encountered in flight. However, it seems that the most versatile method specifically suited to study of the problem at great flight speed has not been used, or not sufficiently so, to furnish all the information required. The following explains this comparatively simple method and presents results obtained by its use.

The Measuring Method

Turbulence causes oscillations of the ram pressure, as well as oscillations of the angle of attack. If $(\Delta\bar{v})$ is the average speed vector of the turbulence, (v_0) is the flight speed, and (ρ) is the air density, the average amplitude of the ram pressure oscillation is

$$\Delta\bar{p} = \rho x v_0 x \Delta\bar{v} \tag{1}$$

and the average amplitude of the angle of attack oscillations is

$$\Delta\bar{\alpha} = \Delta\bar{v}/v_0 \tag{2}$$

The equations indicate that, for equal turbulence, the ram-pressure oscillations increase with increasing flight speed, while the angle of attack oscillations decrease with increasing flight speed. Thus a study of the turbulence carried out at high speed must concentrate on the measurement of the ram-pressure oscillations.

Today's flight speeds are close to sonic speed or approximately 1,000 ft. per sec. When assuming this speed and sea-level density, the unit turbulence speed vector can be expressed as a ram-pressure noise level:

$$\Delta\bar{v} = 1 \text{ in. per sec.} = 114 \text{ db. acoustic pressure (acoustic reference level} = 0.0002 \text{ dyn. per cm.}^2) \tag{3}$$

One inch per second is certainly a small speed vector of the atmospheric turbulence, and yet this small speed vector generates a high noise level when acting on a microphone that is exposed to the ram-pressure oscillations at high speed. The acoustic pressure of 114 db. mentioned is, for instance, comparable to the peak pressure generated by a conventional single propeller airplane at a 100-ft. distance. Thus a microphone fed by the ram pressure is a comparatively simple means to measure the turbulence encountered in flight if the noise generated by the carrier airplane does not interfere with the measurement. The elimination of the carrier noise interference is the greatest problem of the method. There exist two basic possibilities to eliminate this interference.

(1) If the carrier speed is slightly below sonic speed, mounting the microphone on the tip of a boom protruding in front of the carrier is one possibility. The geometric distance between the microphone and the noise source will thereby be acoustically increased with the factor $[1/(1 - M_0)]$ when (M_0) is the speed of the carrier expressed in Mach Number.

(2) If the carrier speed is approximately half the sonic speed, the microphone must be mounted inside a towed body that trails the carrier at an appropriate distance. Naturally, the weight of the towed body and the drag of the towing cable must be so that the towed body flies below the turbulent wake of the carrier.

The Results of Flight Measurements

A comparatively slow single propeller airplane was used for the flight measurements. Its maximum diving speed was limited to Mach 0.6. Consequently, the microphone was mounted inside a towed body which, in turn, was released and retrieved in flight. The towing cable had a length of 400 ft. and an outside diameter of $^1/_{16}$ in. The overall length of the towed body was 3 ft. and its total weight was 12 lbs. The microphone was tuned to 175 cycles per sec. and had a band width of approximately 10 per cent of its center frequency. The microphone output was fed through the towing cable into an electronic voltmeter. The voltmeter was calibrated in decibel center frequency pressure at sea level.

All flight tests were flown under fair weather conditions. The first flights were to prove whether a carrier noise interference existed. Maximum power flights and minimum power dives were repeated at various flight speeds and altitudes. Since the power setting did not affect the microphone output, it was felt that the carrier noise did not interfere. Nevertheless, most of the results were obtained at a low power setting.

The first actual measurements were to determine the relation between the ram-pressure noise and the flight speed. Two flights at 10,000 ft. altitude indicated that, within the range from 150 to 450 m.p.h. true speed, the noise pressure is proportional to the flight speed. An essential conclusion can be drawn from this

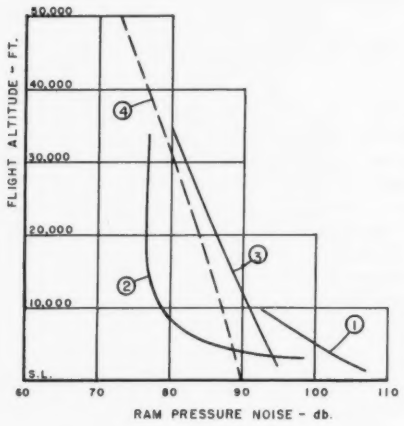

FIG. 1 - THE RAM PRESSURE NOISE AT VARIOUS ALTITUDES
TRUE FLIGHT SPEED = 400 MPH

① AVERAGE OF FOUR FLIGHTS UNDER VARIOUS CONDITIONS

② AVERAGE OF TWO FLIGHTS UNDER CLEAR WINDY CONDITIONS

③ ONE FLIGHT UNDER CALM HAZY CONDITIONS

④ THE AMBIENT DENSITY VS. ALTITUDE

result. Since the microphone was tuned to a fixed frequency, a variation of the flight speed means that the noise is generated by eddies of various sizes. For instance, at 150 m.p.h. or 220 ft. per sec. flight speed, eddies of 1.26 ft. in diameter generate the 175 cycles per sec. noise; while at 450 m.p.h. or 660 ft. per sec. flight speed, eddies of 3.78 ft. in diameter generate the 175 cycles per sec. noise. Thus, according to Eq. (1), proportionality between the flight speed and the noise pressure means *the average fair weather turbulence speed vector* ($\Delta\bar{v}$) *is independent of the eddy size.* Naturally, this conclusion is limited to the comparatively narrow range of the measurement. Greater speed ratios, as well as the use of several center frequencies, could broaden this range and might still disclose a variation of the fair-weather turbulence vector for greatly different eddy sizes.

The next flights were to determine the relation between the ram pressure noise and the flight altitude. Fig. 1 compiles the results of seven flights at 400 m.p.h. true speed and various altitudes. Four flights covered the range from 1,000 to 10,000 ft. altitude. The line (1) in Fig. 1 indicates the averaged result of these four flights. Two more flights extended the measurement up to 30,000 ft. altitude. The averaged result of these two flights is indicated by the curve (2) in Fig. 1. Both flights were flown on clear windy days in summer. Finally, one flight was flown on a calm hazy day in the fall. Curve (3) in Fig. 1 indicates the result of this last flight.

Fig. 1 shows the well-known fact that wind and sunshine cause increased turbulence near the ground. This ground effect disappears above approximately 10,000 ft. altitude. Especially the measurement on a calm hazy day seems to indicate that, outside of the ground effect, the ram noise is approximately proportional to the ambient air density. This, according to Eq. (1), would mean *the average fair weather turbulence speed vector* ($\Delta\bar{v}$) *is constant above 10,000 ft. altitude.* This is an important conclusion if it can be verified by more extensive flight tests.

Surprising is the actual value of the average turbulence speed vector. When extrapolating curve (3) in Fig. 1 to sea level and comparing the result with that of Eq. 3, we find the average fair-weather turbulence vector above 10,000 ft. altitude to be as small as

$$\Delta\bar{v} = 1.0\left(\frac{1{,}000}{580}\right)\left(\frac{1}{2.83}\right) = 0.6 \text{ in. per sec.} \qquad (4)$$

Conclusions

(1) A narrow-band microphone fed by the ram pressure was used to measure the ambient turbulence in flight. The method is comparatively simple and informative, particularly in connection with high-speed carrier airplanes.

(2) The results obtained seem to indicate that, under fair-weather conditions, the average turbulence speed vector is independent of the eddy size, as well as of the altitude, when measured above 10,000 ft. altitude. The fair-weather turbulence speed vector was 0.6 in. per sec. above 10,000 ft. altitude. Near the ground, the vector may be up to ten times stronger.

(3) When using a wide-band microphone and a tape recorder aboard a high-speed carrier, a future investigation would cover a large frequency range, as well as a wide altitude range, in a single flight. Such investigations would greatly contribute to the knowledge of the turbulence structure of the atmosphere.

Suggestion for Binding
Issues of the Journal of the Aeronautical Sciences

Arrangements have been made so that our readers may have their issues of the JOURNAL bound carefully and economically in our authorized binding. Simply write for details to:

AIRE
P.O. Box 776
Highland Park, Illinois